A Measurement of the Top Quark Mass

by

Kirsten Anne Tollefson

Submitted in Partial Fulfillment
of the
Requirements for the Degree
Doctor of Philosophy

Supervised by
Professor Paul Tipton
Department of Physics and Astronomy
The College
Arts and Sciences

University of Rochester
Rochester, New York
1997

Curriculum Vitae

The author was born in Fort Benning, Georgia on July 11, 1970. She graduated with a Bachelor of Arts degree in Physics from Gustavus Adolphus College. She continued her education at the University of Rochester where she began her graduate studies in the fall of 1992. She pursued her research in high energy physics under the direction of Professor Paul Tipton, and received the Master of Arts degree in the Spring of 1994.

Acknowledgements

This thesis could not have been written without the help and support of many people. Foremost I would like to thank my advisor, Paul Tipton, for his time, effort and financial backing which made it possible for me to become Dr. "Hotshot". Paul taught me how to become a good physicist by "always taking the high road", even though sometimes he himself strayed. In tribute to Paul, my food drawer will always be stocked with Baldies. My development as a physicist was also greatly influenced by Richard Hughes and Brian Winer. Thank you for teaching me the finer points of physics analysis and for all of those end-of-the-hall think-tank sessions which usually ended up in laughter. Thanks to Rob Roser for his encouragement, support, and introduction to Patagonia. Thanks go to my officemates, Gordon Watts, Phil Koehn and Josh Cassada. To Gordon for showing me a little bit about the wilder side of life, to Phil for teaching me the proper english language usage of the word "shwunk", and to Josh for being the younger graduate student so that I was no longer "The Kid". Thanks to all my fellow students at Rochester for keeping me sane during those first two years of graduate school.

This thesis builds upon and incorporates work done by many other physicists. I would like to thank the members of the top group for teaching me how to do top physics and the members of the CDF collaboration for teaching me how to do high-energy physics. Thanks also go to the Fermilab staff, without whom there would be no experiment and no data.

A very special thanks goes to my family and friends for their endless support, patience and encouragement. They always believed in me, even during those times when I didn't believe in myself. Thanks to my grandma, Lois Tollefson, for teaching me that the best things in life are the simple things. Thanks to my parents for their love and understanding. Thanks to Karin for turning out to be such a great friend and person, despite the fact that I thought she was just a rotten little sister. Thanks to my long time friends, Dan Brown and Deirdra Hoolahan, for still talking to me after all those years of me being too busy studying to write them back.

Abstract

Presented here is a measurement of the top quark mass using a sample of $t\bar{t}$ events which decay into a charged lepton, a neutrino, and four jets. This analysis separates the sample of $t\bar{t}$ events into non-overlapping subsamples based on our ability to identify jets which originate from b quark decays. This sample was collected in $p\bar{p}$ collisions at $\sqrt{s} = 1.8$ TeV with the Collider Detector at Fermilab, and corresponds to an integrated luminosity of 109 ± 7 pb^{-1}. The top quark mass is measured to be $175.9 \pm 4.8(stat.) \pm 4.9(syst.)$ GeV/c^2.

Contents

List of Figures

List of Tables

Chapter 1

Theory

1.1 Introduction

Currently, the best understanding of the fundamental constituents of matter and how they interact is expressed in a theory called the standard model [1]. This theory has been tested to the level of a few tenths of a percent over a large range of energies and has been found to provide a remarkably precise description of the subnuclear world over distance scales of several orders of magnitude. When predictions can be made from the standard model, the agreement with experiment has been excellent. One such prediction was the existence of a sixth quark type, named the top quark. This prediction was verified in 1994, when the top quark was discovered by two separate physics experiments at Fermi National Accelerator Laboratory (Fermilab) [2] [3] [4] [5].

The standard model contains a number of free parameters which must be obtained from experimental measurements. For example, all of the fermion masses must be input into the theory. The predictive power of the standard model can be improved by making precision measurements of these parameters. For instance, measurements of the top quark and W boson masses place constraints on the Higgs boson mass.

Despite the wonderful success of the standard model, it does have a number of shortcomings. For example, the standard model does not explain why there are three generations of quarks and leptons, nor does it explain the observed hierarchical pattern of their masses. In particular, it gives no insight into why the mass of the top quark is so much heavier than the other quarks, see Figure 1.1. Other theories, which solve some of the problems of the standard model, have been proposed.

1.2 Standard Model

According to the standard model there are three types of fundamental particles which interact through four forces. The fundamental particles are divided into the leptons, the quarks and the gauge bosons. The forces which govern how these particles interact are called the strong force, the weak force, electromagnetism and gravity. The fourth force, gravity, is not incorporated into the standard model. In addition every particle has an anti-particle which is identical in terms of mass and spin, but has opposite values for other properties, in particular its electric charge. For example, the positively charged positron (e^+) is the anti-particle partner of the electron (e^-).

The leptons consists of 6 distinct types of particles which are paired into three families. Each family is composed of a charged lepton and its associated neutrino. The charged leptons, called electron (e), muon (μ) and tau (τ), each carry an electric charge of -1 and have mass. The electron is the lightest and the tau is the heaviest of the three charged leptons. The electron (ν_e), muon (ν_μ), and tau (ν_τ) neutrinos are electrically neutral and are consistent with being massless.

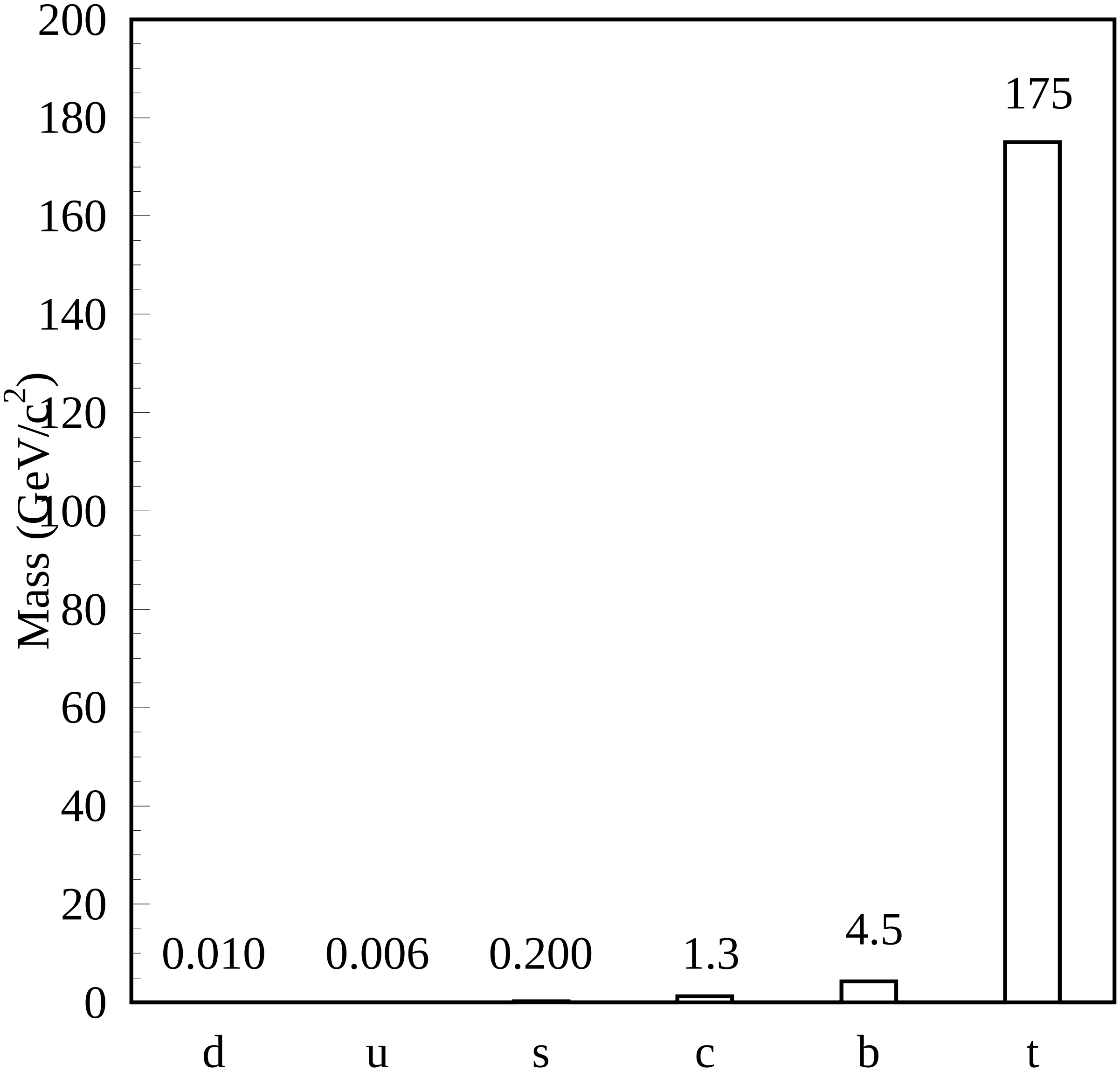

Figure 1.1: The masses, in GeV/c^2, of the down (d), up (u), strange (s), charm (c), bottom (b), and top (t), quarks.

$$\begin{array}{cccc}
 & \textbf{Quarks} & & \textbf{Q} \\
\begin{pmatrix} u \\ d \end{pmatrix} & \begin{pmatrix} c \\ s \end{pmatrix} & \begin{pmatrix} t \\ b \end{pmatrix} & \begin{pmatrix} +2/3 \\ -1/3 \end{pmatrix} \\
 & \textbf{Leptons} & & \\
\begin{pmatrix} e \\ \nu_e \end{pmatrix} & \begin{pmatrix} \mu \\ \nu_\mu \end{pmatrix} & \begin{pmatrix} \tau \\ \nu_\tau \end{pmatrix} & \begin{pmatrix} -1 \\ 0 \end{pmatrix}
\end{array}$$

Table 1.1: The standard model contains two families of six fermions (quarks and leptons) paired in three families. The charge, Q, for each of the fermions is also shown.

Leptons are classified as fermions since they are half integer spin particles and obey Fermi-Dirac statistics. They only participate in interactions of the electromagnetic or weak forces. Table 1.1 lists the three families of leptons and their associated electric charge, Q.

The quarks, like the leptons, are fermions. They come in 6 types, or flavors, called up (u), down (d), charm (c), strange (s), top (t), and bottom (b). The quarks are arranged in three families of weak isospin doublets. Each quark carries an electric charge which is equal to a precise fraction of an electron's charge. Table 1.1 shows the families of quarks and their electric charges. Unlike the leptons, quarks experience strong interactions in addition to electromagnetic and weak interactions. Besides electric charge, each quark also carries a "color" charge of either red, green or blue. This color charge of the strong force is analogous to the electric charge of the electromagnetic force.

The last group of fundamental particles are the gauge bosons. They are called bosons because they have integral spin and obey Bose-Einstein statistics. The gauge bosons are the carriers, or "mediators", of the forces. The electromagnetic force is mediated by the photon. The strong force is mediated by 8 gluons and the weak force is mediated by three vector bosons, W^+, W^- and Z°. A measure of the

Gauge Bosons	**Force**	**Coupling (α)**	**Range**
Photon (γ)	Electromagnetic	10^{-2}	∞
W^+, W^-, Z^0	Weak	10^{-13}	$< 10^{-16}$ cm
Gluon (g)	Strong	1	$< 10^{-13}$ cm

Table 1.2: The standard model contains four vector bosons which carry the electromagnetic, strong and weak forces. The coupling constant (α) is given as the strength at 10^{-13} cm in comparison with the strong force. The range is the average distance over which the forces act.

strength of a force is given by its coupling constant, α, and the average distance over which it acts is given by its range. Table 1.2 lists the mediators, coupling constant, and range for the three forces described by the standard model.

Quarks are bound together through the strong force to form hadrons. There are two types of hadrons: mesons and baryons. Mesons are bosons (have integer spin) comprised of a quark (q) and anti-quark ($\bar{q}$). For example, the π^+ particle is composed of a u quark and a $\bar{d}$ quark. Baryons are fermions (half integer spin) which consist of three quarks or three anti-quarks. For example, the proton is comprised of 2 u quarks and 1 d quark and the neutron is comprised of 1 u and 2 d quarks. The quarks form combinations in which the sum of their electrical charges is an integer and the sum of their color charges is neutral. For example, a meson must consist of a colored quark and an anti-colored anti-quark. A baryon must either consist of a red, blue and green quark or an anti-red, anti-blue and anti-green quark.

The standard model uses gauge theories to mathematically describe how the forces interact with the fundamental particles. Gauge theories are a special class of quantum field theories in which an invariance principle necessarily requires the existence of interactions among the particles. The gauge theory of electromagnetism, called Quantum Electrodynamics (QED), describes the photon-mediated interactions of electrically charged particles. The electromagnetic force is proportional to $1/r^2$, where r is the distance between the interacting particles, and its range is infinite. In QED the electric charge of an interaction must be conserved. Quantum Chromodynamics (QCD), which is modeled after QED, describes the gluon-mediated strong interactions of quarks. The strong force is proportional to r, so as quarks move further and further apart the force binding them together gets stronger and stronger. Like QED, for which electric charge must be conserved, color must be conserved in QCD. Since the quarks carry only one color and color must be conserved, the gluon mediators must carry a color and an anti-color. For example, a gluon may carry red and anti-green.

The gauge theories of the electromagnetic and weak forces have been combined into a single gauge theory called the Electroweak theory. This unification implies that at very short distances and high energies the weak and electromagnetic forces are equal. The Electroweak theory predicts four massless gauge bosons, the W^+, W^-, Z° and the photon (γ). To account for the fact that the W^+, W^-, and Z° bosons are massive, an additional particle, the Higgs, was postulated. At very high energies all fermions and bosons are thought to be massless but at lower energies, interactions with the Higgs boson give the fermions and boson their varying masses. The Higgs boson has not been observed but it is predicted to be a spin zero boson.

1.3 Proton Anti-proton Collisions

Protons (p) and antiprotons ($\bar{p}$) consist of three quarks called the valence quarks. The proton's valence quarks are uud and the antiproton's valence quarks are $\bar{u}\bar{u}\bar{d}$. Other quarks are continually being created and destroyed inside the proton and antiproton. These quarks are called the "sea" quarks. The sea quarks appear as virtual $q\bar{q}$ pairs, being quickly created and annihilated in the vacuum. The proton also consists of a sea of gluons which bind the proton together. Quarks and gluons are sometimes referred to as partons since they are "part" of the proton. At high enough collision energies, the partons of the proton and antiproton are what interact.

In a high-energy proton-antiproton ($p\bar{p}$) collision, a quark (or gluon) from a proton scatters off a quark (or gluon) from the antiproton. As the partons move apart the energy required to separate them increases. Eventually this energy becomes large enough to make it energetically favorable to create a $q\bar{q}$ pair from the vacuum. These new quarks recombine with themselves and with the original quarks to produce hadrons. Quark anti-quarks pairs are continually created until the original interaction energy is dissipated. This process, called hadronization, produces a large number of hadrons which are observed experimentally as a jet. The direction of a jet will be approximately collinear with the parton that initiated it.

Most $p\bar{p}$ collisions involve parton scattering with very low energy transfer. Occasionally an interaction involving large momentum transfer occurs. These are the type of interactions that produce $t\bar{t}$ pairs. In top quark production, the initial partons collide and form a $t\bar{t}$ pair. The top quarks decay and form jets in the detector. In addition to the $t\bar{t}$ pair, gluons are often emitted from the initial or final state partons. These gluons also hadronize and form additional jets in the event. This process is labeled initial or final state radiation depending on the parton from which the gluon radiates.

In $p\bar{p}$ collisions, the components of the initial momenta parallel to the beampipe, the z momenta, of the valence quarks and the composition of the proton sea are unknown. Therefore, the z momenta of the initial partons are also unknown. However, the components of the momenta which are perpendicular to the beampipe, the transverse momenta, of the initial partons should be very close to zero.

Some useful definitions, used throughout this thesis, are given below:

- In the coordinate system used for this thesis, θ and ϕ are the polar and azimuthal angles, respectively, in relation to the proton beam direction, which is the positive z-axis.
- η, pseudorapidity, is defined as

$$\eta = -ln[tan(\theta/2)]$$

- ΔR, is the radius of a cone defined as

$$\Delta R = \sqrt{(\Delta\eta)^2 + (\Delta\phi)^2}$$

- P_T, the transverse momentum of a particle, is the momentum perpendicular to the beam pipe.

$$P_T = Psin\theta$$

  where P is the total momentum of a particle and θ is the angle the particle makes with the beam axis. ($\theta = 0$ is parallel and in the same direction as the proton beam.)

- E_T, the transverse energy, is the energy perpendicular to the beam direction of a particle.

$$E_T = Esin\theta$$

  where E is the total energy of a particle and θ is the angle the particle makes with the beam axis.

- $\not{E}_{\mathrm{T}}$, missing $\mathrm{E_T}$, is the energy that is missed in the detector. Neutrinos rarely interact with material and are therefore hard to detect. Thus their energy is missing and we equate the $\not{E}_{\mathrm{T}}$ in an event with an undetected neutrino. $\not{E}_{\mathrm{T}}$ is the negative of the sum of the transverse energy in the calorimeter, such that $\not{E}_{\mathrm{T}}$ plus the total calorimeter energy sum to zero.

1.4 Top Quark Production and Decay

In $p\bar{p}$ collisions, top quarks are expected to be produced by both $q\bar{q}$ annihilation and gluon-gluon (gg) fusion. Figure 1.2 shows leading order diagrams for $t\bar{t}$ production at the Tevatron. For a top mass greater than 100 GeV/c^2 and center of mass energies near $\sqrt{s} = 1.8$ TeV, $q\bar{q}$ annihilation is expected to be the dominant $t\bar{t}$ production process. In the standard model a top quark decays almost exclusively to a W boson and a b quark. There are other decays possible but these are heavily suppressed since they involve off-diagonal elements of the Cabibbo-Kobayashi-Maskawa (CKM) matrix which are close to zero. (The CKM matrix determines how the quarks mix in their coupling to the W.) There are additional theories that change the standard model predictions and allow for other t-quark decay channels but this analysis considers only the top decay channel $t \rightarrow Wb$. The W boson from the top decay will itself decay into either a lepton and its neutrino or a $q\bar{q}'$ pair. Figure 1.3 shows the Feynman diagram for top quark production by $q\bar{q}$ annihilation and the subsequent top quark decay.

The decay modes of the W boson determine an event's topology and are used as a way to classify the events. Table 1.3 lists the final states of $t\bar{t}$ production, according to the W bosons' decay modes. The events are classified as either an "all-hadronic", "dilepton" or "lepton+jets" event. An event is considered an all-hadronic event when both W bosons decay to a quark-antiquark pair, $t\bar{t} \rightarrow (q\bar{q}'b)$ $(q\bar{q}'\bar{b})$, leading to a fully hadronic state. The signature for a top event in this mode is six or more jets. Though this channel has the largest branching fraction, 44%, it

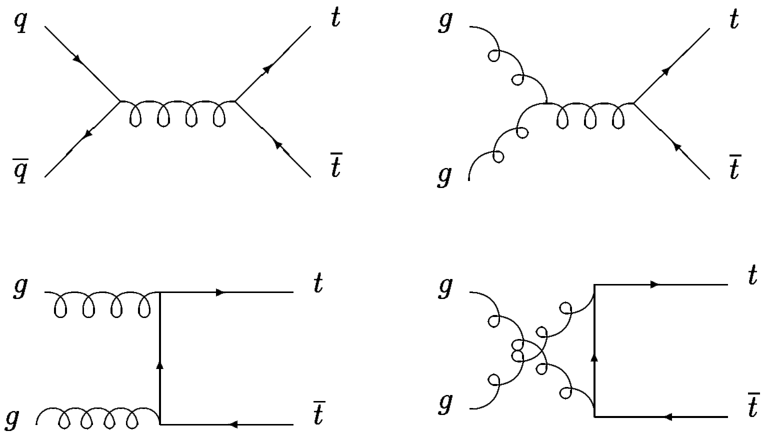

Figure 1.2: The leading order diagrams for $t\bar{t}$ production at the Tevatron.

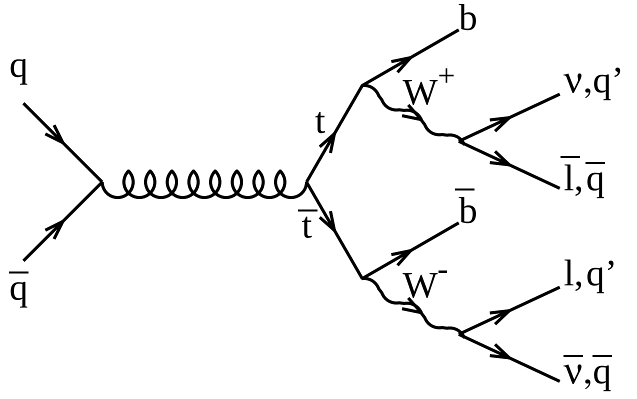

Figure 1.3: The tree-level Feynman diagram for top quark production by $q\bar{q}$ annihilation and standard model top quark decay.

Decay Mode	Branching Ratio
$t\bar{t} \to (q\bar{q}'b)(q\bar{q}'\bar{b})$	36/81
$t\bar{t} \to (q\bar{q}'b)(e\nu\bar{b})$	12/81
$t\bar{t} \to (q\bar{q}'b)(\mu\nu\bar{b})$	12/81
$t\bar{t} \to (q\bar{q}'b)(\tau\nu\bar{b})$	12/81
$t\bar{t} \to (e\nu b)(\mu\nu\bar{b})$	2/81
$t\bar{t} \to (e\nu b)(\tau\nu\bar{b})$	2/81
$t\bar{t} \to (\mu\nu b)(\tau\nu\bar{b})$	2/81
$t\bar{t} \to (e\nu b)(e\nu\bar{b})$	1/81
$t\bar{t} \to (\mu\nu b)(\mu\nu\bar{b})$	1/81
$t\bar{t} \to (\tau\nu b)(\tau\nu\bar{b})$	1/81

Table 1.3: Branching ratios for $t\bar{t}$ decay modes assuming standard model couplings. Here q stands for a u, d, c or s quark.

has a huge amount of background from other QCD multijet production processes. The all-hadronic channel has been described extensively elsewhere [2] [8] [9]. An event is classified as a dilepton event when both W bosons decay leptonically to an e or μ. This channel is identified by two high $\mathrm{P_T}$ leptons and large $\not{E}_{\mathrm{T}}$ from the leptonic decay of both of the Ws, and two jets from the hadronization of the b quarks. The dilepton channel has the least amount of background but a very small branching fraction, $\sim 5\%$. The backgrounds in this mode come from direct $b\bar{b}$, WW, $Z \to \tau\tau$, Drell-Yan production and lepton misidentification. The dilepton decay mode has also been described elsewhere [2] [16].

This analysis focuses on events in which one W decays to a lepton-neutrino pair and the other W decays hadronically. These events are classified as lepton+jets events. The signature for this channel is a charged lepton with high transverse momentum ($\mathrm{P_T}$), an imbalance in energy from the undetected neutrino ($\not{E}_{\mathrm{T}}$), and four or more jets from the hadronized quarks. Decays of W bosons to τ leptons are not explicitly included in this analysis (except when they subsequently decay

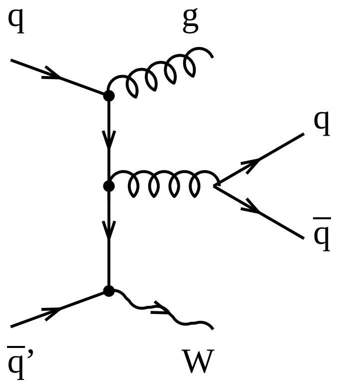

Figure 1.4: The Feynman diagram for W+multijet production which is one of the backgrounds to the top signal.

to an electron or a muon) because of the difficulties associated with identifying the hadronic decays of τ leptons. Requiring one of the W bosons to decay leptonically to an e or μ substantially reduces the amount of background without significantly reducing the branching fraction, $\sim$ 30%. Backgrounds to the lepton+jets channel come predominantly from higher-order production of W bosons, where the W recoils against significant jet activity. This is referred to as "W+multijet" background. Figure 1.4 shows one of the Feynman diagrams for QCD W+multijet production.

As previously mentioned, this analysis only considers the decay channel $t \rightarrow Wb$, so every top event is assumed to have two b quarks. The W+multijet background in the lepton+jets channel can be greatly reduced by identifying, or "b-tagging", at least one of the b quarks in the event. Two different methods of b-tagging are used in this analysis. The first method utilizes the b's lifetime of $\sim$ 1.5 ps. This long lifetime means that the b quark will form a B hadron and travel on average a few millimeters before decaying. B hadrons can be detected experimentally by looking for jets with vertices displaced from the primary vertex of the event. The second technique is to search in the event for additional leptons coming from the semileptonic decays of B hadrons. Chapter 4 explains both *b*-tagging methods in more detail.

1.5 Top Mass

The top quark is a recently discovered fundamental particle whose properties should be measured to the greatest precision possible. One property, the top quark mass (M_{top}), is an important standard model input parameter. It is present in radiative corrections which connect several other standard model parameters. By measuring the top mass very accurately, global fits combining M_{top} and other experimental information can be used to test for consistency and predict unknowns of the standard model. One of the most notable predictions that can be made is that of the unknown mass of the Higgs boson, M_H. Direct, precision measurements of the mass of the W boson (M_W) and of the top quark (M_{top}), provide an indirect constraint on the Higgs boson mass, M_H, via top quark and Higgs boson electroweak radiative corrections to M_W. Figure 1.5 shows the standard model predictions for various Higgs boson masses (indicated by the shaded bands) as a function of M_W and M_{top}.

Previous direct measurements of the top mass in the lepton+jets channel at CDF obtain a value of $\sim$ 175 GeV/c^2 [2] [3]. In the limit $\mathrm{M}_{top} >> \mathrm{M}_b$, $\mathrm{M}_W >> \mathrm{M}_b$, and assuming only three generations of quarks ($|\mathrm{V}_{tb}| = 1$) the partial width for the decay ($t \rightarrow Wb$) is given by [6]

$$\Gamma(t \rightarrow Wb) \quad \approx \quad 175\ MeV \left(\frac{M_{top}}{M_W}\right)^3$$

A top quark with mass 175 GeV/c^2 should have a width of nearly 2 GeV and

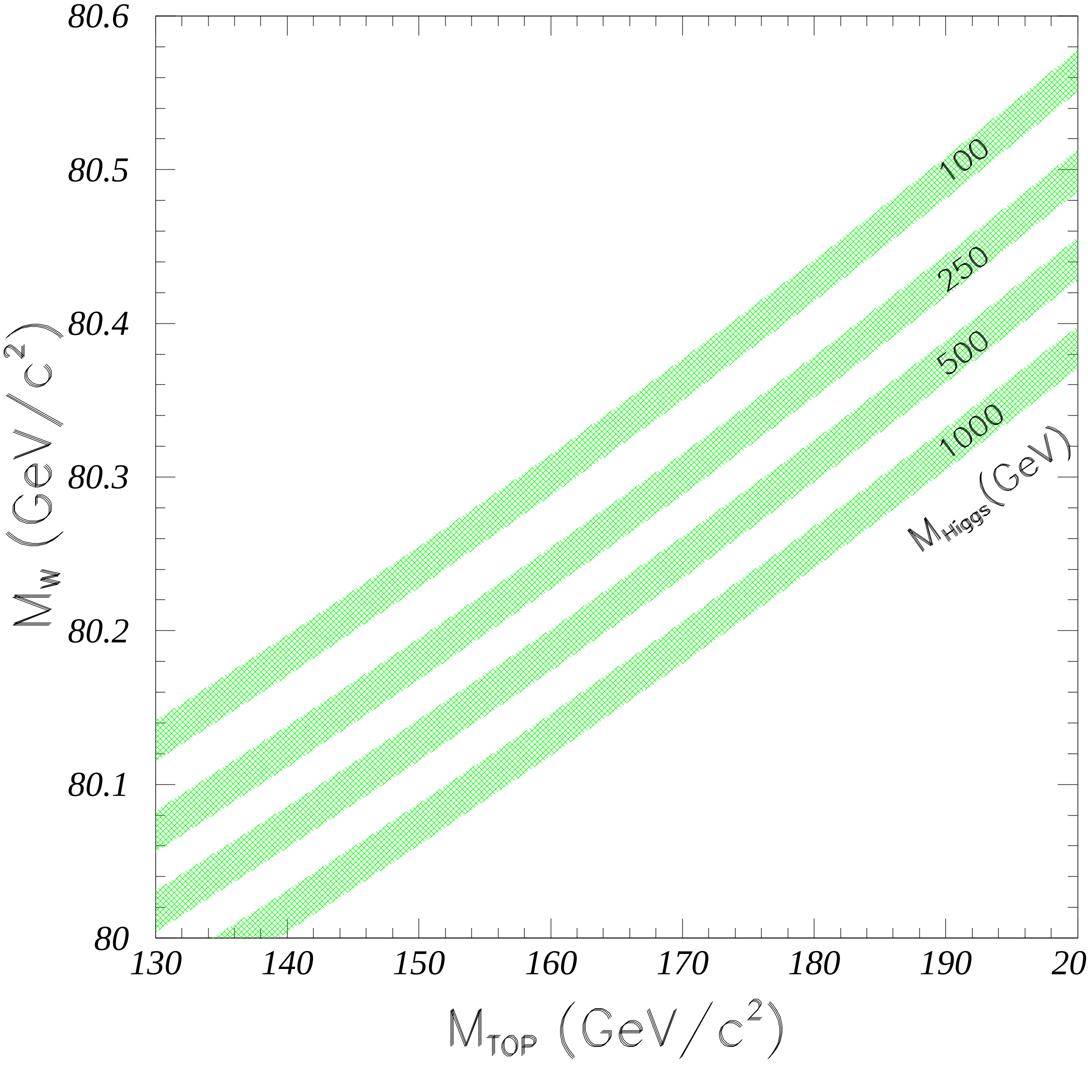

Figure 1.5: The standard model predictions for various Higgs boson masses (indicated by the shaded bands) are shown as a function of the W mass (M_W) and the top quark mass (M_{top}). The width of the shaded bands is due primarily to the uncertainty in the electromagnetic coupling constant at the Z mass scale, $\alpha(M_Z)$, which has been assumed to be $\delta\alpha(M_Z) = 0.0004$.

a lifetime of $\sim 4 \times 10^{-25}$ seconds. This means that the top quark travels only ~ 0.04 fm before it decays. While the hadronization process is not particularly well understood, it has been argued that hadronization does not occur before the outgoing quarks are more than ~ 1 fm apart. At this distance, the stretched color string is expected to break producing $q\overline{q}$ pairs out of the vacuum which can combine with the quarks to form hadrons. Since the top quark travels < 1 fm, it is expected to decay before forming a hadron. However, because the top is so heavy, the decay of a free top quark and a top hadron are not expected to be differentiable in current experiments [7].

1.6 Overview of the Analysis

Since the discovery of the top quark, its mass has been measured in each of the W decay channels; all-hadronic, dilepton and lepton+jets. In the all-hadronic mode each event consists of 6 jets, two from the b quarks and 4 from the hadronic decay of the W bosons. This channel has the advantage of having a one to one correspondence between the top decay partons and the experimentally observed jets. The disadvantage of this channel is the large QCD+multijet background which makes it difficult to isolate top events from background events. The all-hadronic mass measurement is described in detail elsewhere [10] [8]. Measuring the top quark mass from dilepton decays is particularly challenging due to the presence of two neutrinos in the final state. The signature of a dilepton event is two jets from the b quarks, and two leptons and a large amount of missing energy from the leptonic decay of the W bosons. Since the energy of the neutrinos must be inferred from the total amount of missing energy in the detector, an individual event does not contain sufficient information to solve for a unique top mass. Additional outside information must be used when fitting dilepton events to a top mass [11]. Presently, the most accurate technique for measuring the top mass at Fermilab uses the lepton+jets channel and is described in this thesis. In the lepton+jets mode, the $t\bar{t}$ event can be completely reconstructed, as in the all-hadronic mode, but with a much higher purity for top events. Previous measurements from CDF in the lepton+jets channel can be found elsewhere [2] [3].

To measure the mass of the top quark, first a sample of lepton+jets top events must be identified. Chapter 2 gives a brief description of the apparatus used in this thesis, the CDF detector. Chapter 3 describes how a sample of top events is identified. Chapter 4 describes how CDF tags b quarks to help distinguish between top and background and how the backgrounds to top are calculated. Chapter 5 details how the top mass is measured using a constrained event fitting technique and a maximum likelihood method. Chapter 6 describes how the systematic uncertainty on the top mass measurement was obtained. The conclusions are given in Chapter 7.

Chapter 2

Experimental Apparatus

2.1 The Tevatron

The Fermilab Tevatron collider is a large superconducting magnetic accelerator that collides bunches of protons (p) and antiprotons ($\bar{p}$). This accelerator, with a radius of 1.0 km, operates with 6 bunches of 900 GeV protons colliding with 6 bunches of 900 GeV antiprotons. The produced collisions have a total center-of-mass energy of 1.8 TeV. A diagram of the Fermilab Tevatron Accelerator is shown in Figure 2.1.

A series of steps are needed to produce the 900 GeV bunches of protons and antiprotons. The process for producing the protons starts with a bottle of H_2 gas. Two electrons are added to the hydrogen to make H^- ions. The ions are accelerated to 750 kV by a Cockcroft-Walton electrostatic accelerator and then to 400 MeV in a 150 m linear accelerator, the Linac. At the end of the Linac, the ions are passed through a copper foil to remove the electrons giving a bare proton. The protons are then put into a 475 m circumference synchrotron accelerator, the Booster, which accelerates the protons to 8 GeV. From the Booster, the protons are

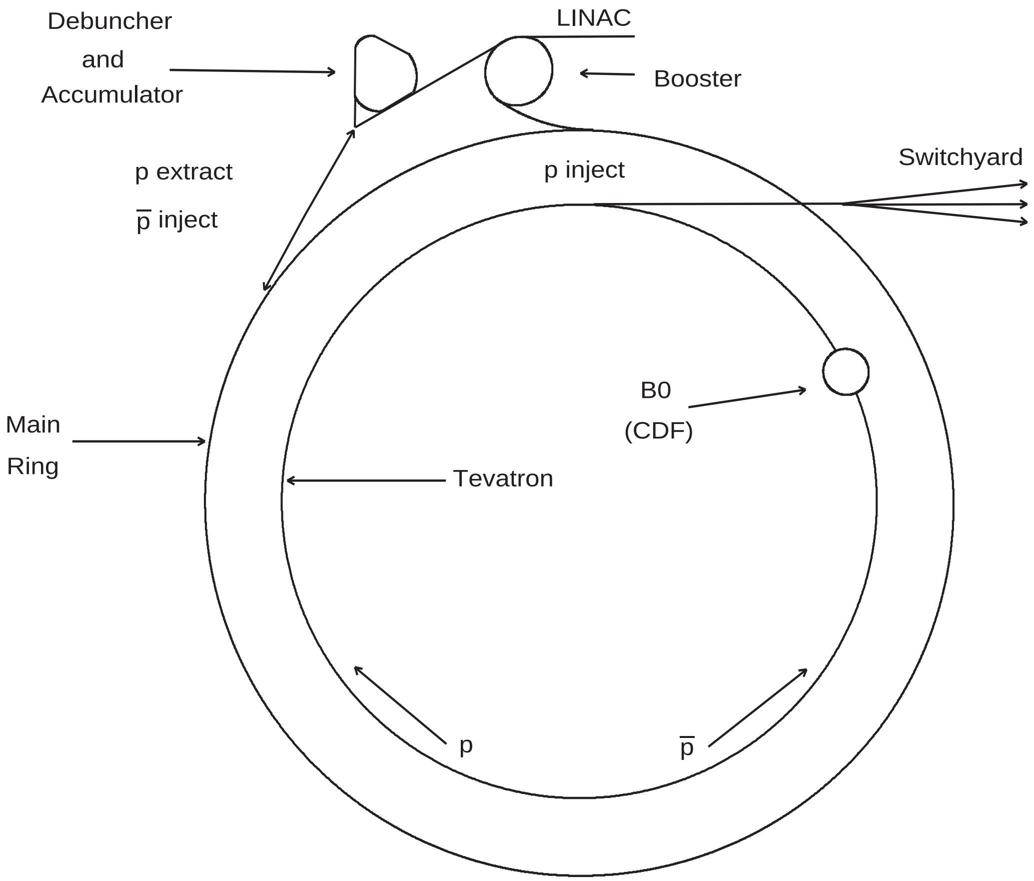

Figure 2.1: Diagram of the Tevatron accelerator complex.

injected into the Main Ring. The Main Ring is a 6.3 km circumference synchrotron that accelerates the protons to 150 GeV. The Main Ring magnets are capable of generating magnetic fields up to 0.7 T to keep the protons in the ring. After reaching an energy of 150 GeV, the protons are coalesced into a single bunch and injected into the Tevatron. The Tevatron is composed of superconducting magnets which reside directly below the Main Ring magnets. The superconducting magnets can generate magnetic fields from 0.66 T to 4.4 T. The Tevatron accelerates the protons to the colliding energy of 900 GeV. The entire process described above takes approximately one minute.

The process of producing antiprotons ($\bar{p}$) is more complex. A beam of 120 GeV protons is taken from the Main Ring and focused onto a tungsten target. A spray of particles is produced from which the antiprotons are selected and focused with a lithium lens. The antiprotons are then passed to the Debuncher where they are stochastically cooled to reduce the phase space of the beam. From the Debuncher, the antiprotons are transferred to a concentric ring, called the Accumulator, where they are stored. The antiprotons are "stacked" at a rate of 4×10^{10} per hour until approximately 100×10^{10} antiprotons have been stored. Now the process of colliding beams of protons and antiprotons can begin.

Six bunches of protons are injected into the Tevatron, each bunch having approximately 2×10^{11} particles. After the protons are in the Tevatron, six bunches of antiprotons are taken from the Accumulator, and reverse injected into the Main Ring. Each bunch of antiprotons contains approximately 5.5×10^{10} particles. After the antiprotons reach an energy of 150 GeV they are injected into the Tevatron, circulating in the opposite direction of the protons. The transfer efficiency between the Accumulator and the Tevatron is low for antiprotons so by the time they reach the Tevatron a bunch of antiprotons typically has 30×10^{9} particles. The proton and antiproton bunches travel within the same beampipe but in opposite directions. They share the same magnetic and RF fields and travel in counter-rotating helical orbits.

There are two interaction regions at the Tevatron, B0 and D0, where the beams are made to collide by focusing them with quadrupole magnets. By colliding two beams, each with energies of 900 GeV, the center-of-mass energy available at the collision point is 1.8 TeV. Detectors enclose these interaction regions. Ideally the collisions would take place at the center of the detectors, but the actual collision point is a gaussian distribution with a width in the x and y planes of 35 μm and a width in the z plane, along the beam axis, of 30 cm. The beams traverse the Tevatron at approximately the speed of light, which means that the bunch crossings occur in the interaction regions roughly every 3.5 μs. The beams are typically left to collide, “run”, in the machine for $\approx$ 10 hours. While the Tevatron is running, antiprotons are being stacked using the Main Ring. More detailed information about the Tevatron can be found in references [12] [13].

The instantaneous luminosity (L) of the Tevatron can be obtained with the following equation:

$$L = \frac{N_p N_{\bar{p}} B f_0}{4\pi\sigma^2} \tag{2.1}$$

where N_p is the total number of protons per bunch, $N_{\bar{p}}$ is the total number of antiprotons per bunch, B is number of bunches of each type, f_0 is the frequency of bunch revolution, and σ^2 is the cross-sectional area of the bunches ($\sigma^2 \sim 5 \times 10^{-5}\ cm^2$). The instantaneous luminosity of the accelerator falls exponentially with time due to transverse spreading of the beam and losses from collisions. To give an idea of the performance of the Tevatron, the best instantaneous luminosity and the typical instantaneous luminosity for two data runs are given below:

- Run IA - August 1992 to May 1993
    - Best instantaneous luminosity was $0.92 \times\ 10^{31}\ cm^{-2}\ s^{-1}$.

  - Typical instantaneous luminosity was $0.54 \times\ 10^{31}\ cm^{-2}\ s^{-1}$.

- Run IB - January 1994 to July 1995
  - Best instantaneous luminosity was $2.8 \times\ 10^{31}\ cm^{-2}\ s^{-1}$.
  - Typical instantaneous luminosity was $1.6 \times\ 10^{31}\ cm^{-2}\ s^{-1}$.

2.2 The CDF Detector

The Collider Detector at Fermilab (CDF) is located at the B0 interaction region of the Tevatron. The CDF detector is a multipurpose detector which is designed to observe particles produced from high-energy $p\bar{p}$ collisions. Specifically, it is used to identify and measure the energy and momentum of electrons, muons, photons and jets. Jets are sprays of particles which come from the decay of quarks and gluons created in the $p\bar{p}$ collision. A quarter view schematic drawing of the detector is shown in Figure 2.2, where the interaction point is in the lower righthand corner. CDF is cylindrically and forward-backward symmetric about the transverse plane that passes through the interaction point.

The coordinate system used by CDF is centered on the interaction point. The positive z axis points along the beamline in the direction of the protons, the x-axis points horizontally toward the center of the ring and the y-axis points upwards. In terms of angles, θ is the polar angle, and ϕ is the azimuthal angle. Typically, locations of particles are identified by the Lorentz invariant quantity of pseudorapidity, η. Pseudorapidity(η) is defined in terms of the polar angle by the relation $\eta = -ln[\tan(\ \theta/2)]$.

The overall design of the CDF detector is dictated by the manner in which different types of particles interact with matter. CDF is composed of a variety of smaller detector segments. The detector can be viewed as being made up of

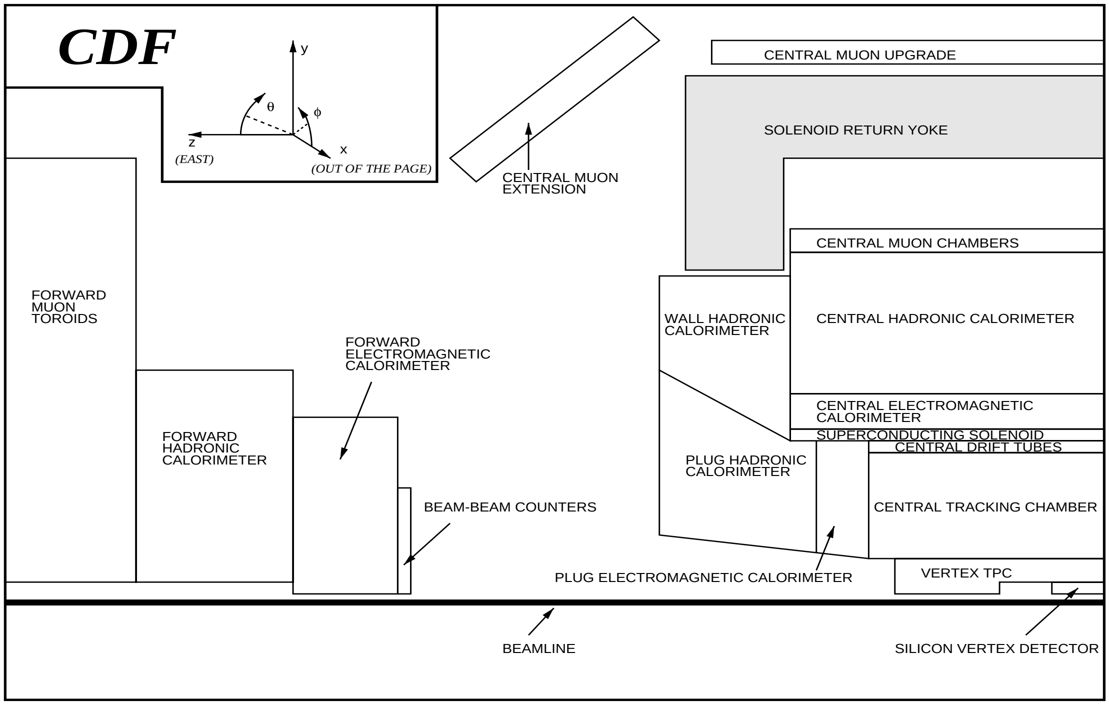

Figure 2.2: A side-view cross section of the CDF detector. The detector is forward-backward symmetric about the interaction region, located at the lower righthand corner of the figure. The detector components are described in the text.

three main functional sections; the tracking chambers, the calorimeters and the muon chambers. Starting from the interaction point and moving radially outward, the tracking system is located inside of a 1.5 m radius superconducting solenoid which produces a 1.4 T axial magnetic field. The magnetic field causes the trajectory of a charged particle to bend within the tracking chambers. The curvature of the trajectory, or "track", is used to measure the momentum of the particle. The calorimeters surround the tracking chambers and are used to measure the electromagnetic and hadronic energy of electrons, photons and jets. The outermost detectors are the muon detectors. Layers of steel outside of the calorimeters are used to absorb any remaining hadrons, leaving only muons which can then be cleanly identified by the muon chambers. The following sections will give a brief overview of the detector components which are important to this analysis. A more complete description of CDF can be found elsewhere [14].

2.2.1 The Tracking Detectors

The CDF tracking system consists of three separate tracking chambers: the Silicon Vertex Detector (SVX), the Vertex Time Projection Chamber (VTX), and the Central Tracking Chamber (CTC). All three of these detectors lie within the 1.4 T magnetic field. Each component is designed to perform a particular task. The SVX, which is closest to the beampipe, has the best position resolution and is used to identify the displaced vertices indicating the decay of a B hadron. The VTX surrounds the SVX and is primarily used to identify the z position of an event's interaction point, its "vertex". Surrounding the VTX is the CTC. The CTC was designed for the precise measurement of a charged particle track's momentum and to give good two track separation.

The Silicon Vertex Detector (SVX) provides precise $r - \phi$ information for the reconstruction of charged particle tracks. A detailed description of the detector and its performance can be found elsewhere [15]. The SVX consists of two barrels that are aligned end-to-end along the beampipe. There is a 2.15 cm gap between the two barrels at z=0. The total active length of the detector is 51 cm which gives a pseudorapidity coverage of $|\eta| < 1.9$. Since $p\bar{p}$ collisions occur with a spread of $\sigma \sim 30$ cm about z=0, the track acceptance of the SVX is $\sim 60\%$. Each barrel is divided into 12 azimuthal wedges of 30° and four concentric layers of silicon strip detectors, see Figure 2.3. The innermost layer is at a radius of 2.86 cm and the outermost layer is at a radius of 7.87 cm, from the beampipe. Each ladder has three 8.5 cm long single-sided silicon strip detectors with its readout strips running parallel to the beam line. The strips on the inner three layers have a 60 μm pitch, while the outermost layer has a 55 μm pitch. The single hit resolution per layer is approximately 13 μm with a 96% hit efficiency per layer. The SVX has a total of 96 ladders. The ladders are read out by readout chips with each chip responsible for 128 channels (strips). There are a total of 46080 channels for the entire SVX detector. This is nearly one third of all the channels for the whole CDF detector. The channels for each wedge are read out in parallel and in sparse mode, meaning that only channels which register a hit are read out. About 5% of the SVX channels are read out for an event. The SVX has one of the longest readout times in CDF with a typical event taking 2 ms. The physical properties of the SVX are summarized in Table 2.2.1.

Due to the high luminosities at the Tevatron, there is frequently more than one interaction per event. The Vertex Time Projection chamber (VTX) is used to associate a track to its correct vertex along the beamline. The VTX is composed of 8 octogonal gas chambers which are segmented azimuthally. The chambers use a 50% - 50% mix of argon and ethane gas. The detector is 2.8 m long in z and extends from an inner radius of 8 cm out to a radius of 22 cm from the beampipe.

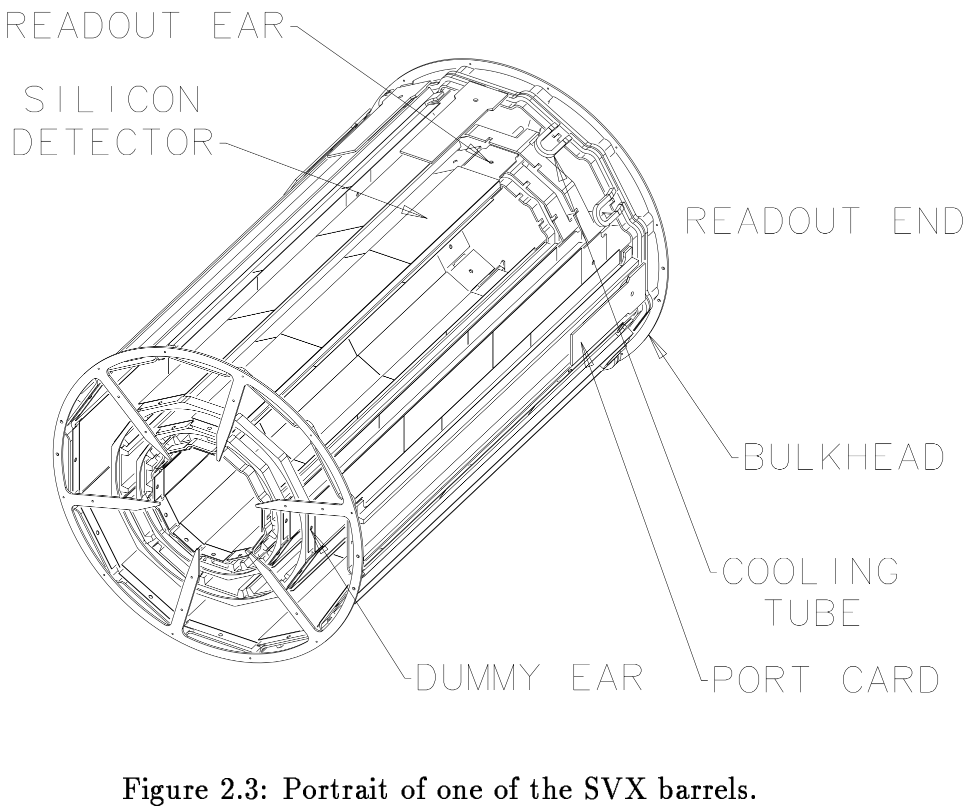

Figure 2.3: Portrait of one of the SVX barrels.

The sense wires in the chambers run radially outward from the beamline providing tracking information in the $r - z$ plane for $|\eta| < 3.5$. The endcaps consist of wires perpendicular to the beamline and the radial centerline of the wedges. Charged particles passing through the VTX ionize the gas and free electrons which drift in the axial direction to the sense wires. The axial drift time of an electron in a module provides the track position in the $r - z$ plane. The wire position gives radial information and the time of arrival to each wire position gives z information. This information for multiple tracks is used to locate the primary vertex of the event. The uncertainty in the measurement of the z coordinate of the vertex is 1 mm. Table 2.2.1 summarizes the physical characteristics of the VTX.

The Central Tracking Chamber (CTC) is a large cylindrical open-wire drift chamber that measures the transverse momentum of a charged particle by determining the curvature of its path in the 1.4 T magnetic field. The CTC is 3.2 m long in z, with an inner radius of 0.3 m and an outer radius of 1.3 m, giving coverage over the pseudorapidity range of $|\eta| < 1.0$. The CTC is comprised of sense wires running the length of the chamber. There are 84 layers of wires which are grouped into nine superlayers. The superlayers are divided into two types of alternating cells, axial and stereo. The five axial layers are cells of 12 sense wires which run parallel to the beamline and provide tracking information in the $r - \phi$ plane. The four stereo layers are cells of 6 sense wires which are offset by an angle of $\pm 3^\circ$ from the beamline. The stereo layers provide tracking information in the $r - z$ plane. The combination of the axial and stereo layers gives 3-dimensional tracking. The field wires of the CTC create a 1350 V/cm drift field. To compensate for the Lorentz angle produced by the crossed electric and magnetic fields the wires in each superlayer are grouped into cells which are tilted by 45° with respect to the radial direction. This gives drift electrons trajectories which are perpendicular to the radial direction and simplifies track reconstruction. Figure 2.4 shows a transverse view of the CTC endplate. Tracks are reconstructed by fitting hits in the CTC to a helix. The curvature of the track is related to the transverse momentum of the particle. The momentum resolution of the CTC is

$$\delta P_T/P_T = 0.002 GeV^{-1} \times P_T.$$

By combining tracking information from the CTC and the SVX, the momentum resolution improves to

$$\delta P_T/P_T = 0.001 GeV^{-1} \times P_T.$$

The CTC is also able to determine the identity of the particle by measuring the ionization rate of the particle's track. The physical properties of the CTC are listed in Table 2.2.1.

2.2.2 Calorimetry

Particles with transverse momentum greater than 350 MeV are able to escape the magnetic field and be detected by the calorimeters which surround the solenoid. CDF has two types of calorimeters: electromagnetic and hadronic. Both types of calorimeters consist of layers of an absorbing material alternating with layers of an active material. The absorbing layers cause the incident particle to interact and form a shower. The active material measures the particle's energy by sampling the energy flow as a function of depth. Electromagnetic showers develop faster than hadronic showers, therefore the electromagnetic calorimeters are positioned in front of the hadronic calorimeters. In this analysis the calorimeters are used to determine the energy and direction of the jets, measure the amount of missing energy ($\not{E}_{\mathrm{T}}$) in the event, and aid in identifying electrons and muons.

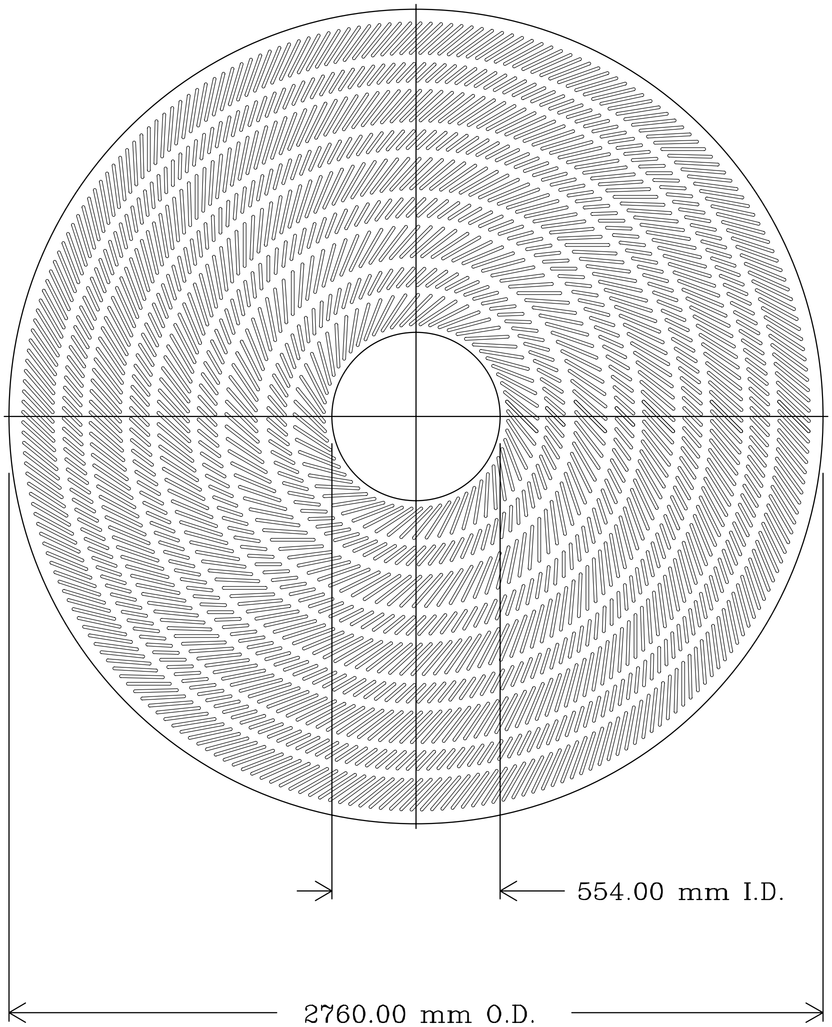

Figure 2.4: Transverse view of the CTC endplate illustrating the 9 superlayer geometry. The wire planes are tilted 45° relative to the radial to account for the Lorentz angle of the ionization drift velocity.

	Central tracking chamber (CTC)	Vertex tracking chamber(VTX)	Silicon vertex detector (SVX)
Polar Angle Coverage	$\|\eta\| < 1.5$	$\|\eta\| < 3.25$	$\|\eta\| < 1.2$
Inner, Outer Radii (cm)	30.9, 132.0	8, 22	2.7, 7.9
Length (cm)	320	280	26
Layers	60 axial, 24 stereo	24	4
Strip/Wire Spacing	10 mm	6.3 mm	60 μm (inner 3 layers) 55 μm (outer layer)
Spacial Resolution	200μm $(r - \phi)$ 4 mm $(r - z)$	200-500 μm $(r - z)$	15 μm $(r - \phi)$
Momentum Resolution	$\delta P_T/P_T = 0.002 \times P_T$		$\delta P_T/P_T = 0.001 \times P_T$
Thickness	$\approx 0.015X_0$	$\approx 0.0045X_0$	$\approx 0.035X_0$

Table 2.1: Description of the charged particle tracking chambers.

The calorimeters are segmented into towers in $\eta - \phi$ space and point back to the geometric center of the detector (x=y=z=0). The calorimeters surround the solenoid and tracking chambers and cover a range of 2π in azimuth and -4.2 to 4.2 in pseudorapidity. The calorimetry consists of three subsystems which are separated into pseudorapidity regions: the central ($|\eta| < 1.1$), plug ($1.1 < |\eta| < 2.4$), and forward ($2.4 < |\eta| < 4.2$) calorimeters.

Central Calorimeters

The central electromagnetic (CEM) and hadronic (CHA) calorimeters are divided into towers covering 15° in azimuth and 0.1 units in pseudorapidity. The central calorimeter has 48 wedges each containing 10 towers. The electromagnetic section is made of alternating layers of lead and polystyrene scintillator. The hadronic section is made of alternating layers of iron and scintillator. Particles traveling through the calorimeter produce light in the scintillator which is collected by acrylic lightguides and transmitted to photomultiplier tubes located at the back of each wedge. A cutaway cross-section view of a central calorimeter wedge is shown in Figure 2.5.

The CEM has 18 radiation lengths worth of material and an inner radius of 173 cm with a depth of 35 cm. The CHA contains 4.7 absorption lengths of material and extends beyond the CEM. The layout of the central calorimeter is shown in Figure 2.6. The measured energy resolution for electromagnetic showers is

$$(\sigma/E)^2 = (13.7\%/\sqrt{E_T})^2 + (2\%)^2.$$

The CEM was originally calibrated using testbeam electrons and is checked periodically using ^{137}Cs sources. The energy resolution for hadronic showers was

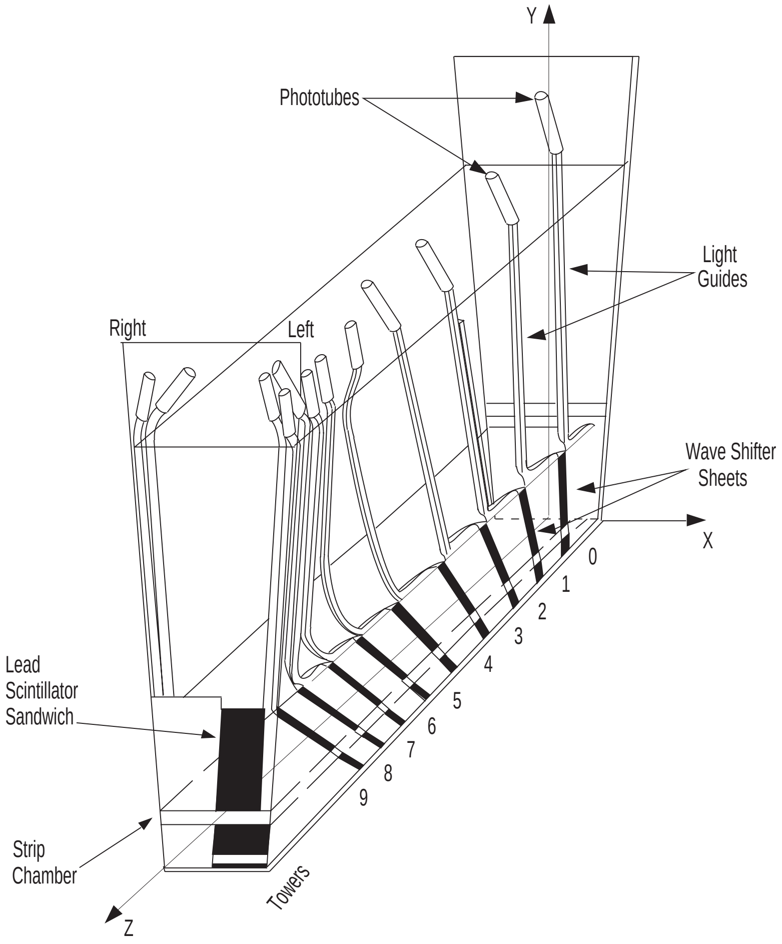

Figure 2.5: Diagram of a single central calorimetry wedge.

	Central EM (CEM)	Hadron (CHA)	Endwall Hadron (WHA)
Coverage ($\|\eta\|$)	0 - 1.1	0 - 0.9	0.7 - 1.3
Tower Size ($\delta\eta \times \delta\phi$)	$0.1 \times 15^\circ$	$0.1 \times 15^\circ$	$0.1 \times 15^\circ$
Module Length	250 cm	250 cm	100 cm
Module Width	15°	15°	80 cm
Number of Modules	48	48	48
# Layers	31	32	15
Active Medium	polystyrene scintillator	acrylic scintillator	acrylic scintillator
Thickness	0.5 cm	1.0 cm	1.0 cm
Absorber	Pb	Fe	Fe
Thickness	0.32 cm	2.5 cm	5.1 cm

Table 2.2: Characteristics of the central and endwall calorimeters.

measured from isolated pions to be

$$(\sigma/E)^2 = (50\%/\sqrt{E_T})^2 + (3\%)^2.$$

Particles in the region $0.6 < |\eta| < 1.1$ do not pass through all layers of the CHA so an additional hadronic calorimeter, the endwall hadronic calorimeter (WHA), was added. Table 2.2.2 gives detailed information on the central calorimeters.

To enable a more precise measurement of the transverse profile of an electromagnetic shower, a proportional strip and wire chamber (CES) was embedded in the central calorimeter at approximately the position of maximum electromagnetic shower deposition ($\sim$6 radiation lengths). Cathode strips running in the azimuthal direction provide z information, while anode wires running in the z direction provide $r - \phi$ information. The position resolution of the CES is approximately 2 mm in each direction for 50 GeV electrons.

In addition to the CES, a set of proportional tubes (CPR) were placed in the

	Plug EM (PEM)	Hadron (PHA)	Forward EM (FEM)	Hadron (FHA)
Coverage($\|\eta\|$)	1.1 - 2.4	1.3 - 2.4	2.2 - 2.4	2.3 - 2.4
Tower Size ($\delta\eta \times \delta\phi$)	$0.09 \times 5^\circ$	$0.09 \times 5^\circ$	$0.1 \times 5^\circ$	$0.1 \times 5^\circ$
Active Medium	Proportional cathode	tube pad	chambers readout	with
Tube Size	0.7×0.7 cm^2	1.4×0.8 cm^2	1.0×0.7 cm^2	1.5×1.0 cm^2
# Layers	34	20	30	27
Absorber	Pb	Fe	94% Pb, 4% Sb	Fe
Thickness	0.27 cm	5.1 cm	0.48 cm	5.1 cm

Table 2.3: Characteristics of the plug and forward calorimeters.

central region between the solenoid and the CEM. The CPR acts as a preradiator and aids in distinguishing electrons from hadrons. Electrons are likely to react in the solenoid coil and will result in depositing several particles in the CPR. Hadrons are less likely to react and should leave little or no energy in the CPR.

Plug and Forward Calorimeters

The plug and forward calorimeters are used in this analysis to measure the energies of forward jets and help determine the missing transverse energy ($\not{E}_{\mathrm{T}}$) of the event. The plug and forward calorimeters are divided into electromagnetic (PEM,FEM) and hadronic (PHA,FHA) sections. The plug and forward calorimeters use gas instead of scintillating material as their active medium. Table 2.2.2 lists detailed characteristics of the plug and forward calorimeters.

The plug and forward calorimeters consists of layers of proportional tubes which use a 50% - 50% mixture of argon and ethane gas as the active medium. Each tube contains a wire, the anode, at high voltage inside a resistive plastic tube.

The cathode is made of copper clad G-10 boards. The copper pads form the tower segmentation for the calorimeter. Particles passing through the detector ionize the gas in the tubes. Electrons produced by the ionization of the gas drift to the wire and induce a charge on the cathode pads. The charge is amplified and read out to give a measure of the energy of the shower. The energy resolution of the PEM from testbeam electrons is

$$(\sigma/E)^2 = (22\%/\sqrt{E})^2 + (2\%)^2.$$

The energy resolution for the PHA determined from pions in the testbeam is

$$(\sigma/E)^2 = (90\%/\sqrt{E})^2 + (4\%)^2.$$

The energy resolution from testbeam electrons for the FEM is

$$(\sigma/E)^2 = (26\%/\sqrt{E})^2 + (2\%)^2.$$

The energy resolution from testbeam electrons for the FHA is

$$(\sigma/E)^2 = (137\%/\sqrt{E})^2 + (4\%)^2.$$

2.2.3 The Muon Detectors

Muons are detected at CDF with arrays of drift tubes that are placed outside of the calorimeters. The lead and steel of the central calorimeters act as a filter for hadrons and prevents most non-muon particles from reaching the muon chambers. CDF has three separate muon detectors: the central muon detector (CMU), the central muon upgrade (CMP), and the central muon extension (CMX). All of the muon chambers are single wire, rectangular drift tubes.

The CMU is located inside the central calorimeter wedges, directly behind the CHA, and covers the pseudorapidity range $|\eta| < 0.6$. The CMU has only 85% coverage in ϕ due to 2.4° gaps between detector modules. Figure 2.6 shows the placement of the CMU detectors in the central calorimeter. Each central calorimeter wedge contains three CMU towers with each tower containing four radial layers of four drift tubes. The layers are offset from one another by half a cell width ($\sim$ 2 mm) to remove any ambiguity of which side the particle passed the wires in ϕ.

An additional 0.6 m of steel was added behind the central calorimeter to further reduce the number of hadrons which "punched-through" the CMU. Four more layers of drift chambers were also added called the central muon upgrade (CMP). The CMP also has drift tubes with alternate layers staggered by half a cell width to avoid gaps in coverage and left-right ambiguities. For $|\eta| < 0.6$, approximately 85% of the solid angle is covered by the CMU, 63% by the CMP, and 53% by both.

Muon detection was also extended in the $0.6 < |\eta| < 1.0$ region with the addition of four free standing conical arches of drift tubes called the central muon extension (CMX). The CMX is sandwiched between two layers of scintillators (CSX) which aid in identifying real muons. The CMX covers 71% of the solid angle in the $0.6 < |\eta| < 1.0$ region. The forward section of the detector also has muon detectors, the forward muon chambers (FMU). The FMU is a toroidal muon spectrometer and is located behind the forward calorimeter. The FMU detector was not used for this analysis.

The total integrated luminosity delivered to CDF is calculated by counting the soft interactions between two partons, called minimum bias events. Minimum bias events are the most frequent type of $p\bar{p}$ interaction at the Tevatron and account for almost all of the interactions. These events generate a spray of particles which leave the interaction point at small angles relative to the beam axis. CDF counts the minimum bias events by using small angle scintillating counters called the Beam Beam Counters (BBC). The BBC counters cover an angular region of 0.32° to 4.47° in both the forward and backward directions. The BBC counters look for at least one track on opposite sides of the detector which are at small angles to the beampipe. Coincident hits in the forward and backward BBC counters are used to calculate the instantaneous luminosity at CDF. The instantaneous luminosity is then integrated over time to obtain the total delivered luminosity to the CDF detector. During Run IA and Run IB, CDF measured its integrated luminosities to be 19.3 pb^{-1} and 90.1 pb^{-1}, respectively.

2.2.4 The Trigger System

At CDF, beam crossings occur roughly once every 3.5 μs with an average of one interaction per crossing during Run IA and three interactions per crossing during Run IB. With an event rate of 280 kHz it is impossible to record every interaction. CDF employes a three level trigger system to reduce the event rate down to a manageable level. The goal of the trigger is to maximize the number of interesting events written to tape but minimize the amount of "dead-time", time during which the detector does not acknowledge new interactions. Each level of the trigger is a logical OR of many separate triggers which select events that have electrons, muons, or jets. Each successive level of the trigger processes fewer events than the preceding level but with greater sophistication and more processing time. CDF's Level 1 and Level 2 triggers are implemented in hardware, while Level 3 is implemented in software.

The Level 1 trigger is deadtimeless, taking less than 3.5 μs to make its decision.

The trigger is based on identification of energy clusters in the calorimeters or muon tracks in the muon chambers. Level 1 reduces the event rate from 280 kHz down to 1 kHz. Electrons and jets are selected at Level 1 with a calorimetry trigger which requires a single trigger tower (defined as $\Delta\eta \times \Delta\phi = 0.2 \times 15^\circ$ sections of the calorimeter) to have energy over a given threshold. The Level 1 muon triggers require a pair of hits in two parallel muon drift tubes. No tracking information is available at this level.

The Level 2 trigger makes use of tracking information and more sophisticated calorimeter information. The central fast tracker (CFT) is a hardware processor that uses CTC hits to reconstruct high momentum tracks in $r - \phi$. The CFT has a momentum resolution of $\delta P_T/P_T^2 = 3.5\%$. Calorimeter clusters are formed by searching for a seed tower above a certain threshold and adding in neighboring towers which are over a lower threshold. The $\mathrm{E_T}$, η, and ϕ are calculated for each energy cluster. Track segment information from the CMP, CMU and CMX detectors is also available. Tracks found by the CFT are matched to clusters in the CEM to form electron candidates or to tracks in the muon chambers to form muon candidates. Level 2 takes $\sim 20\ \mu s$ to make a decision during which time the detector ignores subsequent crossings. Therefore Level 2 incurs a dead time of a few percent. The event rate out of level 2 is approximately 20 to 35 Hz.

The Level 3 trigger is a software reconstruction trigger which is run on a farm of Silicon Graphics processors. The trigger software reconstructs events using a simplified version of the "offline" code. Level 3 implements two dimensional tracking instead of the three dimensional tracking which is used offline. All events which pass the Level 3 trigger are written to 8 mm tape with a typical output rate being 3 - 5 Hz for Run IA and 8 Hz for Run IB.

2.2.5 Offline Reconstruction

The events which pass the level three trigger are written to tape and then processed offline with full CDF event reconstruction code. This code performs full three-dimensional tracking in the CTC and identifies jets, and electron and muon candidates.

Jets are formed by finding clusters of energy in the calorimeter. The cluster starts with a seed tower which has transverse energy ($\mathrm{E_T}$) of at least 3 GeV. Neighboring towers which have $\mathrm{E_T} > 1$ GeV are added to the cluster. The adding of nearby towers continues until either there are no more towers with more than the minimum amount of energy, or a maximum cluster size is reached. An energy weighted centroid is calculated for the cluster. A jet's energy is defined to be the sum of energy within a cone of radius $\Delta R = 0.4$ about the centroid. This "raw" jet energy has not been corrected for various detector effects. Additional jet corrections are described in detail in Section 5.1.1.

Electron identification begins with a calorimeter based clustering algorithm similar to the one described for jets. An electron cluster also starts with a seed tower of at least 3 GeV of electromagnetic transverse energy (E_T^{EM}). Adjacent towers with $E_T^{EM} > 0.1$ GeV are added until a maximum cluster size is reached. An electron candidate is required to have $E_T^{EM} > 5$ GeV and a ratio of hadronic to electromagnetic energy in the cluster less than 0.125.

A muon candidate consists of a CTC track which is matched to a track segment in a muon detector. Hits in the CMU, CMP and CMX are first fit to form track segments called stubs. The muon stubs are then extrapolated back to tracks in the CTC. Each muon stub is linked with the nearest CTC track in $r - \phi$ to form a muon candidate.

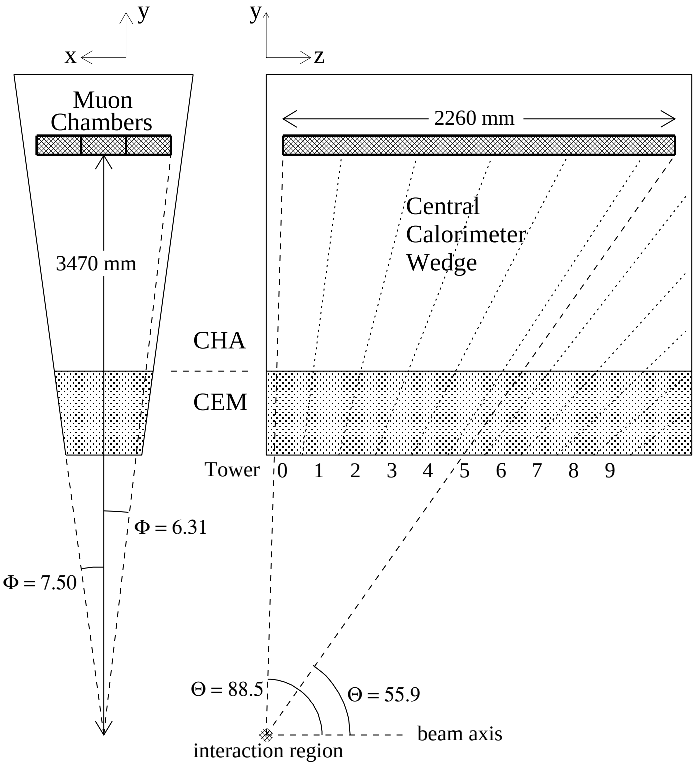

Figure 2.6: Geometry of a central calorimeter wedge and its towers.

Chapter 3

The Event Samples

Event samples from both data and Monte Carlo generators are used in this analysis. Monte Carlo generators are computer programs which use random numbers, hence Monte Carlo, to simulate data events of the type one is interested in. Descriptions of these samples are given here for simplicity in the reading of later chapters. Throughout the chapter, selection requirements made on the samples will be referred to as "cuts".

3.1 Data

This analysis focuses on the lepton+jets decay mode for measuring the top mass. This decay channel is characterized by events which have a high energy lepton and a large amount of missing transverse energy ($\not{E}_{\mathrm{T}}$) from the leptonic decay of one W, and 4 jets from the hadronic decay of the other W and the two b quarks. The search for top events starts by first requiring the event to have a high E_{T} electron or a high P_{T} muon as described in Sections 3.1.1 and 3.1.2. Tighter selection criteria, described in section 3.1.3, are imposed to select only the electron or muon events which come from a W boson decay. Section 3.1.4 describes the sample of events, a subset of the W sample, which are used to measure the mass of the top quark.

3.1.1 Inclusive Electron Sample

A central electromagnetic (CEM) cluster is classified as an electron candidate at the Level 1 trigger if it has $\mathrm{E_T} > 8$ GeV. At Level 2, a CEM cluster with $\mathrm{E_T} > 16$ GeV must match to a CFT track with $\mathrm{P_T} > 12$ GeV. This requirement is only $\sim$ 90% efficient for electrons (with $\mathrm{E_T} > 20$ GeV) so an additional Level 2 trigger was added. The second trigger requires a CEM cluster with $\mathrm{E_T} > 16$ GeV and at least 20 GeV of $\not{E}_\mathrm{T}$. Additional cuts are applied at Level 3 which are looser versions of the final selection cuts described below.

Table 3.1 lists the cuts that are applied to the electron candidates passing the Level 3 trigger. These electron quality cuts are designed to eliminate non-electrons, electrons in jets and electrons coming from photon conversions. First, the $\mathrm{E_T}$ requirement for the CEM cluster is raised to $\mathrm{E_T} > 20$ GeV. Next, to insure that a CTC track associated with an electromagnetic cluster in the calorimeter came from the same particle, the ratio of the electromagnetic calorimeter energy (E) to the momentum (P) of the track must be less than 1.8. Particle showers from electrons are mostly contained in the electromagnetic (EM) calorimeter while hadronic showers tend to deposit energy in both the electromagnetic and hadronic (HAD) sections. The E_{had}/E_{em} cut requires that most of the calorimeter energy associated with the electron is electromagnetic instead of hadronic. Additionally, the energy profile of adjacent calorimeter towers is required to be similar to the profile measured using test beam electrons. The L_{shr} variable is an indicator of how well the electron cluster matches this profile prediction and is defined as:

$$L_{shr} = 0.14 \sum_i \frac{E_i^{obs} - E_i^{pred}}{\sqrt{(0.14\sqrt{E})^2 + \sigma_{pred}^2}}$$

where E_i^{obs} is the observed energy in tower i, E_i^{pred} is the predicted energy in tower i, σ_{pred}^2 is the uncertainty on the predicted value, $0.14\sqrt{E}$ is the uncertainty on the measured energy and the sum is over all adjacent towers. The electron track must also be well matched to hits in the Central Electromagnetic Shower (CES) chamber. The quantities Δx and Δz denote the distance in the $r - \phi$ and z directions, respectively, between the extrapolated CTC track position and the electron shower position measured in the CES. In addition a χ^2 test is used to compare the profile of the electron shower shape (χ^2_{strip}) in the CES with the shape measured from testbeam electrons. To insure that the electron track came from the primary vertex the z position of the electron track origin is required to be within 5 cm of a well measured VTX event vertex ($|Z_{electron} - Z_{vertex}|$). The event vertex itself is required to be close to the center of the detector by the $|Z_{vertex}|$ cut. Finally, fiducial cuts are applied to remove electron clusters which are near detector boundaries.

Efficiencies for these cuts are measured using electrons from Z boson decay. Electrons in the decay $Z \rightarrow e^+e^-$ are expected to have characteristics similar to electrons from W decay. To identify $Z \rightarrow e^+e^-$ events tight quality cuts are used to find a good electron (the primary electron) and looser cuts to find the second electron (the secondary electron). If the combined mass of the primary and secondary electrons is between 75 and 105 GeV the event is assumed to come from a Z decay. To be unbiased, the primary electron is required to pass tight cuts and satisfy the trigger, while the characteristics of the secondary electron are used to measure the electron finding efficiency. Figure 3.1 shows distributions for several

$E_T > 20$ GeV
$E/P < 1.8$
$E_{had}/E_{em} < 0.05$
$L_{shr} < 0.2$
Track Strip/Wire Matching:
$\Delta x < 1.5$ cm
$\Delta z < 3.0$ cm
$\chi^2_{strip} < 10$
$\lvert Z_{electron} - Z_{vertex}\rvert < 5$ cm
$\lvert Z_{vertex}\rvert < 60$ cm
Fiducial Requirements

Table 3.1: Inclusive electron sample selection requirements.

of the selection criteria variables, already described, for a sample of secondary electrons from Z decay. The combined efficiency of all the cuts in Table 3.1 is $81.9 \pm 0.7(stat)\%$.

The inclusive electron sample does contain real electrons which do not come from W decay. These electrons typically come from photons which interact with material in the detector and convert to electron positron pairs. These electrons are called conversion electrons. Before removal, conversion electrons comprise roughly 30 - 40% of the inclusive electron sample. Since the photon is massless, conversion electrons are identified by searching for an additional oppositely-charged track near the electron track that extrapolates to a common tangent point. The tracks are required to be close in θ and to pass within 0.3 cm of each other in the $r - \phi$ plane. If the P_T of the additional track is too low, the track will not be reconstructed. To remove conversions electrons of this type, electron candidates with fewer than 20% of the expected hits in the VTX are removed. A summary of the conversion removal cuts is listed in Table 3.2. The efficiency of the conversion removal cuts is $90.7 \pm 3.8\%$.

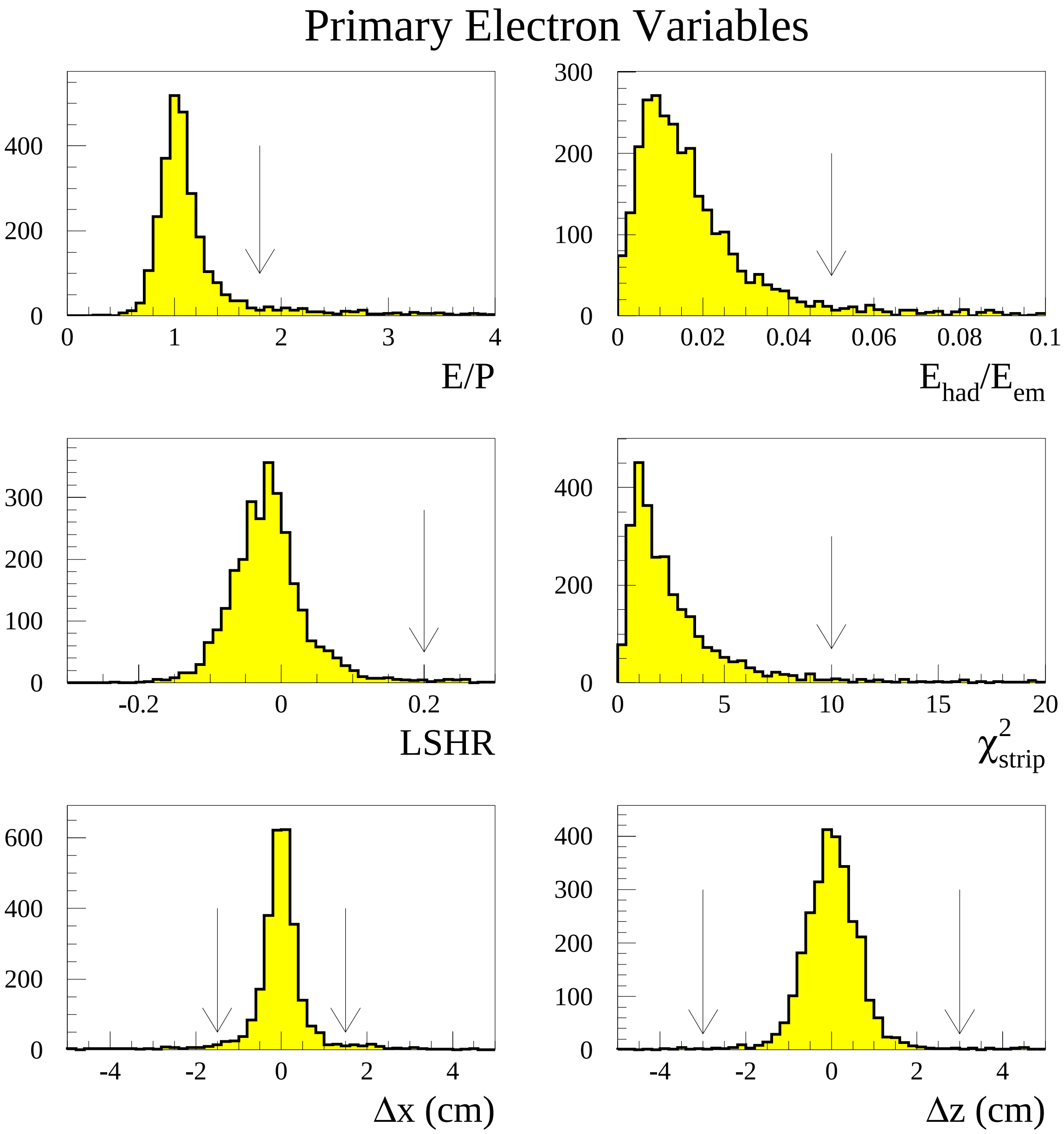

Figure 3.1: Selection requirement variables used in defining the inclusive electron sample, plotted for electrons in a $Z \rightarrow e^+e^-$ sample. The arrows indicate where the cuts are made.

$\lvert\Delta R\phi\rvert < 0.3$ cm *and* $\lvert\Delta cot(\theta)\rvert < 0.06$
OR
$VTX_{occupancy} < 0.2$

Table 3.2: Inclusive electron sample conversion removal selection requirements.

3.1.2 Inclusive Muon Sample

Muon events at CDF are categorized by the detector region through which they pass. Muons reconstructed in both the CMU and CMP are called CMUP muons. If the muon is reconstructed in only one of the muon systems it is called a CMU-only or CMP-only muon. If the muon passes through the CMX, it is called a CMX muon.

Muons are selected for the inclusive muon sample if they pass a Level 2 trigger which requires a CFT track with $P_T > 12$ GeV/c pointing to within 5° of a Level 1 muon stub. Some of the Level 2 muon triggers have very high event rates so only 1 out of every n triggers is kept. This procedure is called prescaling. Prescaling of triggers is done so that event rates which are unacceptably large are kept manageable. The variable n changes as a function of luminosity, as the luminosity decreases n is lowered accordingly. Since some of the muon triggers are prescaled an additional trigger which requires a level 2 calorimeter cluster (jet) with $E_T > 15$ GeV matched to a muon track is also used to retain good efficiency for top events. The CMP-only muons are used for this analysis only if there is at least 35 GeV of $\not\!\!E_T$ in the calorimeter, as well as two jets. The level 2 muon trigger requirements are listed in Table 3.3.

The level 3 muon trigger runs full offline reconstruction of muon stubs and a 2-dimensional version of the offline tracking code. The distance between the extrapolated CTC track and the muon stub (Δx) is required to be less than 10 cm

Triggers	Prescaled
CMU-only Muons	
1) $\not\!\!E_{T} > 35$ GeV and two jets with $E_{T} > 3$ GeV	NO
2) CFT track with $P_{T} > 12$ GeV/c matched to CMU stub	YES
3) CFT track with $P_{T} > 12$ GeV/c matched to CMU stub *and* one jet with $E_{T} > 15$ GeV	NO
CMUP Muons	
1) $\not\!\!E_{T} > 35$ GeV and two jets with $E_{T} > 3$ GeV	NO
2) CFT track with $P_{T} > 12$ GeV/c matched to CMU and CMP stubs	NO
3) CFT track with $P_{T} > 12$ GeV/c matched to CMU and CMP stubs *and* one jet with $E_{T} > 15$ GeV	NO
CMP-only Muons	
1) $\not\!\!E_{T} > 35$ GeV and two jets with $E_{T} > 3$ GeV	NO
CMX Muons	
1) $\not\!\!E_{T} > 35$ GeV and two jets with $E_{T} > 3$ GeV	NO
2) CFT track with $P_{T} > 12$ GeV/c matched to CMX stub	YES
3) CFT track with $P_{T} > 12$ GeV/c matched to CMX stub *and* one jet with $E_{T} > 15$ GeV	YES

Table 3.3: Level 2 trigger requirements for the primary muons.

for CMU-only or CMUP muons, 25 cm for CMX muons and 40 cm for CMP-only muons.

If the muon event passes the level 3 trigger requirements, a final set of quality cuts are applied. Table 3.4 lists the inclusive muon selection criteria. Muons in the CMP and CMX detectors traverse more material than in the CMU and experience greater deflections due to multiple scattering. Therefore, the track-to-stub matching cuts (ΔX) are looser for muons in the CMP and CMX than in the CMU. High energy muons are minimum ionizing particles so the electromagnetic (hadronic) energy in the calorimeter tower associated with the muon is required to contain less than 2 GeV (6 GeV) of energy. Finally the z position of the muon track at its point of closest approach to the beam line must be within 5 cm of a good event vertex in the VTX. The event vertex must be within 60 cm of the center of the detector.

The efficiencies for the muon cuts are measured using Z boson decays of the type $Z \rightarrow \mu^+\mu^-$, in a manner similar to the one that was described for the inclusive electron sample. The efficiency of the combined cuts is $91.4 \pm 1\%$ for CMX muons, $90 \pm 2\%$ for CMU-only muons, $88 \pm 2\%$ for CMP-only muons and $93.6 \pm 0.7\%$ for CMUP muons. Figure 3.2 shows the cut variables for secondary muons from a $Z \rightarrow \mu^+\mu^-$ sample, where the primary muon is required to pass tight cuts and satisfy the trigger.

3.1.3 *W* Sample

The W sample is a subset of the inclusive lepton samples. This sample is made by requiring that the primary lepton be isolated and that the event have a significant amount of $\not\!\!E_{\mathrm{T}}$, indicating the presence of a neutrino.

To insure that the leptons are isolated, a quantity called Iso is defined. For

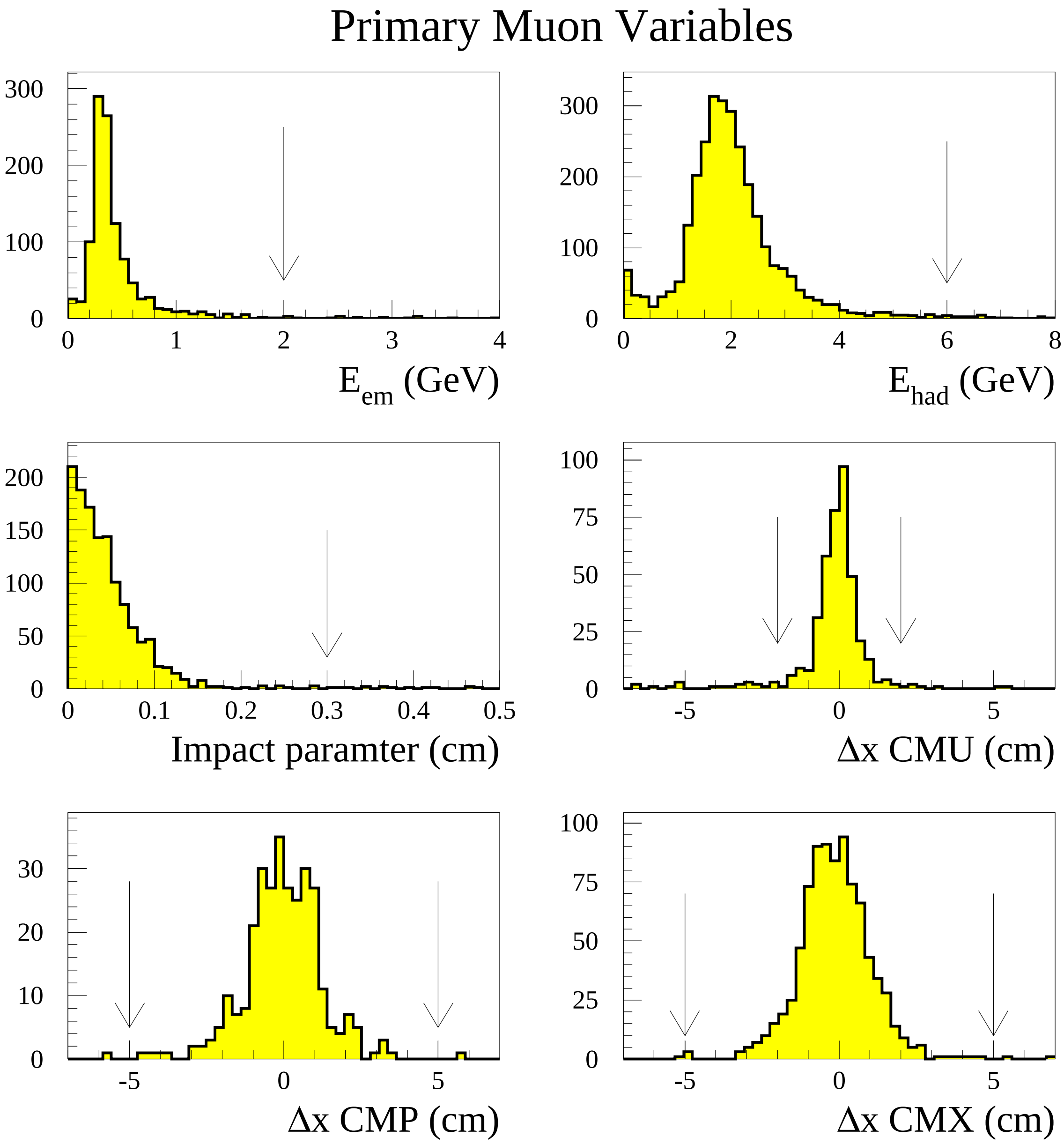

Figure 3.2: Selection requirement variables used in defining the inclusive muon sample, plotted for secondary muons in a $Z \rightarrow \mu^+\mu^-$ sample. The arrows indicate were the cuts are made.

$P_T > 20$ GeV/c
Track-Stub Matching :
$\lvert\Delta X\rvert_{CMU} < 2.0$ cm
OR
$\lvert\Delta X\rvert_{CMP} < 5.0$ cm
OR
$\lvert\Delta X\rvert_{CMX} < 5.0$ cm
E_{em} energy in tower < 2.0 GeV
E_{had} energy in tower < 6.0 GeV
Impact Parameter < 33 mm
$\lvert Z_{muon} - Z_{vertex}\rvert < 5$ cm
$\lvert Z_{vertex}\rvert < 60$ cm

Table 3.4: Inclusive muon sample selection requirements.

electrons, isolation is described by the relation:

$$Iso^{ele} = \frac{E_t^{cone} - E_t^{ele}}{E_t^{ele}}$$

where E_t^{cone} is the calorimeter energy contained in a cone of radius $\Delta R = 0.4$ centered on the electron cluster centroid, and E_t^{ele} is the calorimeter energy of the electron. For muons, isolation is determined by the relation:

$$Iso^{muon} = \frac{E_t^{cone} - E_t^{tower}}{P_t^{muon}}$$

where E_t^{tower} is the amount of energy found in the tower associated with the muon track and P_t^{muon} is the transverse momentum of the muon track. Primary leptons are required to have $Iso < 0.1$.

The neutrino from the leptonic W decay does not interact in the detector so its presence is inferred indirectly when a large imbalance in energy transverse to the beam line, called missing E_T or $\not\!\!E_T$, is observed. The raw $\not\!\!E_T$ of an event is calculated by taking the negative of the vector sum of the transverse energy in calorimeter towers. If the primary lepton is a muon the raw $\not{E}_{\mathrm{T}}$ is corrected by vectorially adding the $\mathrm{P_T}$ of the muon track and subtracting the $\mathrm{E_T}$ in the calorimeter tower associated with the muon. Similar corrections are done for minimum ionizing tracks with $\mathrm{P_T} > 10$ GeV/c, which pass loose matching requirements with a muon stub or extrapolate to regions not covered by the CMU, CMP or CMX detectors. Only events with $\not{E}_{\mathrm{T}} > 20$ GeV are kept in the W sample. This cut is $83 \pm 0.1(stat)\%$ efficient for top events.

Events are also removed from the W sample if the primary lepton is consistent with coming from a Z boson decay or if the event was recorded during a time when there were known detector problems, a “bad run”. For example, bad runs arise when voltage trips occur in any detector component or there is excessive amounts of noise in muon chambers. Events from Z boson decay are identified as described in Section 3.1.1. Table 3.5 lists the cuts imposed on the secondary leptons to identify Z boson decay events. Table 3.6 shows the number of events which survive the W selection criteria.

To check that the W sample contains real W's, the mass of these events should peak at the W mass. The full invariant mass of the W cannot be reconstructed because the longitudinal momentum of the neutrino is unmeasured. However a transverse mass of the W can be calculated using the following relation:

$$M_t = \sqrt{(|P_t^{lep}| + \not{E}_{\mathrm{T}})^2 - (\vec{P_t^{lep}} + \vec{\not{E}_{\mathrm{T}}})^2}$$

where P_t^{lep} is the transverse energy of the electron measured in the calorimeter or the transverse momentum of the muon measured from the muon track. Figure 3.3 shows the transverse mass for electron and muon events from the W sample. The plots exhibit the expected smeared Jacobian peak at roughly the W mass (80

Electron Cuts:
  $E_t > 10$ GeV
  $E_{had}/E_{em} < 0.12$
  $Isolation < 0.2$
  $E/p < 2.0$ (if in CEM)
Muon Cuts:
  $P_t > 10$ GeV/c
 If associated with a stub
  E_{em} energy in tower < 5.0 GeV
  E_{had} energy in tower < 10.0 GeV
  $|\Delta X|_{CMU,CMPorCMX} < 5.0$ cm
  $Isolation < 0.1$
 If no stub
  E_{em} energy in tower < 2.0 GeV
  E_{had} energy in tower < 6.0 GeV
  $|\eta| < 1.1$
  $Isolation < 0.2$

Table 3.5: Loose lepton quality cuts applied to the secondary lepton to remove events consistent with Z boson decays.

	Muons	Electrons
Quality Cuts	87892	121123
Bad Run Removal	84251	115699
Trigger Requirement	79955	111895
$Isolation < 0.1$	51102	76791
$\not\!\!E_{\mathrm{T}} > 20$ GeV	38602	57675

Table 3.6: Events remaining in the W sample after cuts.

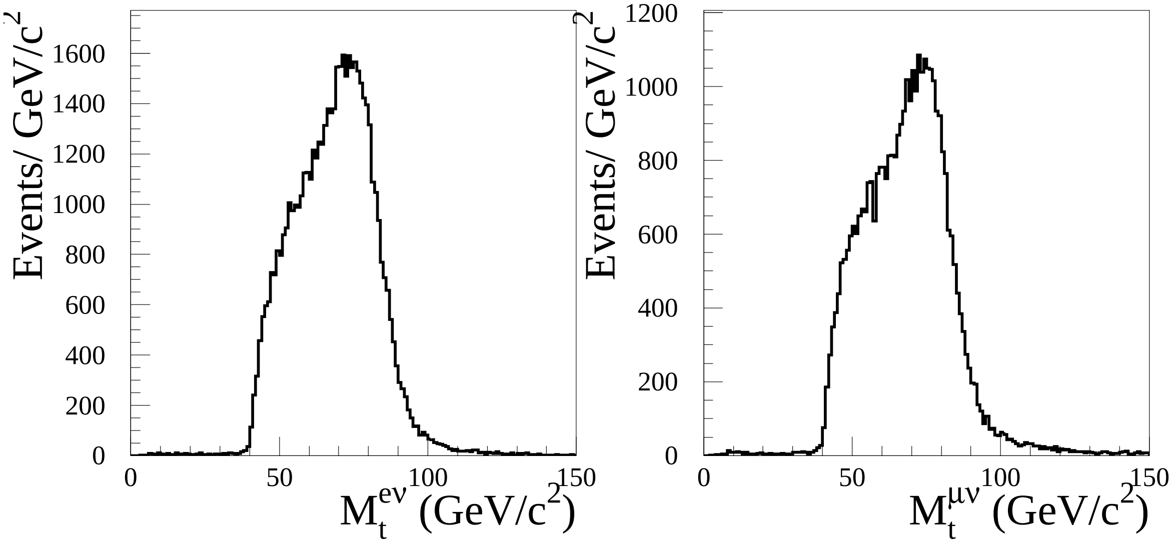

Figure 3.3: Transverse mass of the primary lepton and missing energy for the *W* candidate sample. Events with a primary electron are on the left and events with a primary muon are on the right.

GeV/c^2).

Events passing the dilepton selection criteria are removed from the *W* sample to avoid any overlap of the lepton+jets channel with the dilepton channel. The dilepton analysis begins with the same inclusive lepton samples described here and looks for an additional opposite charged lepton with $E_T > 20$ GeV, $\not{E}_T > 25$ GeV and two jets with $E_T > 20$ GeV. A detailed description of the cuts used in the dilepton analysis can be found in references [2] and [16].

3.1.4 Mass Sample

To fully reconstruct the top mass four jets are needed; two from *b* quarks and two from the hadronic decay of one *W* boson. The number of events in the *W* sample is reduced further by requiring the events to have at least four jets. Three of the jets must have $E_T > 15$ GeV and $|\eta| < 2.0$. By relaxing the requirements on the fourth jet to $E_T > 8$ GeV and $|\eta| < 2.4$ the acceptance for top is increased. There are 163 data events which pass the above requirements and are referred to as the mass sample.

3.2 Monte Carlo

Multi-process shower Monte Carlo event generators are used to simulate the physics of $p\bar{p}$ collisions. Monte Carlo programs help physicists to understand the characteristics of interesting physical processes and to separate them from background events. This analysis makes extensive use of Monte Carlo event samples to measure the top mass and its systematic uncertainty.

Monte Carlo event generators use QCD and Electroweak theory to generate complete $p\bar{p}$ collisions that, in principle, may be treated in the same manner as data. The processes generated by most of these programs are accurate only to leading order and use QCD cascade approximations to simulate higher orders. All of the generators begin by convoluting parton distribution functions with a tree level matrix element for the desired process. Unless otherwise stated all Monte Carlo samples used in this analysis were generated with the MRSD0$'$ [17] parton distribution function which describes CDF's observed W asymmetry data [18].

Each of the event generators outputs a list of four-vectors of stable particles which are then input into a CDF detector simulation package. CDF has two detector simulation packages available, CDFSIM and QFL. CDFSIM models particle showers and interactions in the material of the CDF detector in detail. The QFL simulation uses parameterizations of detector response based on testbeam measurements. In general, CDFSIM is better suited for tracking, whereas QFL models jets more accurately and is considerably faster than CDFSIM.

Since QFL models jets better than CDFSIM and takes less processing time it was used for simulating the detector in this analysis. In QFL, all short-lived particles, except for B hadrons, are decayed according to the branching fractions compiled by the Particle Data Group [19]. The B hadron decay branching fractions and decay kinematics are taken from the measurements of the CLEO collaboration which are implemented in CLEOMC [20].

Three different Monte Carlo generators were used to generate top quark pair events for this analysis; HERWIG, PYTHIA and ISAJET. VECBOS was used to generate W+multijet background events. Each of these Monte Carlo generators is described here briefly with references to more detailed information.

3.2.1 Top Samples

Of the three Monte Carlo generators used to simulate top events, HERWIG is used almost exclusively since it has been shown to reproduce the observed properties of multijet events in CDF data well [21]. PYTHIA is used mainly as a cross-check of the HERWIG results. PYTHIA and HERWIG use similar techniques for generating events and therefore, have similar results. Results from ISAJET provide an additional cross-check with HERWIG. However, ISAJET does not reproduce kinematic distributions of top events (in particular the distribution of the number of jets per event, N_{jet}) as well as HERWIG or PYTHIA.

Both HERWIG and PYTHIA are based on leading-order QCD matrix elements for the hard-scattering processes. HERWIG is a multi-process coherent, parton shower Monte Carlo with cluster hadronization and an underlying event model based on data. PYTHIA is a multi-process Monte Carlo which uses JETSET [25] to provide coherent final state showers, string hadronization and decays. PYTHIA's underlying event model is based upon multiple parton scattering. Jet production in both HERWIG and PYTHIA takes into account color correlations between initial and final state partons. ISAJET is a parton shower Monte Carlo program based on the leading-order QCD matrix elements for the hard-scattering sub-process, incoherent gluon emission, and independent fragmentation of the outgoing partons. This analysis uses HERWIG version 5.6 [22], PYTHIA version 5.7 [23] and ISAJET version 7.06 [24].

3.2.2 Background Samples

The VECBOS [26] Monte Carlo program is used to model W+multijet backgrounds to the top signal. VECBOS is a parton-level Monte Carlo program based on the tree-level matrix element calculations. It produces partons from a hard-scattering process which are subsequently evolved using a separate program derived from the parton shower model contained in Herwig (HERPRT). HERPRT turns the Vecbos output into a list of stable particles which are passed to the QFL detector simulation. VECBOS reproduces the observed kinematics and rates of W+multijet events in data well [27].

Chapter 4

Identifying the Top Quark

Before measuring the top mass a sample of events, which is enriched in top and depleted in background events, is needed. The number of background events in the lepton+jets channel can be greatly reduced by requiring the presence of jets which come from b quark decays. This section briefly explains how CDF tags b quarks and how the expected number of background events was calculated. More detailed explanations can be found in references [2] [28] [29] [30].

The dominant background in the lepton+jets channel is W+multijet production, an example of one such Feynman diagram is shown in Figure 4.1. This background has the same signature as $t\bar{t}$ production except for two important differences; 1) Top events always contain two b quarks, whereas QCD W+multijet events usually do not. 2) The jets in a QCD W+multijet event tend to be less energetic than jets from top decay.

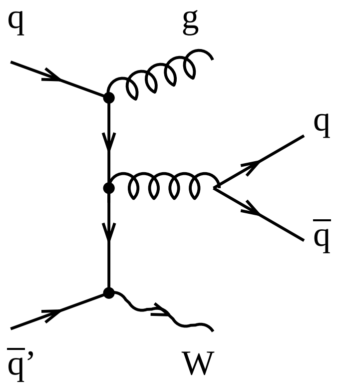

Figure 4.1: The Feynman diagram for W+multijet production which is one of the backgrounds to the top signal.

4.1 B-tagging

To suppress the W+multijet background in the lepton+jets channel, two b-tagging methods are used. The first method uses the CDF silicon vertex detector (SVX) to locate decay vertices of B hadrons that are separated from the primary vertex as a result of the long b lifetime. The second technique is to search in the event for additional leptons (e or μ) from semileptonic decays of B hadrons.

Silicon Vertex Detector Tag (SVX)

B hadrons have a lifetime of $\sim$1.5 picoseconds and receive large boosts in top decays. Therefore, in $t\bar{t}$ events b quarks will travel an average of 3.4 mm, in the radial direction, before decaying. Tracks from the B hadron decay are measurably displaced from the $p\bar{p}$ interaction point, called the primary vertex. See Figure 4.2. The SVX detector can be used to identify tracks from a vertex which is displaced in the transverse direction from the primary vertex. The ability to identify such displaced tracks depends on the resolution for determining both the trajectory of

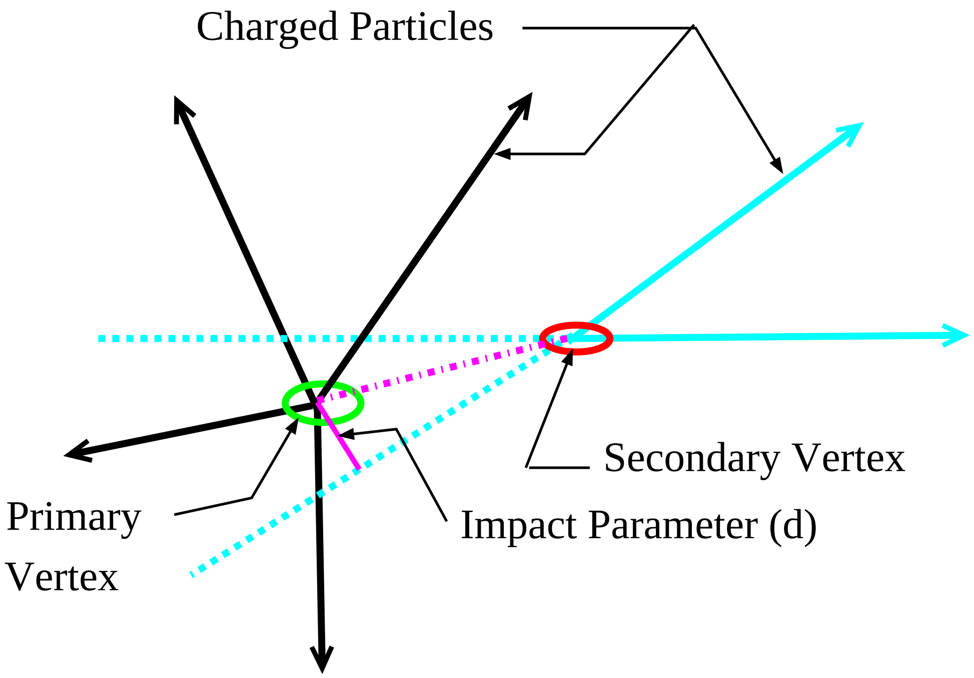

Figure 4.2: Schematic of a displaced vertex in the Silicon Vertex Detector.

each track and the position of the primary vertex, from which most tracks emanate.

The primary vertex is found for each event by a weighted fit of the SVX tracks and the VTX z event vertex position, with appropriate corrections for detector offset and slope. An iterative search removes tracks from the fit, which have large impact parameters. The impact parameter, d, is the distance of closest approach of a track to the primary vertex in the $r-\phi$ plane, see Figure 4.2. The uncertainty in the fitted primary vertex coordinates, transverse to the beam direction, ranges from 6 to 26 μm depending on the number of tracks and the event topology.

Due to the high luminosity conditions at the Tevatron a large number of events in the W sample contain multiple primary interactions separated along the beam axis. In these events, the event vertex is chosen to be the one with the greatest total transverse momentum of associated tracks. All tracks used in the vertex fit and subsequent analysis are required to extrapolate to within 5 cm of this vertex along the beam direction. The resolution on the extrapolation to the z position for CTC tracks above 2 GeV/c is approximately 6 mm.

The SVX tagging algorithm searches for displaced vertices with 3 or more tracks pointing to them, using loose track requirements. If this fails, the track quality requirements are tightened and a search for two-track vertices is performed. If the size of the impact parameter, d, for a track is large compared to its estimated uncertainty, the track is identified as a displaced track. Figure 4.2 shows a schematic drawing of a displaced vertex from a b quark decay. These tracks are used as input to the SVX tagger. The tagger is applied to sets of SVX tracks which are associated with jets that have calorimeter $E_T \geq 15$ GeV and $|\eta| < 2.0$. A track is associated with a jet if the opening angle between the track direction and the jet direction is less than 35°. The distance in the transverse plane from the secondary vertex to the primary vertex is called L_{xy}. L_{xy} is positive if the vertex is on the same side of the primary vertex as the jet, and negative if it is on the opposite side. Jets with significantly displaced secondary vertices with positive L_{xy} are considered tagged. The SVX can resolve displaced vertices to roughly 130 μm. The SVX b-tagger is described in detail in references [28] [29] [2].

For a top mass of 175 GeV/c^2, 67% of $t\bar{t}$ events have at least one b jet in the SVX fiducial acceptance. The efficiency for tagging a b quark is measured in the inclusive electron and muon samples which are enriched in b decays. The ratio of the measured efficiency to the prediction of a detailed simulation is 0.72±0.15 for the vertex detector used in the 1992-93 run, and 0.87±0.07 for the 1994-95 vertex detector. The data/simulation ratio differs from 1.0 as a result of higher tracking efficiency in the simulation. We measure the efficiency for tagging a b quark in a $t\bar{t}$ event using Monte Carlo events, and correct the efficiency found there by the data/simulation scale factor measured in inclusive electron events. The efficiency for tagging at least one b quark in a $t\bar{t}$ event with ≥ 3 jets is found to be (39 ±

3)%.

Soft Lepton Tag (SLT)

An alternate way to tag b quarks is to search for leptons produced in decays of the b quark through $b \to e\nu_l X$ or through the cascade decay $b \to c \to e\nu_l X$. These additional leptons in top events typically have a momentum of a few GeV/c^2 and are contained in the b jet. This method is called the soft lepton tag (SLT) because the leptons from a b decay are produced with momenta lower than leptons from W decays.

Electrons and muons are found by matching CTC tracks with electromagnetic energy clusters or tracks in the muon chambers. In order to maintain high efficiency for leptons coming directly from b decay and from the daughter c quark, the $\mathrm{P_T}$ threshold is lowered to 2 GeV/c. To search for electrons from b and c decays, each particle track reconstructed in the CTC is extrapolated out to the calorimeter and checked for a match to a CES shower cluster. The matched CES clusters are required to be consistent in size, shape and position with expectations for electron showers. In addition, the energy-clustering algorithm was optimized for the detection of electrons from b decays which are nonisolated, unlike electrons from W decays. To identify muons from b or c decays, track segments reconstructed in the muon chambers are matched to tracks in the CTC. To maintain high efficiency for nonisolated muons, the minimum ionizing requirements used to identify isolated muons, described in section 3.1.2 are not imposed. The soft lepton tag analysis is described in detail in reference [30].

The efficiency of the SLT tagger, as a function of lepton $\mathrm{P_T}$, is measured with photon conversions and $J/\psi \to \mu\mu$ data, and applied to Monte Carlo $t\bar{t}$ events. The probability of finding an additional e or μ from a b quark decay in a $t\bar{t}$ event with ≥ 3 jets is $(18 \pm 2)\%$.

4.2 Backgrounds

Backgrounds to top events in the lepton+jets channel come from W+multijet events which contain real heavy flavor, non-W events, mistags, single top production, diboson production (WW, ZZ), $Z \rightarrow \tau^+\tau^-$, Wc and Drell-Yan. A brief description of the larger backgrounds for the SVX and SLT taggers is given below.

The single most important source of background in the SVX tagged sample is inclusive W production in association with jets containing b or c quarks, for example $p\bar{p} \rightarrow Wg(g \rightarrow b\bar{b})$. Gluon splitting can produce $Wb\bar{b}$ or $Wc\bar{c}$ events, and Wc events can be produced from an initial state s quark, as shown in Figure 4.3. To calculate the background from W+multijet events, the HERWIG Monte Carlo program is used to predict, as a function of the number of jets in the event (jet multiplicity), the fraction of events which are $Wb\bar{b}$, $Wc\bar{c}$ and Wc. These fractions and a tagging efficiency for each type of event are applied to the number of W+jet events seen in the data to give an expected background from these sources for each jet multiplicity.

The second largest background to the SVX tagged sample is from mistags. Mistags are tags in jets which contain no true displaced vertices. To calculate the background from mistags, it is assumed that the distribution of reconstructed transverse decay length, L_{xy}, is symmetric about zero. The negative L_{xy} distribution, those secondary vertices which reconstruct to the opposite side of the primary vertex from the jet direction, comes primarily from reconstruction errors in light quark jets. The negative L_{xy} measured in generic jet data is parameterized as a function of jet E_T, η and the number of SVX tracks in the jet. This parameterization is applied to the W+jet data to predict the number of mistags observed.

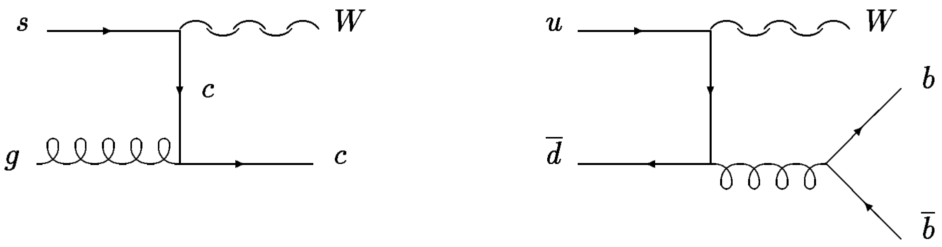

Figure 4.3: Diagrams for heavy flavor production in W+multijet events. The left diagram shows Wc production where a gluon and a strange quark from the proton or antiproton sea produce a W boson with an associated charm quark. The diagram on the right shows $Wb\bar{b}$ production where a final state gluon splits into a $b\bar{b}$ pair. $Wc\bar{c}$ events are produced in an identical manner.

The main background for the soft lepton tag is from "fake" soft lepton tags. Fake tags are defined as particles which are identified as leptons but whose origin is not a heavy flavor decay. This includes non-leptons which pass the lepton selection requirements (such as a pion faking an electron or muon) as well as electrons from conversions, or muons from pions or kaons decaying in flight. The fake and $Wb\bar{b}$ and $Wc\bar{c}$ backgrounds are calculated by measuring the fraction of tags per track in a generic jet sample as a function of the track P_T. These probabilities are applied to tracks in the W+jet events to estimate the background from the above sources.

The remaining backgrounds are calculated in the same manner for both taggers. The background from non-W events, for example direct $b\bar{b}$ production, is calculated from the data by measuring the number of tags as a function of lepton isolation, Iso, and $\not{E}_T$. The tagging rate in the low $\not{E}_T$ and high Iso region, which has essentially no real W events, is used to predict the contamination in the W signal region of high $\not{E}_T$ and low Iso. The single top background is determined by measuring the acceptance of W^* and $W-$gluon production using the PYTHIA and HERWIG Monte Carlo programs, and normalizing to the respective theoretical cross sections. The remaining backgrounds of Wc, Drell-Yan, $Z \to \tau^+\tau^-$ and diboson (WW, ZZ) production, are relatively small for both taggers and are derived from Monte Carlo predictions.

The b-tagging methods and background calculations described here will be used in measuring the top mass, which is described in the next chapter. Jets that are b-tagged must be associated with b quarks when kinematically fitting the top events. The background calculations for the mass sample start from the calculations mentioned above.

Chapter 5

Measuring the Mass of the Top Quark

Measurement of the top quark mass begins by fitting each event in the sample to the hypothesis of $t\bar{t}$ production. This analysis concentrates on the lepton+jets decay channel where one of the W bosons decays hadronically to quark jets and the other decays to a lepton-neutrino pair, as shown below:

$$p\bar{p} \rightarrow t_1 + t_2 + X$$

$$t_1 \rightarrow b_1 + W_1$$

$$t_2 \rightarrow b_2 + W_2$$

$$W_1 \rightarrow l + \nu$$

$$W_2 \rightarrow j_1 + j_2$$

The quantity X represents the system recoiling against the $t\bar{t}$ pair.

5.1 Event Reconstruction

The signature for a lepton+jets top decay is a high energy lepton, missing energy from its neutrino partner, and 4 jets; two from a W and two from the b quarks. In principle, one expects to observe one jet for each quark in the final-state of a $t\bar{t}$ decay. In reality, the number of observed jets may decrease due to detector effects or jet overlap, or increase as a result of multiple interactions or the presence of gluon radiation. In order to determine a top mass for each event, the events are required to have at least four jets so a one-to-one matching of jets to quarks is possible. When an event has more than four jets, the four highest $\mathrm{E_T}$ jets are matched to the quarks. A kinematic fitting program is then used to fully reconstruct each event to the $t\bar{t}$ hypothesis.

5.1.1 Jet energy corrections

Before the jet energies are used in the kinematic fitting program they are corrected for losses in cracks between detector components, absolute energy scale, contributions from the underlying event and multiple interactions, and losses outside the clustering cone. This section gives a brief description of the corrections applied to the jets used for this analysis. The jet energy corrections are divided into the following categories:

- Absolute jet energy scale correction
- Underlying event correction
- Relative jet energy scale correction
- Energy outside of the jet cone correction

The corrected transverse momentum of the jet, $P_T^c(R)$ can be expressed in terms of the above corrections in the following way:

$$P_T^c(R) = (P_T^{raw}(R) \times f_{rel}(R) - UEM(R)) \times f_{abs}(R) - UE(R) + OC(R) \quad (5.1)$$

where:

- $P_T^{raw}(R)$ is the uncorrected transverse momentum of the jet,
- $f_{rel}(R)$ is the relative jet energy correction,
- UEM(R) is the underlying event energy for multiple vertices in the event,
- $f_{abs}(R)$ is the absolute energy scale correction,
- UE(R) is the underlying event energy correction for the primary vertex of the event,
- OC(R) is the energy outside of the chosen jet cone correction.

All of the corrections depend on the chosen cone size, R, of the jet. The corrections are applied in the order shown in equation 5.1 and each correction is described in more detail below.

Absolute jet energy scale correction

The absolute jet energy scale correction corrects for both detector response and fragmentation effects. The CDF detector simulation was tuned to reproduce the particle responses from electron and pion test beam data. Electron and pion test beam data at several energies and isolated pions in min-bias events were used to determine the detector response. The fragmentation effects account for the fact that particles interact in the calorimeter and are experimentally observed as jets.

For measuring the mass of the top quark, one needs to know how to equate the energy of a jet to the energy of the originating particle. The ISAJET fragmentation was tuned so that the detector simulation reproduced a number of experimental distributions.

Underlying event correction

There are actually two corrections in the underlying event correction. One correction takes into account extra energy in the event due to multiple interactions (UEM) while the other takes into account energy in the event when there is only one interaction (UE) or primary vertex. UEM is applied after the relative jet energy correction but before the absolute jet correction. UE is applied after both relative and absolute corrections.

Relative jet energy scale correction

The relative jet energy scale correction corrects for the η response of the detector, relative to the central region of the detector, $|\eta| = 0.2$ to 0.7.

Energy outside of the jet cone correction

The correction imposed for energy which is outside of a given jet cone size has two components. The first component is a correction to take into account differences in the fragmentation modeling of jet energies between cone sizes of 0.4 and 1.0 in data and Monte Carlo. CDF terms this type of correction the soft gluon radiation correction. The second correction takes into account energy which is outside the cone of 1.0. This correction is called the splash-out correction.

Figure 5.1 shows the size of each of the generic jet corrections, described above, as a function of a jet's uncorrected E_T. The corrections are shown for jets with a cone size of 0.4 and assuming $|\eta| = 0.7$. The relative correction shown in the upper left hand corner is flat as a function of the jet E_T but it has an additional dependence based on the $|\eta|$ of the jet. The underlying event correction, shown in the lower left hand corner, is shown assuming that there is only one vertex per event. If there are additional vertices in the event an additional 0.65 GeV is subtracted from the jet E_T for each vertex.

The four leading jets in a $t\bar{t}$ candidate event undergo an additional energy correction which depends on the type of parton they are assigned to in the fit: either a light quark, a hadronically decaying b quark, a b quark that decayed semileptonically into the electron channel, or a b quark which decayed semileptonically into the muon channel. This parton-specific correction was derived from a study of $t\bar{t}$ events generated with the HERWIG Monte Carlo program. The top-specific jet-to-parton corrections are applied to jets as a function of available tagging information. Figure 5.2 shows the fractional change to the corrected jet E_T, after all generic jet corrections have been applied, for (A) jets from the decay of a W boson, (B) jets from b quarks, (C) jets from b quarks semileptonically decaying via a electron, and (D) jets from a semileptonic decay of a b quark to a muon. It can be seen that the largest corrections are for those jets containing a semileptonic decay of a b to a muon. Figure 5.3 shows the size of the average uncertainty in the estimated parton P_T as a function of the jet E_T after applying all of the jet corrections. The curves are for: (A) jets from the decay of W boson, (B) jets from b quarks, (C) jets from the semileptonic decay of the b quark via an electron, and (D) jets from the semileptonic decay of the b quark via a muon. Also indicated is the uncertainty ascribed to any jets observed in addition to the leading four jets. Such jets are corrected solely with the generic jet factors. The parton P_T uncertainties shown are used as an estimate of the resolution during the kinematic

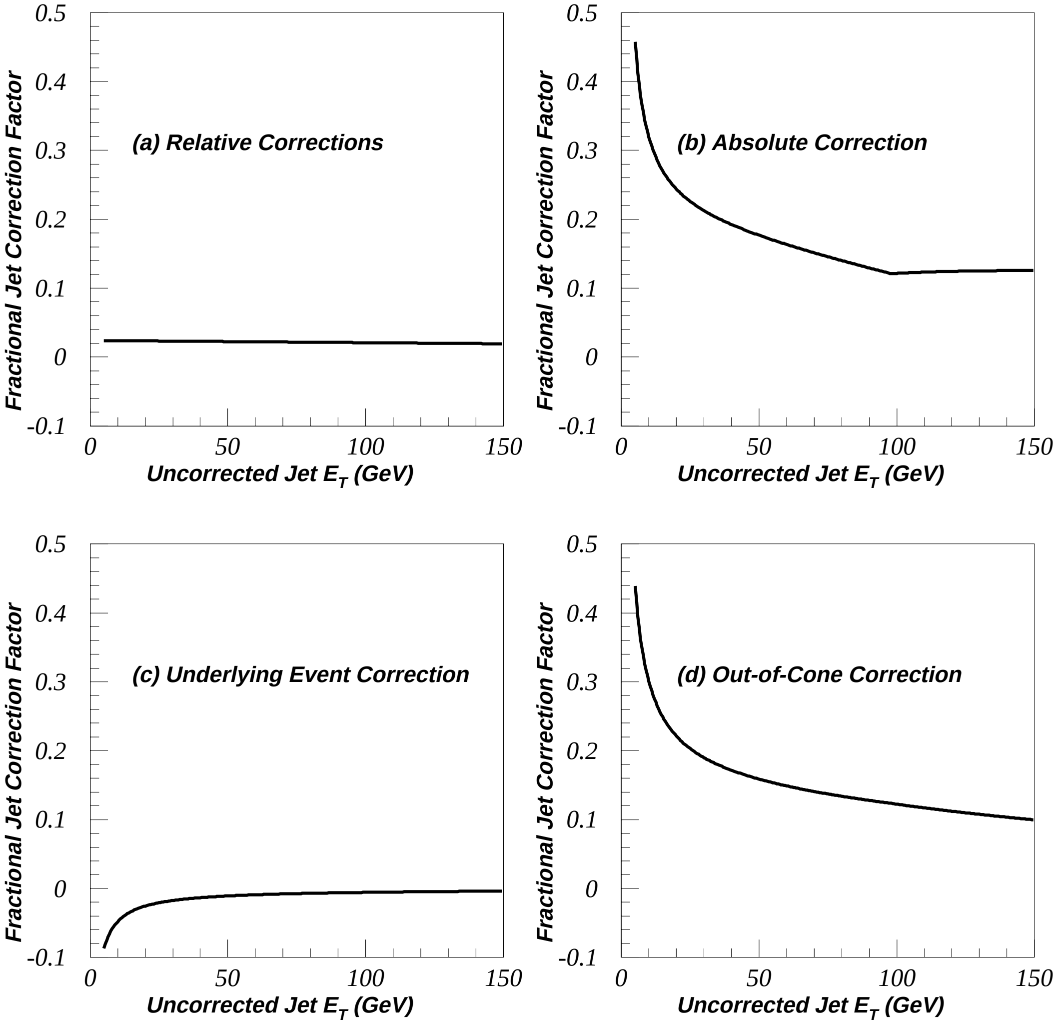

Figure 5.1: The size of the jet corrections as a function a jet's uncorrected E_T for the a) relative correction, b) absolute correction, c) underlying event correction, and d) out-of-cone correction. The corrections are displayed for jets with a cone size of 0.4 and assuming $|\eta| = 0.7$ and only one vertex in the event. The relative corrections shown in (a) contain an additional dependence on the jet $|\eta|$. The underlying event corrections subtract an additional 0.65 GeV for each additional vertex.

fit.

5.1.2 Definition of the fit χ^2

To measure the mass of the top quark, the momenta of the t and $\bar{t}$ are calculated by reconstructing the 4-momenta of the 6 particles in the top decay; ℓ, ν, b, $\bar{b}$, q, and $\bar{q}'$. The 3-momenta of the lepton and the b, $\bar{b}$, q and $\bar{q}'$ quarks are known from the measured energy and angle of the observed lepton and four highest $\mathrm{E_T}$ jets in the event. The masses of the b and $\bar{b}$ are set to 5 GeV/c^2, while those of the light quarks, q and $\bar{q}'$, are set to 0.5 GeV/c^2. (These nominal quark masses are used rather than the measured jet masses because the latter are affected by instrumental effects such as bending of tracks in the magnetic field and secondary interactions.) The W boson mass (M_W) is required to be 80.41 GeV/c^2 [31], with an uncertainty assigned to the W mass in the fit consistent with the W width (σ_W) of 2.12 GeV/c^2 [32]. The top quark width (σ_{top}) is set to 2.5 GeV/c^2 [33]. The neutrino mass is assumed to be zero and its transverse momentum can be obtained from the missing transverse energy, $\vec{\not{E}}_{\mathrm{T}}$. Because of the way that the neutrino transverse momentum is measured, it is strongly correlated with the lepton and jets momenta. To avoid such correlations between the jet momenta and the missing transverse energy, the neutrino 3-momentum is treated as a complete unknown and replaced by constraints on the jets beyond the leading four and on the unclustered energy. The unclustered energy is defined as any energy which is detected in the calorimeter but not collected in a jet or electron cluster. The two transverse momentum components of X are calculated by adding the vector transverse momentum components of the jets, beyond the four leading jets, and the unclustered energy in the event. The invariant mass and z momentum component of X are left as unknowns.

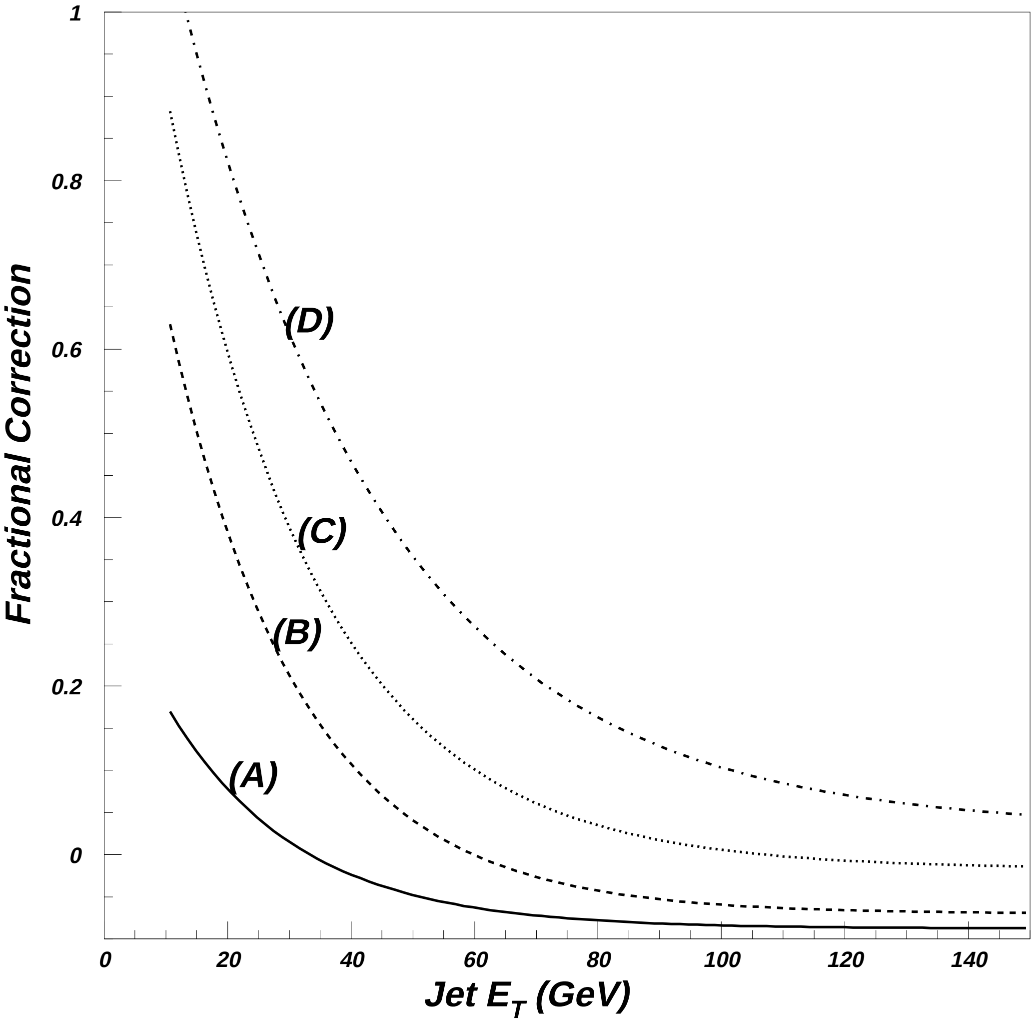

Figure 5.2: The top specific jet-to-parton corrections are applied to jets as a function of available tagging information. The curves show the fractional change to the corrected jet E_T after all generic jet corrections have been applied. The curves are for: (A) jets from the decay of a W boson, (B) jets from b quarks, (C) jets from b quarks semileptonically decaying via a electron, and (D) jets from a semileptonic decay of a b quark to a muon.

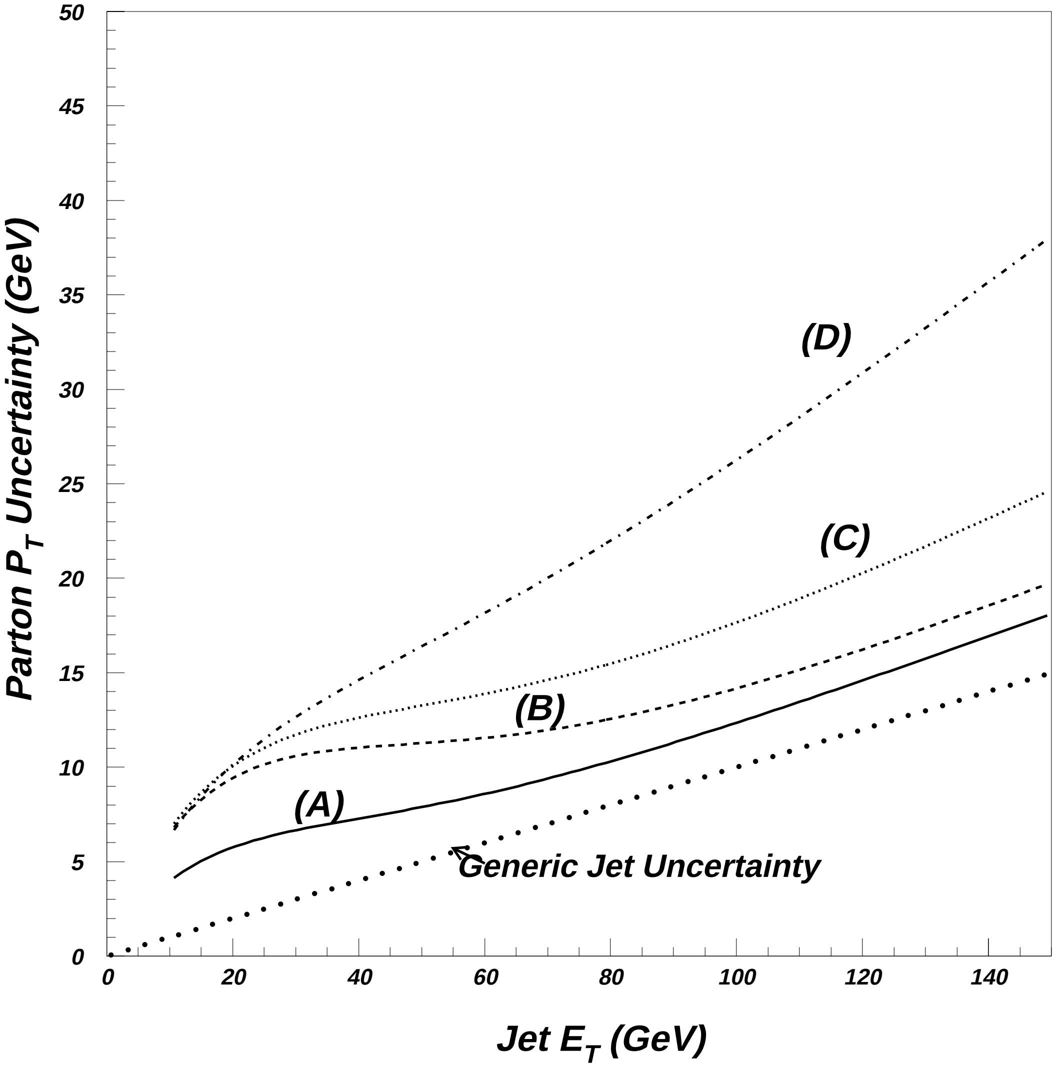

Figure 5.3: The average uncertainty in the estimated parton P_T as a function of the jet E_T after applying all of the jet corrections. The curves are for: (A) jets from the decay of W boson, (B) jets from b quarks, (C) jets from the semileptonic decay of the b quark via an electron, and (D) jets from the semileptonic decay of the b quark via a muon. Also indicated is the uncertainty ascribed to any jets observed in addition to the leading four jets. Such jets are corrected solely with the generic jet factors.

Due to these unknowns, there is insufficient information to fully reconstruct the t and $\bar{t}$ momenta. In order to solve the problem, the following five kinematic constraints are applied: the transverse momentum components of the $t\bar{t}{+}X$ system must be zero, the invariant mass of the lepton-neutrino pair must equal the W boson mass, the invariant mass of the $q\bar{q}$ pair assigned to the W must equal the W boson mass, and the mass of the top quark must equal the mass of the antitop quark. With these additional constraints, the problem is actually overconstrained with two pieces of extra information (2C-fit) and it can now be solved by using the MINUIT [34] package to minimize the following χ^2:

$$\begin{aligned} \chi^2 \;=\; & \sum_{\ell,j} \frac{(\hat{\mathrm{E}}_{\mathrm{T}} - \mathrm{E}_{\mathrm{T}})^2}{\sigma^2(\mathrm{E}_{\mathrm{T}})} + \sum_{i\,=\,x,y} \frac{(\hat{\mathrm{E}}_i^{\mathrm{u}} - \mathrm{E}_i^{\mathrm{u}})^2}{\sigma^2(\mathrm{E}_i^{\mathrm{u}})} + \frac{(M_{\ell\nu} - M_W)^2}{\sigma_W^2} + \\ & \frac{(M_{q\bar{q}'} - M_W)^2}{\sigma_W^2} + \frac{(M_{b\ell\nu} - M_{\mathrm{rec}})^2}{\sigma_{\mathrm{top}}^2} + \frac{(M_{q\bar{q}'\bar{b}} - M_{\mathrm{rec}})^2}{\sigma_{\mathrm{top}}^2} \end{aligned} \qquad (5.2)$$

where the sum in the first term runs over the primary lepton and all jets with observed $\mathrm{E}_{\mathrm{T}} \geq 8$ GeV and $|\eta| \leq 2.4$, and the second sum runs over the transverse components of the unclustered energy. The hatted variables $\hat{\mathrm{E}}_{\mathrm{T}}$ and $\hat{\mathrm{E}}_i^{\mathrm{u}}$ refer to the output of the minimization procedure, whereas $\mathrm{E}_{\mathrm{T}}{}^*$ and $\mathrm{E}_i^{\mathrm{u}}$ represent measured values, corrected for all known detector and physics effects. M_{rec} is the fit parameter giving the reconstructed top mass for the event. Note that the jet directions are not adjusted in the χ^2 minimization. Studies have shown that allowing for such adjustment yields negligible improvement in the mass measurement.

There are twelve ways of assigning the four leading jets to the four partons b, $\bar{b}$, q, and $\bar{q}'$ (the W decay products q and $\bar{q}'$ can be interchanged without affecting the

---

[*] The χ^2 actually uses the jets' P_{T} rather than their E_{T}, where the momentum $\vec{\mathrm{P}}_{\mathrm{T}}$ of a jet is defined as the sum of vectors pointing from the interaction point to the center of each tower belonging to the jet cluster, and with magnitude equal to the energy deposited in the tower. The total energy E of a jet is calculated from its momentum and the nominal mass for the quark.

result of the fit). The kinematical constraints can be used to solve for the neutrino transverse momentum (P_T) and to compute the mass of the lepton-neutrino pair ($M_{l\nu}$) and the mass of the top quark ($M_{bl\nu}$). However, because the longitudinal component of the total energy is unknown, there are two possible solutions for the P_Z of the neutrino. In the absence of any further information, this yields a total of twenty-four different configurations for reconstructing an event according to the $t\bar{t}$ hypothesis. If one or two SVX or SLT-tagged jets are present, they are assigned to b-partons, thereby reducing the total number of configurations to twelve or four, respectively. The ν momentum is left as an unknown in the fit, and it is determined from the kinematical constraints used to solve for the neutrino transverse momentum and to compute $M_{l\nu}$ and $M_{bl\nu}$ at each iteration of the fit. When fitting an event, all allowed configurations are tried, and only the one with the lowest χ^2 is kept. Events for which this lowest χ^2 is larger than 10 are rejected. Figure 5.4 shows the χ^2 distribution for HERWIG top events with M_{top} = 175 GeV/c^2. The efficiency of the $\chi^2 < 10$ cut is 94% for Monte Carlo $t\bar{t}$ events which have at least one SVX or SLT b-tag in the leading four jets and 83% for background events.

5.1.3 Combinatorial issues

The resolution of reconstructed mass distribution obtained by fitting HERWIG $t\bar{t}$ events depends on the intrinsic resolution of the CDF detector and, more importantly, the ability to correctly associate the daughter partons from a $t\bar{t}$ decay with the observed jets. The impact of the ability to correctly associate jets to their originating partons on the reconstructed top mass is studied by dividing the sample of HERWIG (M_{top} = 175 GeV/c^2), where at least one b-tag was required within the leading four jets, into three categories:

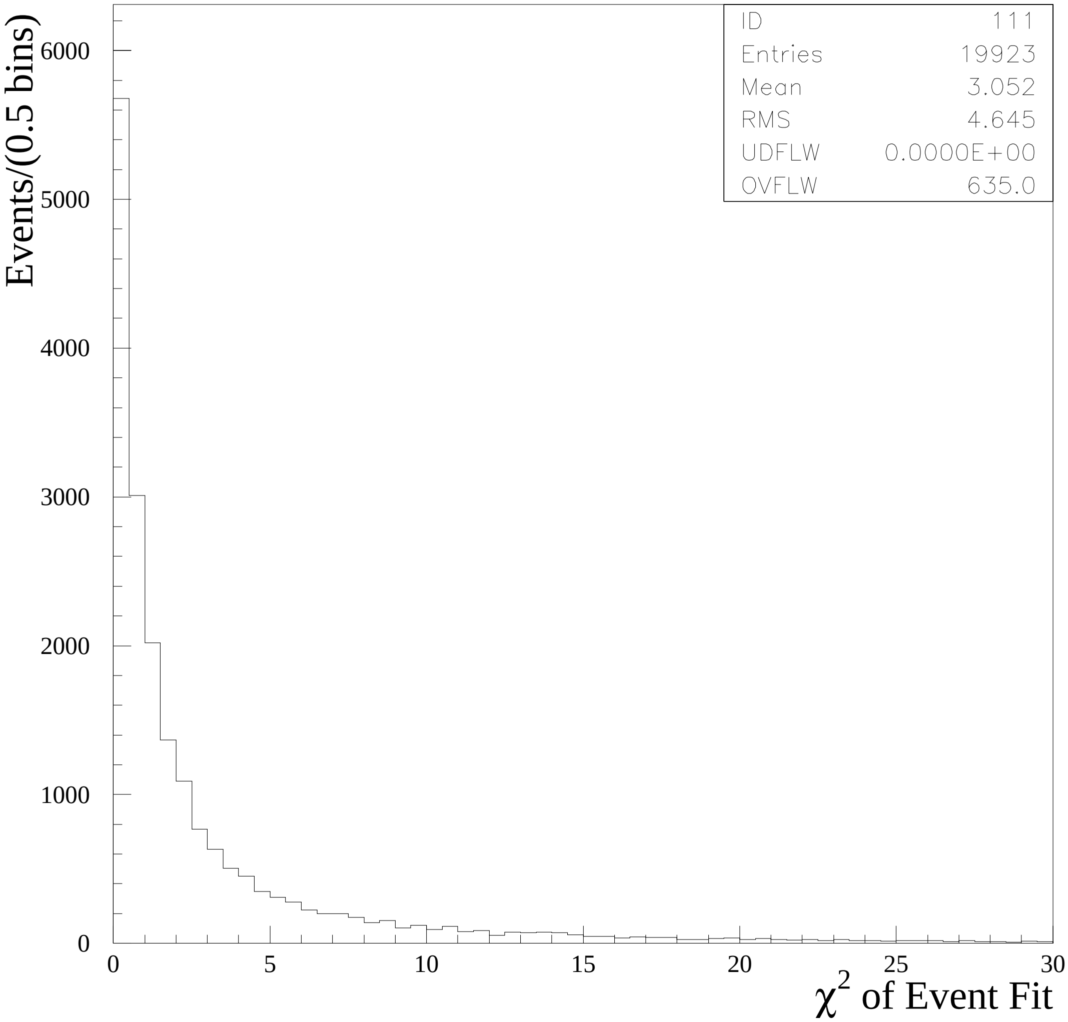

Figure 5.4: The χ^2 distribution for top events from HERWIG with M_{top} = 175 GeV/c^2. A cut is made at $\chi^2 < 10$.

- **Events with Correctly Assigned Jets** - each of the four leading jets are within a cone of $\Delta R < 0.4$ of a parton from the $t\bar{t}$ decay and are correctly associated with the appropriate quark by the lowest χ^2 solution satisfying any imposed tagging requirements. The jet-to-parton match must be unique, meaning that a parton can match to only one jet, two jets cannot be matched to the same parton.

- **Events with Incorrectly Assigned Jets** - each of the four leading jets are within $\Delta R < 0.4$ of a parton from the $t\bar{t}$ decay and the match is unique, but the configuration with the lowest χ^2, consistent with tagging information, is not the correct one.

- **Ill Defined Events** - A good match between the leading jets and partons cannot be defined. Such events are typically characterized as having extra jets produced from either initial or final state radiation.

Figure 5.5 shows the reconstructed mass distribution for HERWIG $t\bar{t}$ ($M_{top} =$ 175 GeV/c^2) events which have at least one tagged jet among the leading four jets. The solid histogram is the shape of the reconstructed top mass distribution for events in which the jets were correctly assigned to the partons. The resolution, or RMS, of this sample is $\sim$ 13 GeV/c^2. The cross-hatched histogram is the shape of the reconstructed top mass distribution for the events in the incorrectly assigned category. The hashed (diagonal lines) histogram is the reconstructed mass distribution for the ill-defined events. The top mass resolution is clearly dominated by the ill-defined events.

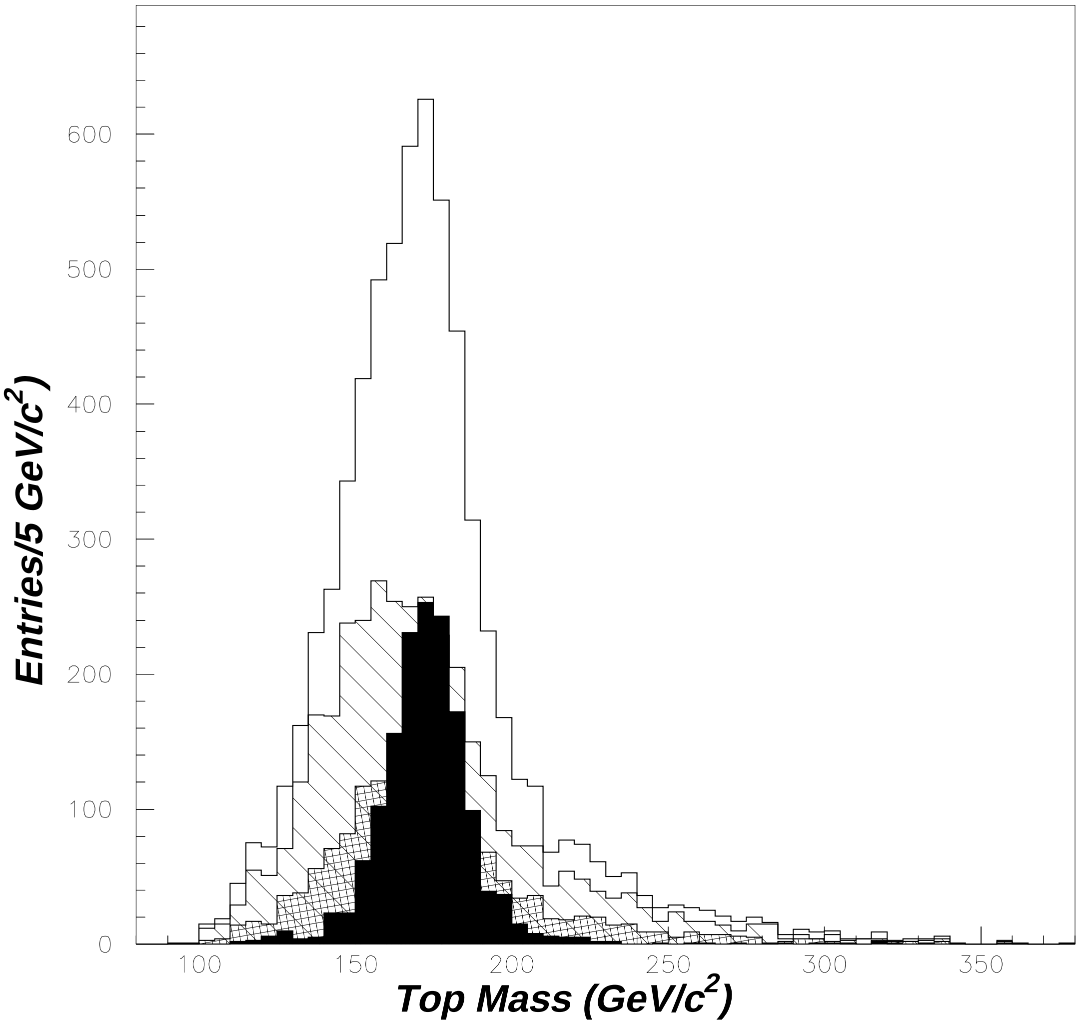

Figure 5.5: The reconstructed mass for $t\bar{t}$ events (M_{top} = 175 GeV/c^2) with at least one tagged leading jet. The solid histogram shows the distribution for those events for which the selected parton-jet configuration was also the correct one. The hashed histogram shows the distribution for events where a correct assignment was ill defined. The cross hatched histogram shows the distributions for which a correct assignment could be defined but was not selected.

5.2 Background Calculation

The calculation of the expected background content of each subsample starts from the background calculation, described in Section 4.2, done for the $t\bar{t}$ cross section measurement [35]. The extrapolation to the mass subsamples takes into account the additional requirement of a fourth jet, the $\chi^2 \leq 10$ cut on event reconstruction, and the requirement that SVX and SLT tags are only counted if they are on one of the leading four jets. The efficiencies of these requirements are determined from Monte Carlo studies. They are used together with background rates and tagging efficiencies from the cross section analysis to predict the total number of events in each mass subsample as a function of the unknown numbers of $t\bar{t}$ ($N_{t\bar{t}}$) and W+jet (N_W) events in the total combined mass sample. For given values of $N_{t\bar{t}}$ and N_W, the expected number of events $N_{pred,j}$ in each subsample j can be predicted by the following equation:

$$N_{pred,j} = a_j \times N_{t\bar{t}} + b_j \times N_W + N_{abs,j}$$

where $N_{abs,j}$ is the number of events from background sources for which an absolute rate can be estimated, and a_j, and b_j are obtained from various known rates and efficiencies. $N_{t\bar{t}}$ and N_W are varied in order to optimize the agreement between observed and predicted subsample sizes. This is done by maximizing a multinomial log-likelihood that constrains the predicted subsample sizes to the observed ones. This procedure generates the expected background contents shown in Table 5.1, and the background likelihood $\mathcal{L}_{backgr}$ used in equation 5.6. Figure 5.6 shows the background likelihood shapes for each of the four subsamples used to measure the top mass.

Approximately 67% of the background in the entire mass sample comes from

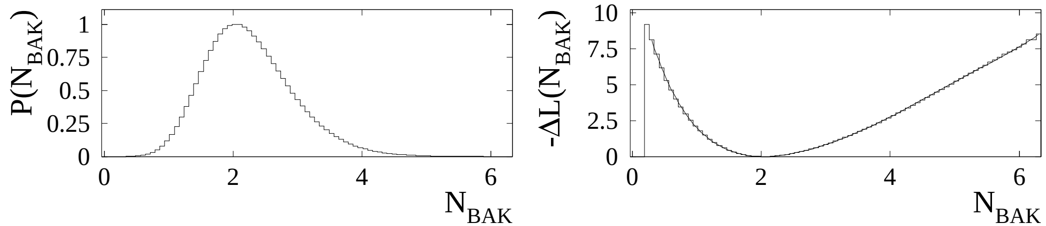

P(N_{BAK}) - SVX Single

L(N_{BAK}) - SVX Single

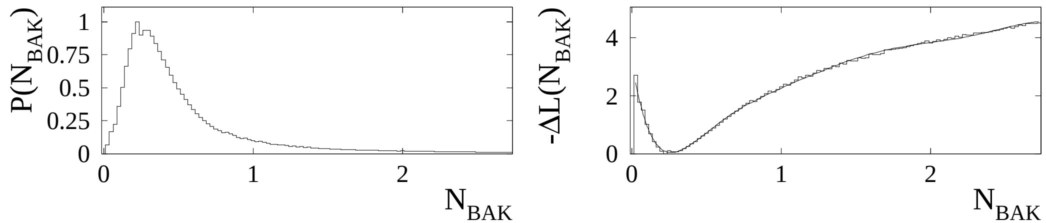

P(N_{BAK}) - SVX Double

L(N_{BAK}) - SVX Double

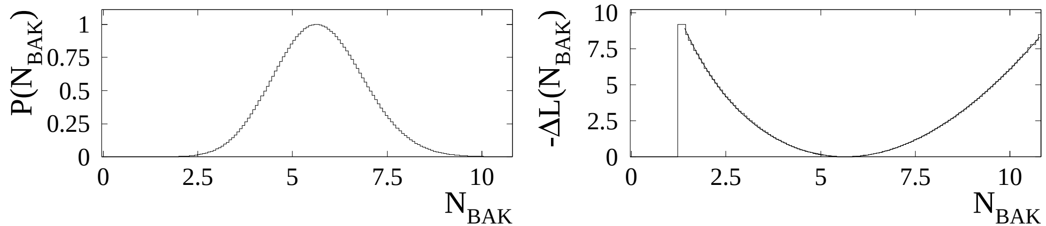

P(N_{BAK}) - SLT

L(N_{BAK}) - SLT

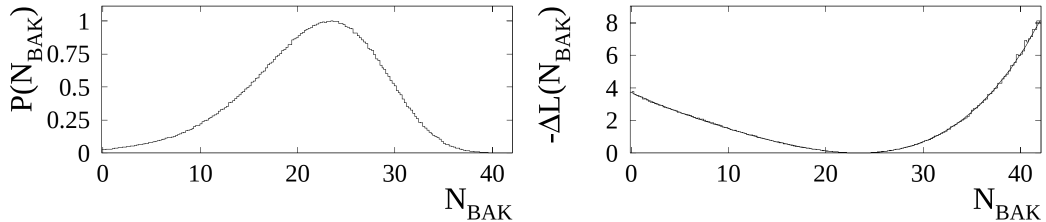

P(N_{BAK}) - NoTag

L(N_{BAK}) - NoTag

Figure 5.6: Probability distribution of the expected background in the four subsamples and their associated negative log-likelihoods, which are used in the constrained likelihood fit.

Subsample	N_{bg}	x_b^{fit}
SVX Double Tag	0.2 ± 0.2	0.05 ± 0.03
SVX Single Tag	2.0 ± 0.7	0.13 ± 0.04
SLT Tag (No SVX)	5.6 ± 1.2	0.40 ± 0.08
No Tag ($E_T > 15$)	23.5 ± 6.5	0.55 ± 0.13

Table 5.1: The expected number of background (N_{bg}) and the background fraction (x_b^{fit}) for the mass event subsamples which are used for the top quark mass measurement.

W+jet events. Another 20% consists of multijet events where a jet was misidentified as a lepton and $b\bar{b}$ events with a b hadron decaying semileptonically. The remaining 13% is made up of Z+jet events where the Z boson decays leptonically, events with a WW, WZ or ZZ diboson, and single-top production. The shape of the mass distribution of W+jet events generated from VECBOS has been compared with mass distributions from W and Z+multijet data events as well as non-W backgrounds [36]. For example, the reconstructed mass distributions from VECBOS and data for three event selections, which are expected to be depleted in $t\bar{t}$ events, have been compared. These selections are slight variations of the mass sample selection. The first selection requires that the primary lepton be an electron with a pseudorapidity in the range of $1.1 \leq |\eta| \leq 2.4$ instead of $|\eta| \leq 1.0$. The second selection requires at least four jets with $E_T \geq 8$ GeV and $|\eta| \leq 2.4$, but no more than two jets with $E_T \geq 15$ GeV and $|\eta| \leq 2.0$. The third selection was obtained by choosing events with a non-isolated primary lepton. In all three cases, a Kolmogorov-Smirnov test applied to the comparison of VECBOS and data yielded a confidence level of at least 35%. Since the shape of the mass distribution for W+jet events from VECBOS agrees well with mass distributions from W and Z+multijet data events, as well as non-W backgrounds, the VECBOS mass distribution is used to determine the shape of the background likelihood function

(f_b).

5.3 Discrete Likelihood Method

In order to extract a top mass measurement from a sample of $t\bar{t}$ candidates, it is necessary to know how the reconstructed mass is distributed for signal and background events. Let $f_s(M_{\rm rec}; M_{\rm top})$ be the probability density to reconstruct a mass $M_{\rm rec}$ from a $t\bar{t}$ event if the true top mass is $M_{\rm top}$, and $f_b(M_{\rm rec})$ is the probability density to reconstruct a mass $M_{\rm rec}$ from a background event. The probability density function for $t\bar{t}$ events (f_s) is estimated for discreet sets of $M_{\rm top}$ values by smoothing histograms of $M_{\rm rec}$ for HERWIG $t\bar{t}$ events. Samples of HERWIG $t\bar{t}$ events were generated for various values of M_{top} ranging from 120 GeV/c^2 to 220 GeV/c^2 in steps of 5 GeV/c^2. The reconstructed mass histogram for each value of M_{top} is smoothed to remove large statistical fluctuations from bin to bin, particularly in the tail of the distribution. Such histograms are referred to as templates. A background template is similarly obtained by smoothing a histogram of $M_{\rm rec}$ for VECBOS [26] events. A maximum-likelihood technique is then used to fit the $M_{\rm rec}$ distribution of the data to a sum of background and signal templates. The likelihood is maximized with respect to N_b and N_s for each M_{top} value for which a Monte Carlo signal template exists. The likelihood is expressed in the following way:

$$\mathcal{L} = \mathcal{L}_{shape} \times \mathcal{L}_{count} \times \mathcal{L}_{backgr} \tag{5.3}$$

where:

$$\begin{aligned} \mathcal{L}_{shape} &= \prod_{i=1}^{N} \frac{N_s\, f_s(M_i, M_{\rm top}) + N_b\, f_b(M_i)}{N_s + N_b} \\ \mathcal{L}_{count} &= \frac{e^{-(N_s+N_b)}\,(N_s + N_b)^N}{N!} \end{aligned}$$

$$\mathcal{L}_{backgr} = \frac{1}{\sqrt{2\pi}\,\sigma_b} e^{\frac{-(N_b-n_b)^2}{2\sigma_b^2}},$$

where N_b and N_s represent the number of background and signal events, respectively, N is the number of observed events, n_b is the calculated number of background events, and σ_b is the calculated background uncertainty. The variable f_s is the normalized top Monte Carlo mass distribution and f_b is the normalized W+jet Monte Carlo mass distribution. The variable M_i is the top mass that gives the minimum χ^2 for the fit of the ith event.

To calculate the top mass and its uncertainty, the negative log-likelihood values from all the fits are plotted as a function of $M_{\rm top}$. The top mass corresponds to the minimum of the negative log-likelihood and its statistical uncertainty is defined to be the spread in the top mass value when changing the log-likelihood value by half a unit with respect to its minimum. This technique for the fitting the mass has been documented extensively in various publications [2] [3] [4].

5.4 Optimization Technique

The statistical uncertainty on the top quark mass measurement is expected to decrease if the number of observed events increases, or the purity of the event sample improves, or the top mass resolution improves. Run I data taking for the colliding experiments at the Tevatron was completed last year and new data will not be available until 1999. So to improve the statistical precision of the top mass measurement requires improving the purity and the resolution of the mass sample. These characteristics vary significantly depending on the b-tagging requirements which are imposed on the mass sample. Therefore, to make closer to optimal use of all the available information, the $W+\geq 4$-jet mass sample is partitioned into non-overlapping subsamples based on b-tagging information.

The simplest way to divide the mass sample is into two subsamples; one with events that do not contain a b-tag and one with events that have a b-tag within the four leading jets. Throughout the rest of this thesis, the sample of events without b-tags will be called the "No Tag" subsample and the sample of events with at least one b-tag will be called the "SVX or SLT Tagged" subsample. The sample of b-tagged events can be divided further based on the type of tag, either SVX or SLT. Since the SVX tagger is better at rejecting background, the SLT tagging information is ignored for events that have both an SVX and an SLT tag. Events which have SLT tags and no SVX tags are placed in the "SLT Tagged" subsample. The SVX tagged events themselves can be divided again into events which have only one SVX tag, "SVX Single Tagged" subsample, and events which have two SVX tags, "SVX Double Tagged" subsample.

To help determine which of the above subsamples should be used to measure the top mass, the purity and resolution of these subsamples is examined. A way to measure the purity of an event sample is by calculating the ratio of the number of signal to background events expected for that sample. Table 5.2 shows the number of data events observed, the calculated number of background, and the signal to background ratio for various mass subsamples. In addition to separating the events by b-tag type, the purity of the samples can be increased by changing the kinematic cuts on the mass sample to reduce the number of background events. An obvious thing to try is to tighten the $\mathrm{E_T}$ and η cuts on the fourth jet to match the cuts of the three highest $\mathrm{E_T}$ jets; $\mathrm{E_T} > 15\ GeV$ and $\eta < 2.0$. The efficiency of the tighter kinematic requirements on the fourth jet is 31% for background and 68% for top. The last line of Table 5.2, No Tag ($\mathrm{E_T} > 15$), gives the signal to background ratio for the No Tag subsample but with the tighter kinematic cuts.

Subsample	$N_{observed}$	N_{back}	Signal/Back
SVX or SLT Tag	34	7.8 ± 2.2	3.3/1
SVX Single Tag	15	2.0 ± 0.6	6.5/1
SVX Double Tag	5	0.2 ± 0.2	22.8/1
SLT Tag (No SVX)	14	5.6 ± 1.2	1.5/1
No Tag	119	91.6 ± 10	0.3/1
No Tag ($E_T > 15$)	42	23.5 ± 6.4	0.8/1

Table 5.2: The number of observed mass events ($N_{observed}$) in 110 pb^{-1} of data and the expected number of background events (N_{back}) for various subsamples. The last column shows the signal to background ratio (or purity) of each of the subsamples.

Subsample	Width (GeV/c^2)	$f^{correct}$
SVX or SLT Tag	29.8	0.400 ± 0.011
SVX Double Tag	24.6	0.603 ± 0.025
SVX Single Tag	30.9	0.371 ± 0.014
SLT Tag (No SVX)	30.7	0.306 ± 0.022
No Tag ($E_T > 15$)	33.9	0.250 ± 0.013

Table 5.3: The width of the reconstructed top mass distribution for various subsamples from HERWIG ($M_{top} = 175$ GeV/c^2) Monte Carlo. The fraction of events ($f^{correct}$) in which the observed jets correctly matched (see Section 5.1.3) to the top decay partons is also shown.

The resolution on the top mass is determined by the width of the reconstructed top mass distribution, which is fit to a gaussian and the RMS is taken as the width. Table 5.3 lists the widths of the mass distributions for various subsamples using HERWIG $t\bar{t}$ generated events. This table also includes the fraction of events in which the observed jets match correctly to the top decay partons, as defined in Section 5.1.3.

To determine which mass subsamples give the smallest statistical uncertainty, Monte Carlo simulations of the data, or "pseudo-experiments", are run for each of the subsamples. Each pseudo-experiment consists of the same number of total events as the data. The calculated number of background events (shown in Table 5.2) are chosen from the VECBOS template. The $t\bar{t}$ events are chosen from the HERWIG (M_{top} = 175 GeV/c^2) template. The pseudo-experiment is then treated exactly like the data and fit as described in Sections 5.1 and 5.3. Each pseudo-experiment returns a top mass and statistical uncertainty. Five hundred pseudo-experiments are done for each subsample, producing distributions of 500 top masses and 500 statistical uncertainties. The median of the distribution of statistical uncertainties is used as the figure of merit for deciding which subsample should be used to measure the top mass.

Table 5.2 shows that the signal to background ratio (purity) of the SVX Tagged subsamples is much higher than any of the other subsamples. Based on this fact, it is reasonable to consider using only the SVX Tagged subsamples to measure the top mass. However, from Table 5.4, one sees that the statistical uncertainty on the top mass is smaller when using the SVX or SLT Tagged subsample than using the SVX Tagged subsamples alone. It is indeed true that the amount of background is significantly reduced by using the SVX Tagged samples only but the number of events in this sample is small enough to cause the statistical uncertainty to increase instead of decrease. Tables 5.2 and 5.4 show that the SVX Double Tagged subsample gives the best purity and resolution of any of the subsamples but it is statistically limited until more data is collected.

Table 5.2 also shows that the signal to background ratio increases for No Tagged subsample when the kinematic constraints on the jets are tightened. For the tagged subsamples the tighter kinematic cuts do increase the purity of these samples but they reduce the number of events per subsample enough that the statistical uncertainty increases. Table 5.4 shows that the tighter kinematic cuts decrease the statistical uncertainty for the No Tagged subsample. For the remainder of this

Subsample	Median Mass GeV/c^2	Stat. Uncertainty GeV/c^2
SVX or SLT Tag	175.1	6.4
SVX Single Tag	175.7	8.7
SVX Double Tag	175.4	9.7
SLT Tag (No SVX)	175.3	12.1
No Tag	173.8	12.9
No Tag ($E_t > 15$)	174.3	11.6

Table 5.4: The median mass and median statistical uncertainty from 500 pseudo-experiments for various subsamples.

thesis the tighter kinematic cuts will only be applied to the No Tagged subsample.

The amount of information used to measure the top mass can be be increased by using more than one of the mass subsamples. Since the subsamples were constructed to be exclusive (non-overlapping), their corresponding likelihoods (as defined in Section 5.3) can be treated as statistically uncorrelated and multiplied together to obtain one total likelihood. A set of 500 pseudo-experiments are generated for each subsample and the likelihood values from each experiment are multiplied together. Each of the 500 combined likelihoods is fit to obtain a distribution of top masses and statistical uncertainties. The median mass and median statistical uncertainty is compared for different combinations of uncorrelated subsamples to determine which combination is the best. Table 5.5 shows the masses and statistical uncertainties for several different combinations of uncorrelated subsamples.

The combination which gives the smallest expected statistical uncertainty uses the following four subsamples:

- SVX Single Tagged
- SVX Double Tagged

Subsample	Median Mass GeV/c^2	Stat. Uncertainty GeV/c^2
(SVX or SLT) + No Tag ($E_t > 15$)	176.1	5.9
SVX + SLT (No SVX) + No Tag ($E_t > 15$)	176.1	5.8
SVX Single + SVX Double + SLT (No SVX) + No Tag ($E_t > 15$)	175.3	5.4

Table 5.5: The median mass and median statistical uncertainty from 500 pseudo-experiments for various combinations of subsamples.

- SLT Tagged (No SVX)
- Not Tagged with the tighter kinematic requirement that all 4 jets have $E_T > 15$ *GeV* and $\eta < 2$.

This combination of four subsamples, from 500 pseudo-experiments, gives a statistical uncertainty of 5.4 GeV/c^2 compared to 6.4 GeV/c^2 from the SVX or SLT Tagged sample. This reduction in the statistical uncertainty is equivalent to increasing the size of the current SVX or SLT Tagged data sample by approximately 40%. The mass measurement using only the SVX or SLT Tagged subsample is described elsewhere [36] [40]. This thesis will measure the top mass by combining the following four mass subsamples: the SVX Double Tagged, the SVX Single Tagged, the SLT Tagged (No SVX), and the Not Tagged (with all four jets having $E_T > 15$ GeV/c^2 and $\eta < 2$.

5.5 Parameterized Likelihood Method

The main difficulty with the discrete likelihood method is the limited amount of information it provides about the true shape of the likelihood function versus top mass. The plotted likelihood values are correlated due to the common background template in the fits, and they must be interpolated to yield a top mass measurement. This interpolation gives poor results when the negative log-likelihood is very flat near its minimum (as is the case for the sample of events tagged by SLT but not by SVX). A corresponding systematic uncertainty must be introduced, but it is far from obvious how to properly calculate it. To avoid these problems, f_s is introduced as a smooth function of both $M_{\rm rec}$ and $M_{\rm top}$ [37]. For fixed $M_{\rm top}$, f_s can be adequately represented by a sum of two components, a Gaussian which describes mainly events where all the parton-jet assignments are correctly reconstructed, and a gamma distribution for the remaining events:

$$f_s(M_{\rm rec}, M_{\rm top}) \;=\; \frac{(1-p_6)}{\sqrt{2\pi}\,p_5}\, e^{-\frac{1}{2}\left(\frac{M_{\rm rec}-p_4}{p_5}\right)^2} \;+\; \frac{p_6\, p_3^{(1+p_2)}}{\Gamma(1+p_2)}\,(M_{\rm rec}-p_1)^{p_2}\; e^{-p_3(M_{\rm rec}-p_1)} \tag{5.4}$$

The parameters of the Gaussian and gamma distributions are themselves linear functions of $M_{\rm top}$:

$$p_i \;=\; \alpha_i \;+\; \alpha_{i+6}\,(M_{\rm top} \;-\; 175) \tag{5.5}$$

In all, twelve parameters α_j are needed. Their nominal values α_{0j} are determined by a simultaneous fit to eighteen reconstructed-mass distributions calculated with the HERWIG program and corresponding to input top masses ranging from 120 to 220 GeV/c^2, in steps of 5 GeV/c^2.

Signal templates have been obtained for each of the four subsamples used to measure the top mass. Equation 5.4 provides a good fit in all four cases. Figures 5.7, 5.8, 5.9 and 5.10 show the template fits obtained for the subsamples of events with a single SVX tag, events with a double SVX tag, events with an SLT tag and no SVX tag, and untagged events with a 4th jet with $E_T \geq 15$ GeV and $|\eta| \leq 2.4$ respectively. In each figure, there are nine templates with $M_{\rm top}$ ranging from 155 to 195 GeV/c^2. For the background template, it was found that most

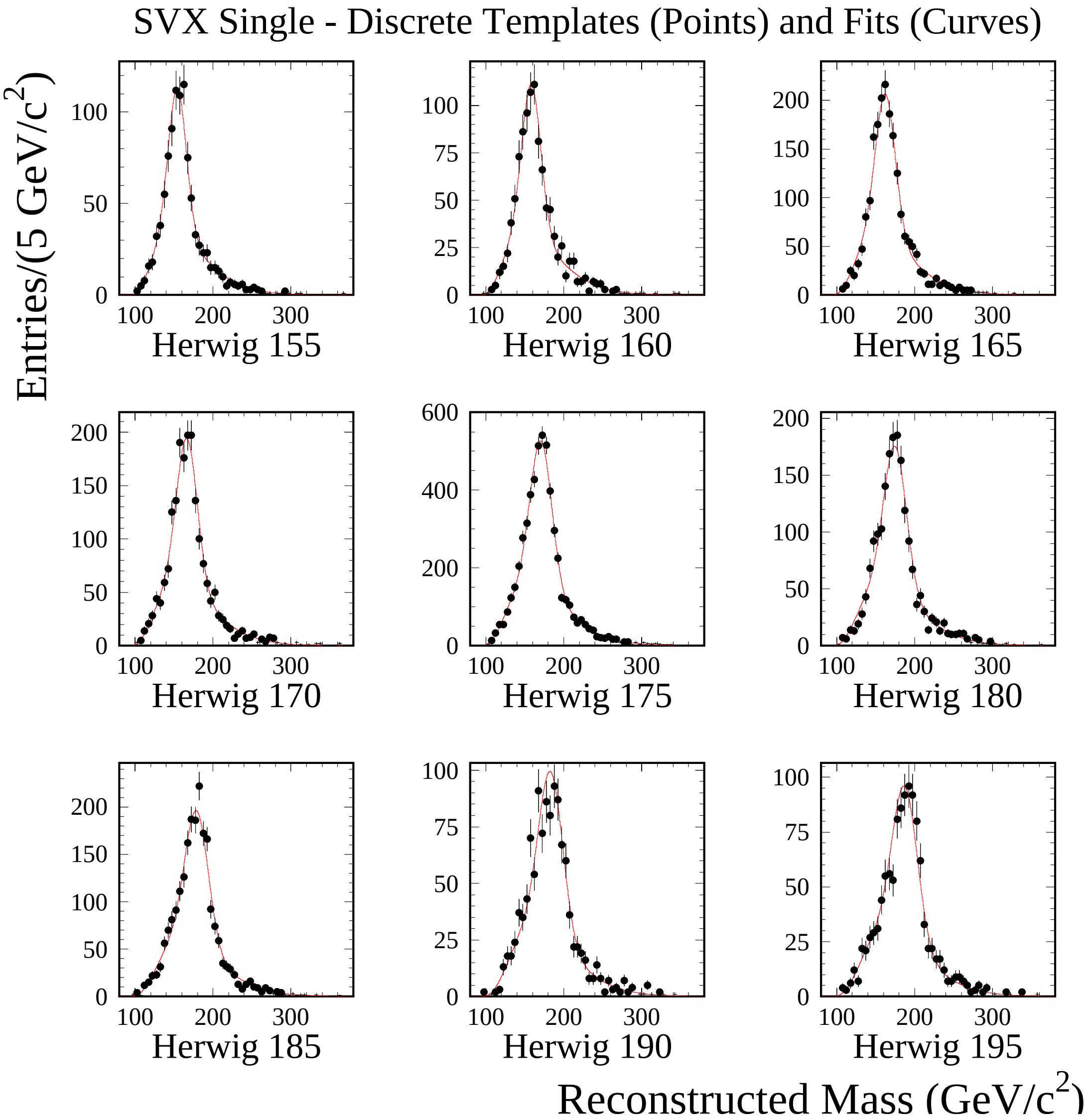

Figure 5.7: Fits to HERWIG templates for the subsample of SVX Single Tagged events, using the 12-parameter function cited in the text.

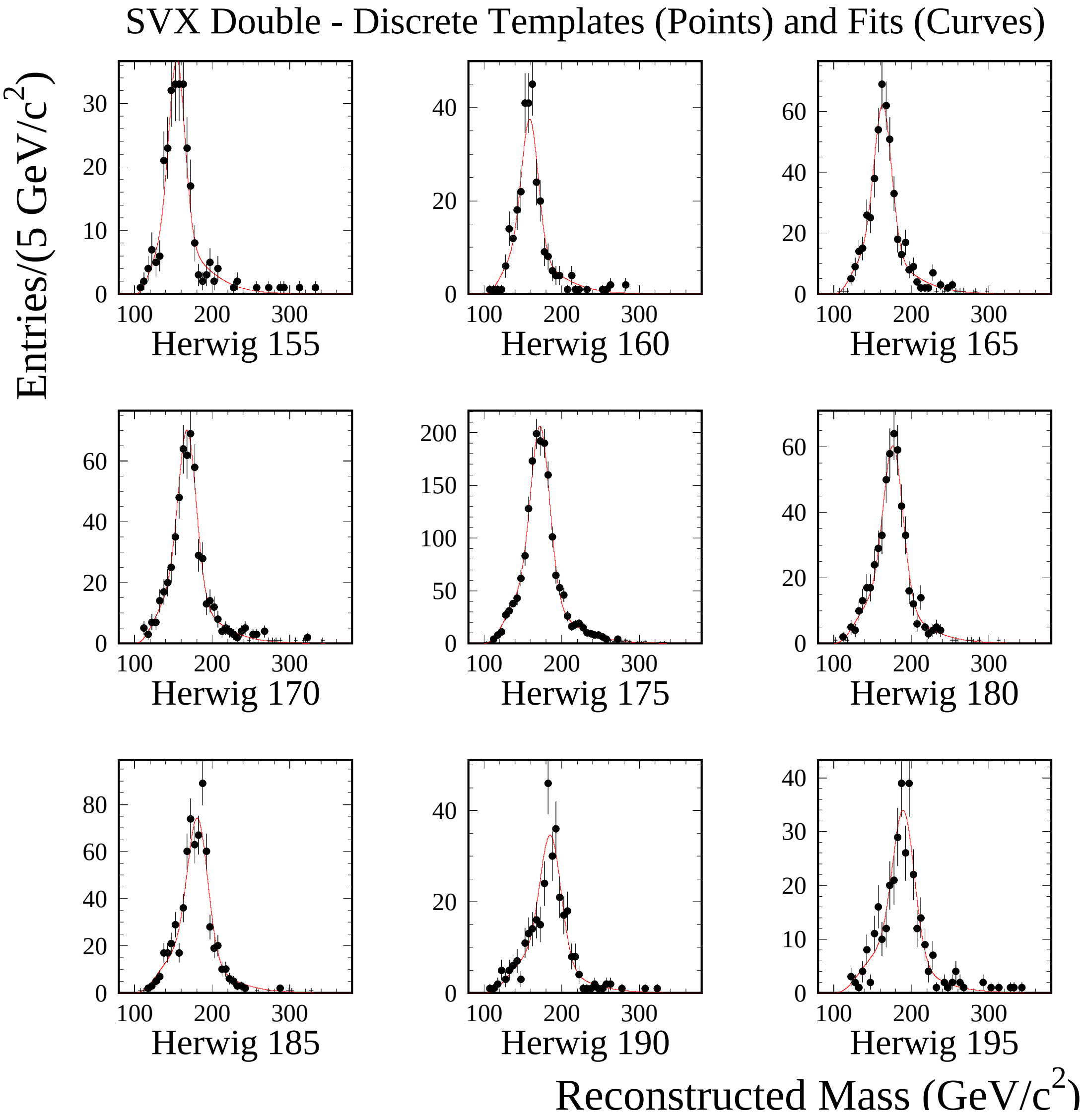

Figure 5.8: Fits to HERWIG templates for the subsample of SVX Double Tagged events, using the 12-parameter function cited in the text.

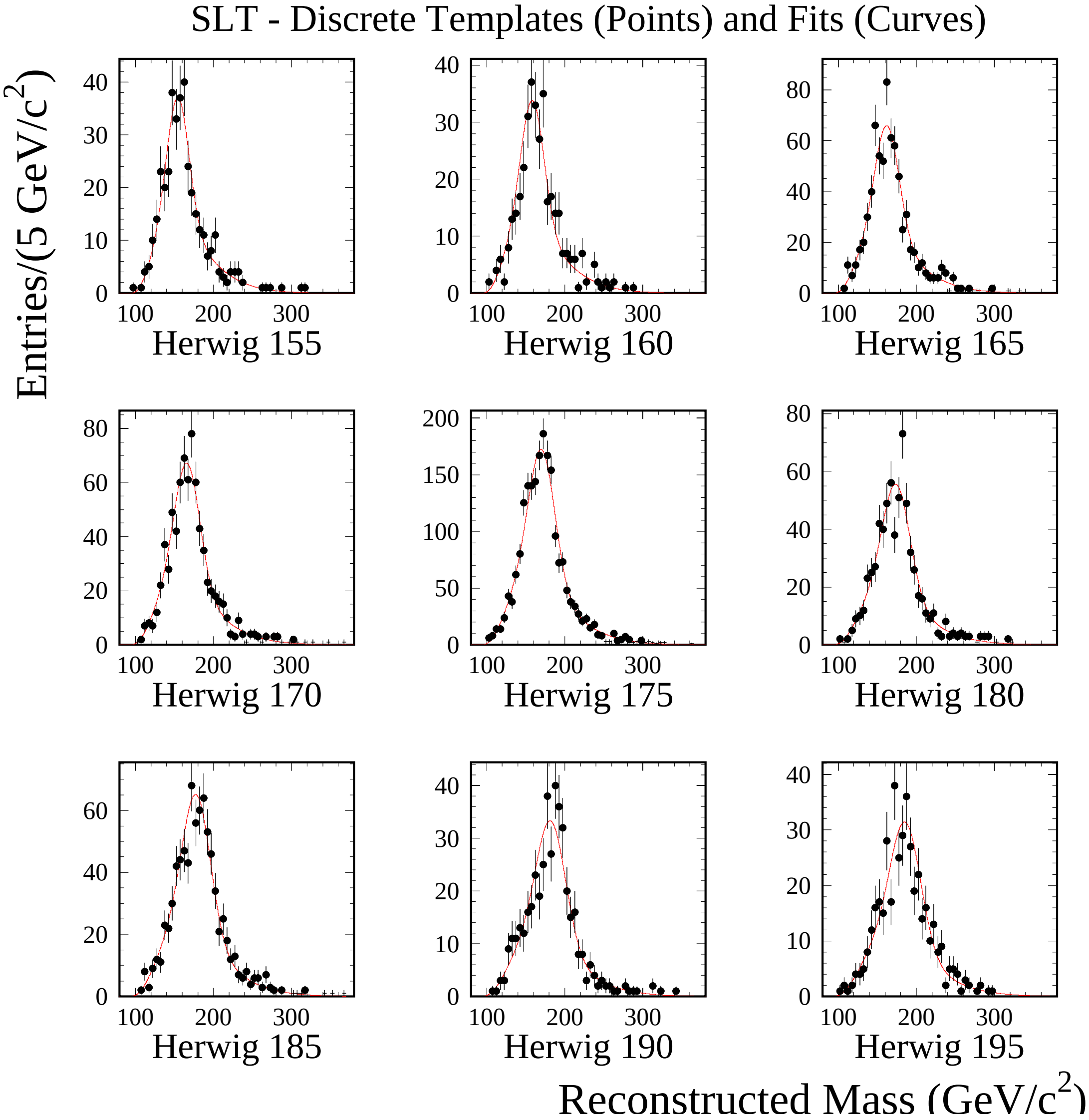

Figure 5.9: Fits to HERWIG templates for the subsample of SLT Tagged (No SVX) events, using the 12-parameter function cited in the text.

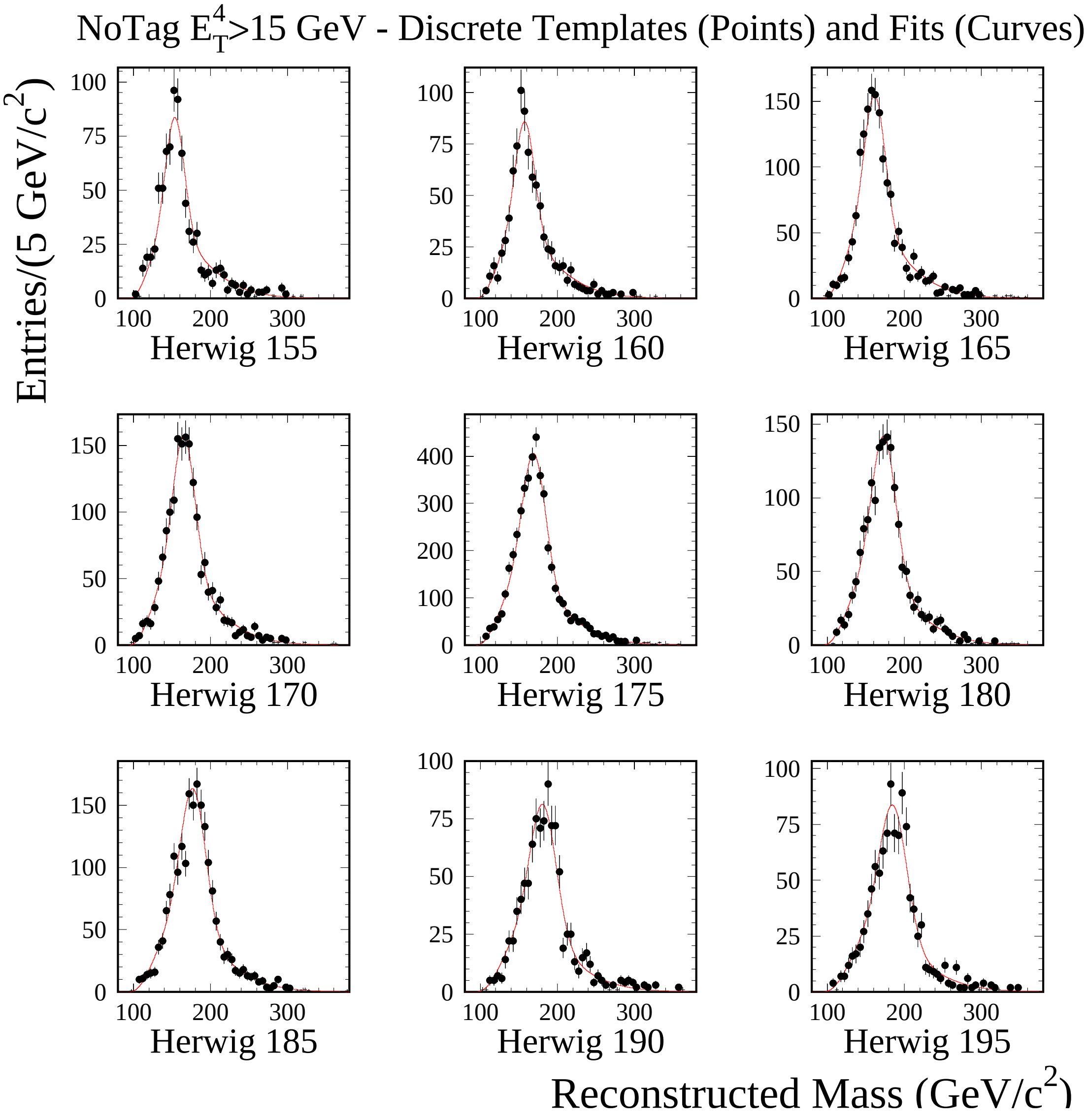

Figure 5.10: Fits to HERWIG templates for the subsample of No Tagged events, using the 12-parameter function cited in the text.

mass subsamples have a $M_{\rm rec}$ distribution which can be fit with a single gamma distribution. In the case of the Not Tagged subsample, a gaussian must be added to the gamma distribution to make the fit acceptable. The fits to the VECBOS templates are shown in Figure 5.11.

A significant advantage of using a single smooth function to represent $t\bar{t}$ templates with different true top mass is that this reduces the sensitivity to statistical fluctuations in individual templates. Information about the high-statistics template for $M_{\rm top} = 175$ GeV/c^2 is used to improve our knowledge of the shape of lower-statistics templates at other top masses. However, one must be careful that this global fitting procedure does not introduce biases. Several checks were made on the quality of the signal and background template fits for each subsample:

- The reduced χ^2's of the fits are all close to 1.0.

- The pulls on the bins of the $M_{\rm rec}$ histograms have means around 0.0 (see Figures 5.12 and 5.13) and widths around 1.0 (see Figures 5.14 and 5.15), as expected; for the signal distributions, this indicates that the fits are not biased by templates for a specific $M_{\rm top}$ (for example at the edge of the $M_{\rm top}$ range). The pull is defined as the fit mass returned from a pseudo-experiment minus the input mass (in this case 175 GeV/c^2) divided by the statistical uncertainty returned from the fitter.

- The fit was repeated without the high-statistics template for $M_{\rm top} = 175$ GeV/c^2, and compared the resulting $f_s(M_{\rm rec}, M_{\rm top} = 175\,{\rm GeV/c^2})$ with the 175 GeV/c^2 template; good agreement was found.

- Pseudo-experiments were run in which event samples were generated according to a given signal template, and then fit to the parameterized distribution f_s. The median mass from the pseudo-experiment fits agrees with the input

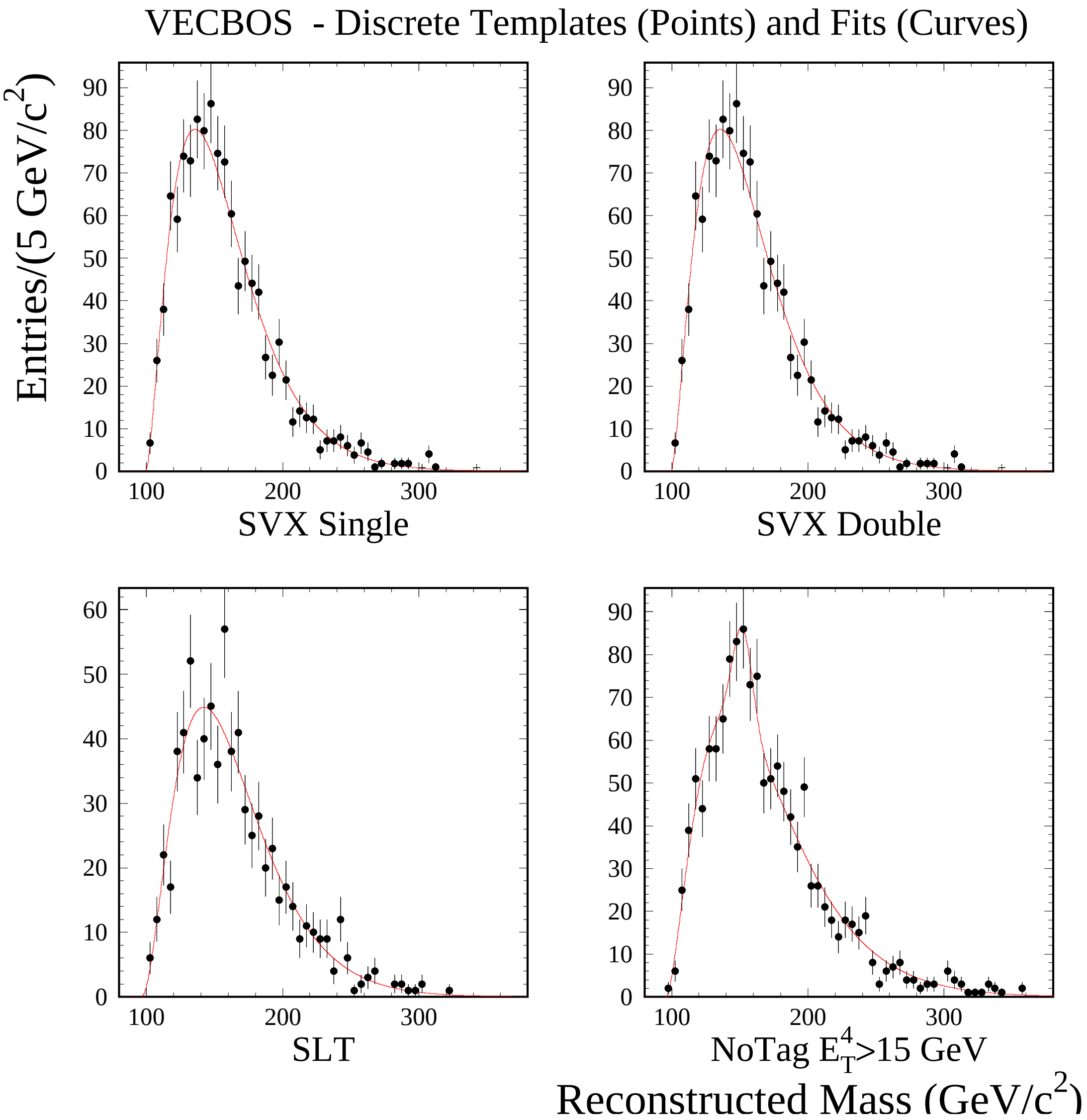

Figure 5.11: Three-parameter fits to the VECBOS SVX Single, SVX Double and SLT (No SVX) tagged templates, and the six-parameter fit to the VECBOS No Tagged template.

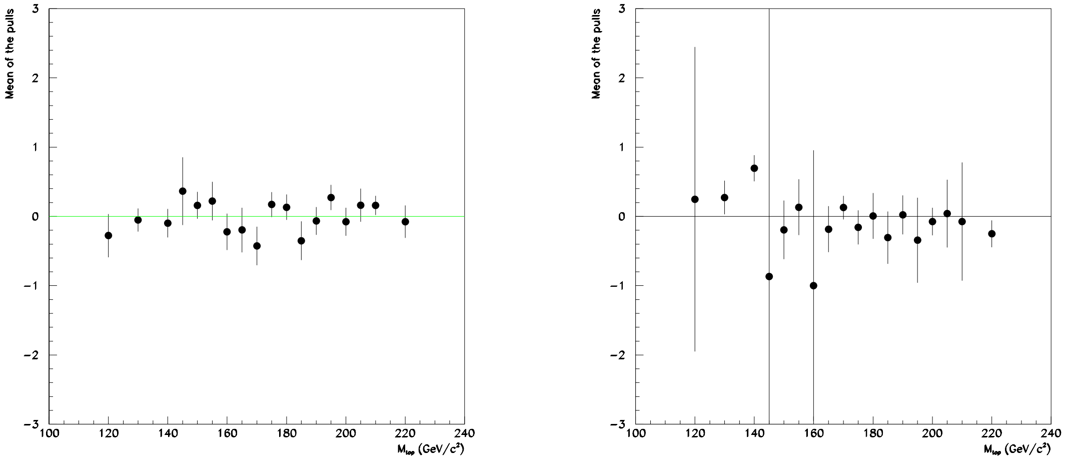

Figure 5.12: Mean of the pulls distributions from the template fits for the SVX Single Tagged (left) and SVX Double Tagged (right) samples, as a function of top mass.

mass used to generate the events.

A maximum-likelihood method is used to extract a top mass measurement from a sample of events which have been reconstructed according to the $t\bar{t}$ hypothesis. The likelihood function is the product of four factors:

$$\mathcal{L} = \mathcal{L}_{shape} \times \mathcal{L}_{count} \times \mathcal{L}_{backgr} \times \mathcal{L}_{param}, \tag{5.6}$$

where:

$$\begin{aligned}
\mathcal{L}_{shape} &= \prod_{i=1}^{N} \frac{N_s\, f_s(M_i; M_{\mathrm{top}}, \vec{\alpha}) + N_b\, f_b(M_i; \vec{\beta})}{N_s + N_b} \\
\mathcal{L}_{count} &= \frac{e^{-(N_s+N_b)}\, (N_s + N_b)^N}{N!} \\
\mathcal{L}_{backgr} &= \mathrm{Prob}(N_b) \\
\mathcal{L}_{param} &= e^{-\frac{1}{2}(\vec{\alpha}-\vec{\alpha}_0)^T U^{-1} (\vec{\alpha}-\vec{\alpha}_0) \,-\, \frac{1}{2}(\vec{\beta}-\vec{\beta}_0)^T V^{-1} (\vec{\beta}-\vec{\beta}_0)}.
\end{aligned}$$

The likelihood $\mathcal{L}_{shape}$ is the joint probability density for the N reconstructed masses

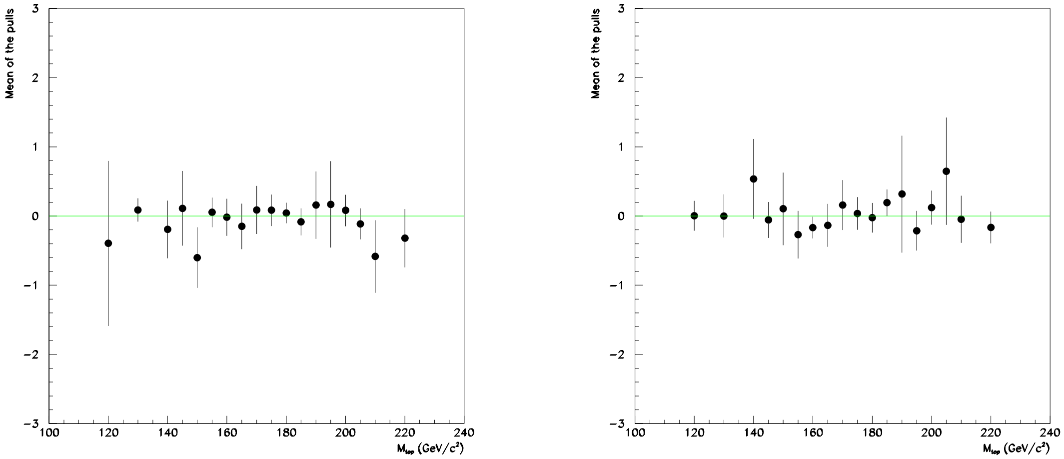

Figure 5.13: Mean of the pulls distributions from the template fits for the SLT (no SVX) Tagged (left) and No Tagged ($E_T > 15$) (right) samples, as a function of top mass.

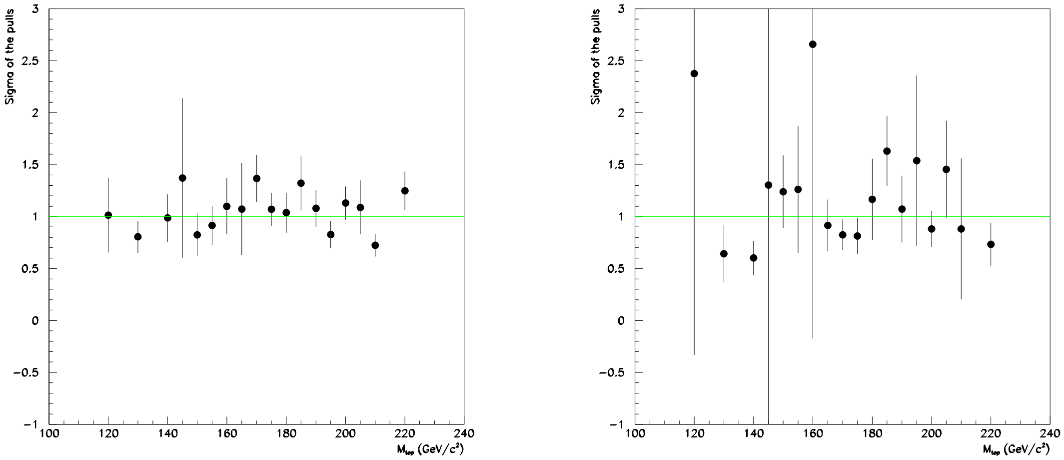

Figure 5.14: Width of the pulls distributions from the template fits for the SVX Single Tagged (left) and SVX Double Tagged (right) samples, as a function of top mass.

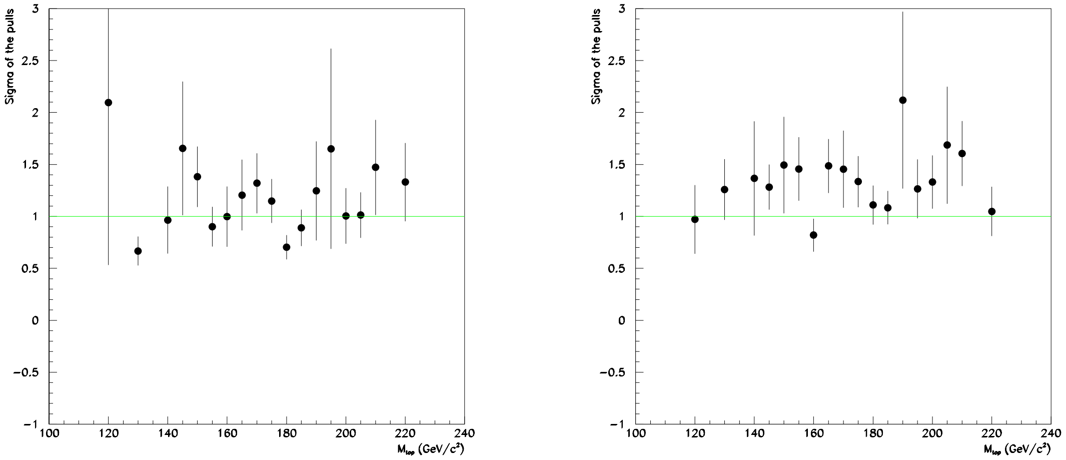

Figure 5.15: Width of the pulls distributions from the template fits for the SLT (no SVX) Tagged (left) and No Tagged (right) samples, as a function of top mass.

M_i in the sample to come from a parent distribution with N_s signal and N_b background events. The sum of N_s and N_b is the expectation value for the total number of observed events N, which is assumed to obey Poisson statistics, as expressed by the likelihood $\mathcal{L}_{count}$. The expected number of background events is itself constrained by an independent measurement which is summarized by the likelihood $\mathcal{L}_{backgr}$. Finally, the parameters α_j and β_j which determine the shape of f_s and f_b are constrained by $\mathcal{L}_{param}$ to be near the fitted values α_{0j} and β_{0j}, whose covariance matrices are U and V respectively. The inclusion of $\mathcal{L}_{param}$ in the likelihood definition takes into account the finite statistics of the Monte Carlo samples used to determine f_s and f_b. The likelihood $\mathcal{L}$ is maximized with respect to $M_{\rm top}$, N_s, N_b, $\vec{\alpha}$ and $\vec{\beta}$.

5.6 Checks

A number of checks can be done to make sure that the likelihood fitting technique just described works correctly. For instance, if a sample of HERWIG ($M_{top} = 175$

GeV/c^2) $t\bar{t}$ events is input into the fitter the top mass that is returned should be $\sim$ 175. To check the fitting method, 5000 pseudo-experiments were generated from the HERWIG ($M_{top} = 175$ GeV/c^2) template and fit with the standard templates. If the fitter is working correctly, the pull distribution of the pseudo-experiments should have a mean of zero and a width of one. The pull distribution is defined as the fit mass returned from a pseudo-experiment minus the input mass (in this case 175) divided by the statistical uncertainty returned from the fitter. Figure 5.16 shows the pull distribution for the 5000 pseudo-experiments. Figure 5.16 has a mean of zero and a width of 1.04 which indicates that, on average, the statistical uncertainty from fitter is slightly underestimated.

Additional studies have been done to make sure that the statistical uncertainty returned from the fitter is correct. If an infinite number of experiments were run the statistical uncertainty would be equal to the width of the top mass distribution plotted for all of the pseudo-experiments with that statistical uncertainty. To check that this was true, 5000 pseudo-experiments were generated and then divided up into roughly equal bins based on the returned statistical uncertainty of the experiment. The top mass distribution was plotted for each of the statistical uncertainty bins and fit to a gaussian to measure its width. Figure 5.17 shows the statistical uncertainty returned from the mass fitter versus the width of the mass distribution for events which have statistical uncertainties in the range of the horizontal error bar. If the statistical uncertainty returned by the mass fitter is correct it should be equal to the width of the mass distribution for that statistical uncertainty bin and should lie along the line which has a slope of one. Points which low below (above) the line of slope one indicate that the statistical uncertainty from the fitter is an overestimate (underestimate). Figure 5.17 shows that the Monte Carlo pseudo-experiments follow the line with slope of 1.0.

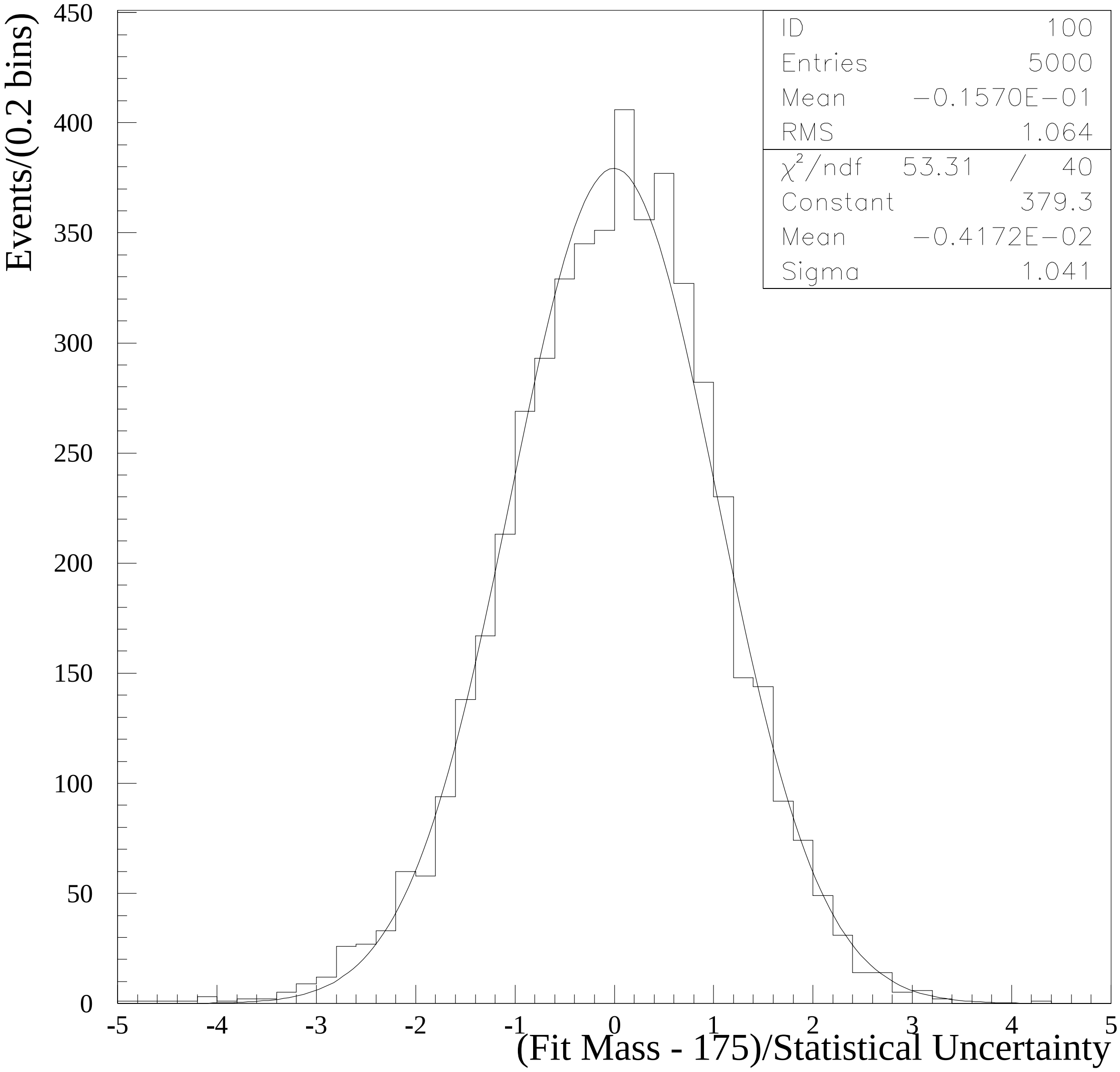

Figure 5.16: The pull distribution for 5000 pseudo-experiments chosen from standard HERWIG with $M_{top} = 175$ GeV/c^2. The pull is defined as fit mass returned from a pseudo-experiment minus the input mass (175) divided by the statistical uncertainty returned from the fitter. The fit mass should be close to 175 so the pull distribution should be centered around zero. If the fitter is calculating the statistical uncertainty correctly the width of the pull distribution should be equal to 1.0.

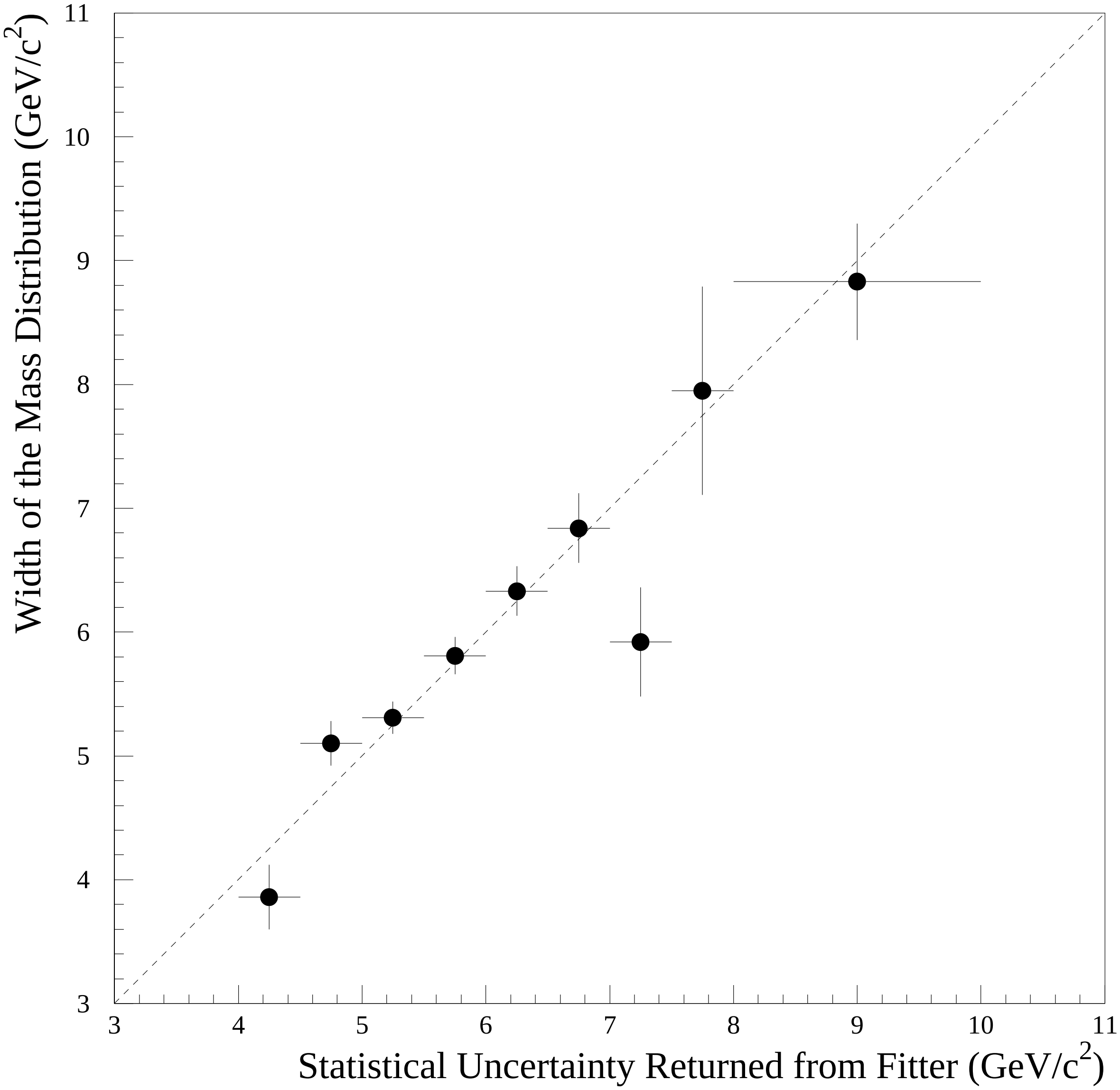

Figure 5.17: The width of the mass distribution as a function of statistical uncertainty versus the returned statistical uncertainty for pseudo-experiments.

Subsample	Measured $M_{\rm top}$ (GeV/c^2)
SVX Double Tag	$170.1^{+9.5}_{-9.0}$
SVX Single Tag	$178.0^{+8.3}_{-7.5}$
SLT Tag (No SVX)	142^{+33}_{-14}
No Tag ($E_T > 15$)	$180.8^{+9.6}_{-8.4}$

Table 5.6: The measured top mass and statistical uncertainty for each of the individual subsamples used to measure the top mass.

5.7 Results

The likelihood fitting technique is applied to the four mass subsamples in the data to give a combined likelihood. From the likelihood a top quark mass of $M_{\rm top} = 175.9 \pm 4.8$ GeV/c^2 is obtained, where the uncertainty corresponds to a half-unit change in the log-likelihood with respect to its minimum, and represents the statistical uncertainty from both the data and the size of the Monte Carlo samples used in calculating f_s and f_b. Figure 5.19 shows the reconstructed mass distribution for the sum of the four subsamples. The inset shows the shape of the corresponding sum of negative log-likelihoods as a function of top mass. The reconstructed mass distribution and negative log-likelihood are shown for each of the individual subsamples in Figure 5.18. The top mass measurements for the individual subsamples are summarized in Table 5.6.

To determine how likely it is to obtain a top mass with a statistical uncertainty of 4.8 GeV/c^2, studies with ensembles of simulated experiments yield an 11% probability for obtaining a statistical uncertainty of this size or smaller. In addition, an unbinned Kolmogorov-Smirnov (KS) test was performed to estimate how well the data fit the Monte Carlo model. Figure 5.20 shows the cumulative distribution of the 76 data events, compared with the linear combination of top and background probability distributions which was obtained from the likelihood

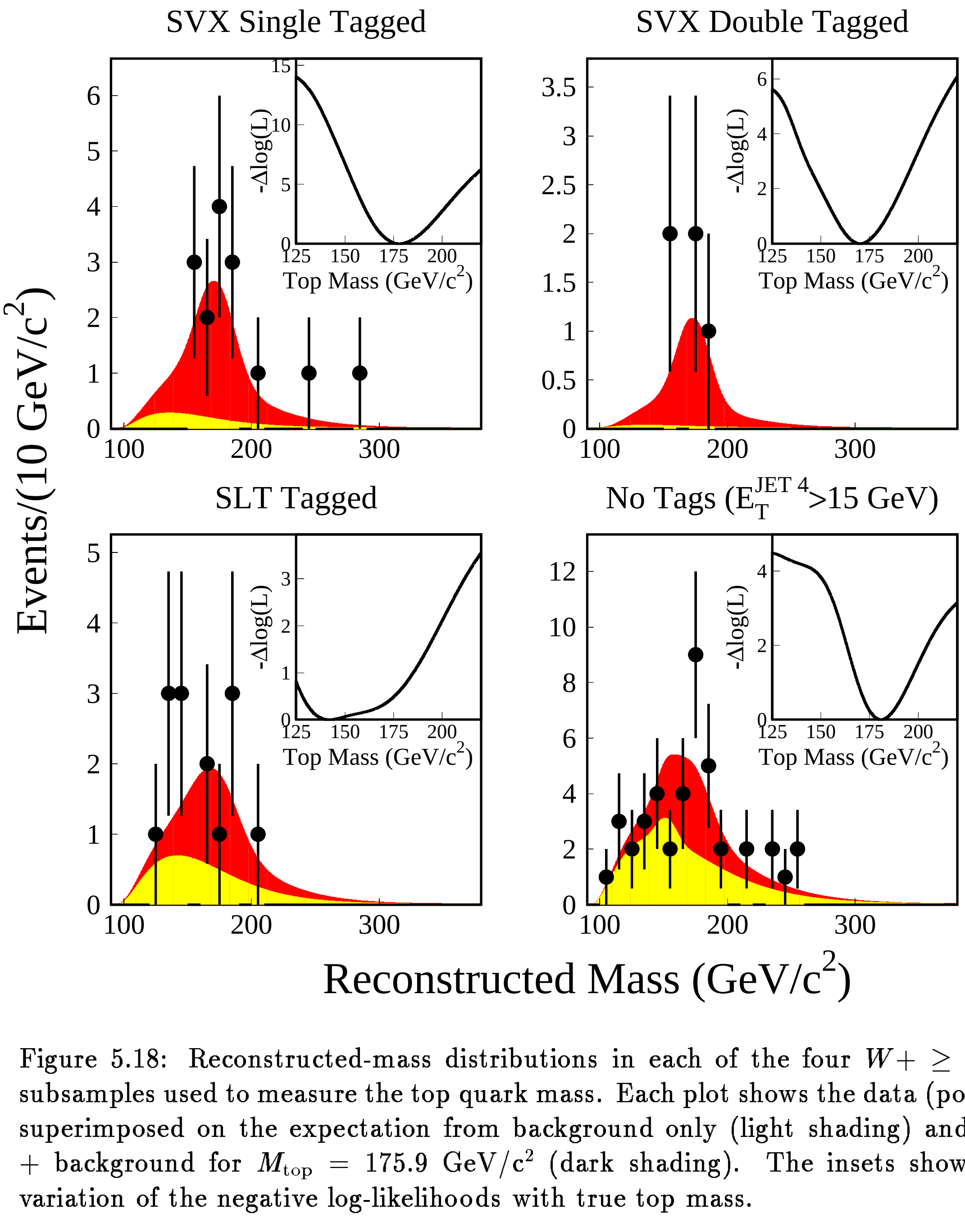

Figure 5.18: Reconstructed-mass distributions in each of the four $W+ \geq$ 4-jet subsamples used to measure the top quark mass. Each plot shows the data (points) superimposed on the expectation from background only (light shading) and top + background for $M_{\rm top}$ = 175.9 GeV/c^2 (dark shading). The insets show the variation of the negative log-likelihoods with true top mass.

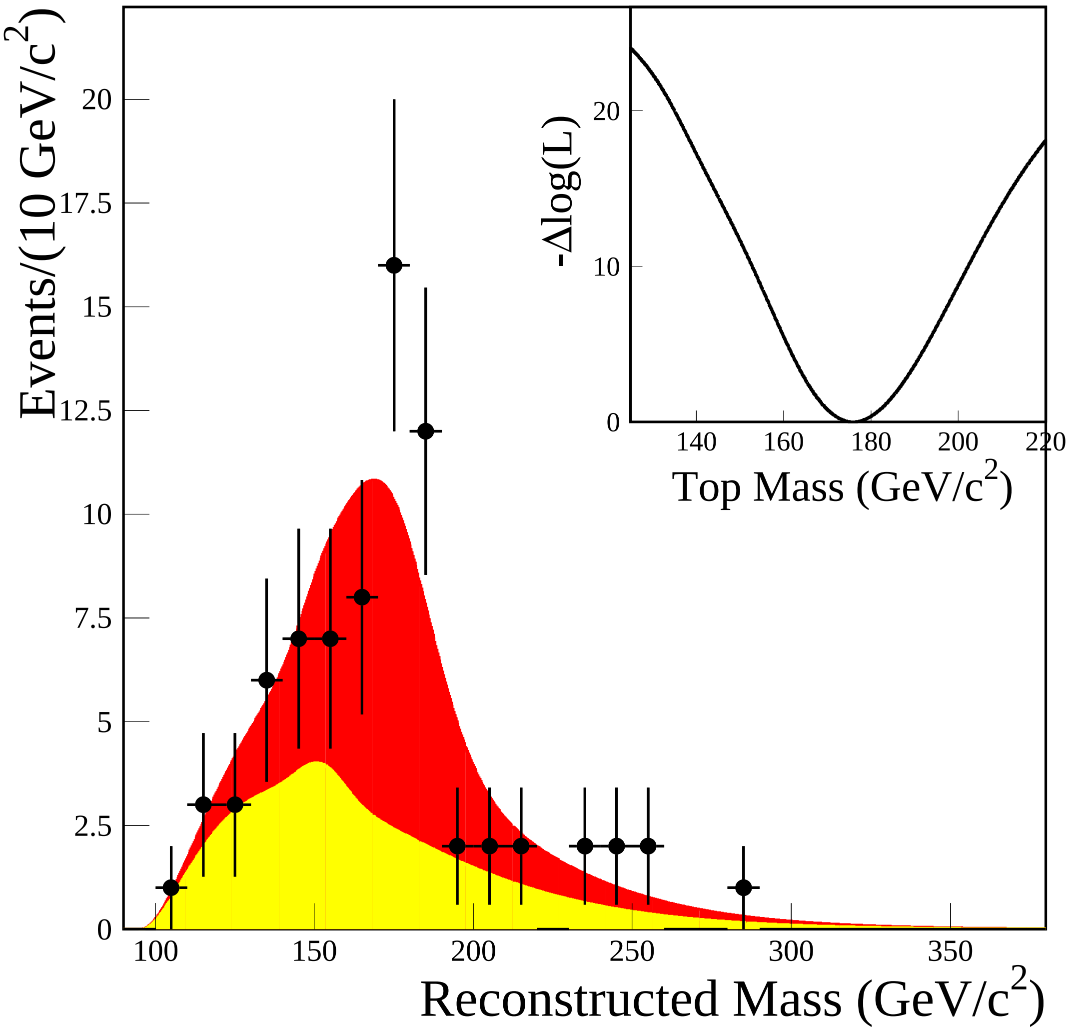

Figure 5.19: Reconstructed-mass distribution of the four $W+\geq 4$-jet subsamples combined. The data (points) are compared with the expectation from background only (light shading) and top + background for $M_{\rm top} = 175.9$ GeV/c^2 (dark shading). The inset shows the variation of the combined negative log-likelihood with true top mass.

fit. The KS statistic is defined as the maximum vertical distance between the two cumulative distributions, multiplied by the square root of the number of data events. To extract a confidence level from this statistic, it is necessary to take into account the fact that several parameters used in the Monte Carlo model were extracted from the data (namely the expected numbers of top and background events in each of the four subsamples). In other words, the likelihood fit biases the KS statistic towards smaller values, so that one cannot simply use standard statistical tables (or the standard CERN library routine PROBKL) to calculate the confidence level. Instead, a large number of pseudo-experiments, each with 76 events, were generated and fit to a top plus background probability density. The KS statistic was then calculated between the pseudo-experiment sample and the data result. The distribution of the KS statistics for all pseudo-experiments is shown in Figure 5.21. Using Figure 5.21(b), the fraction of pseudo-experiments with a KS statistic above the observed one is the sought-for confidence level. It is found to be 64%.

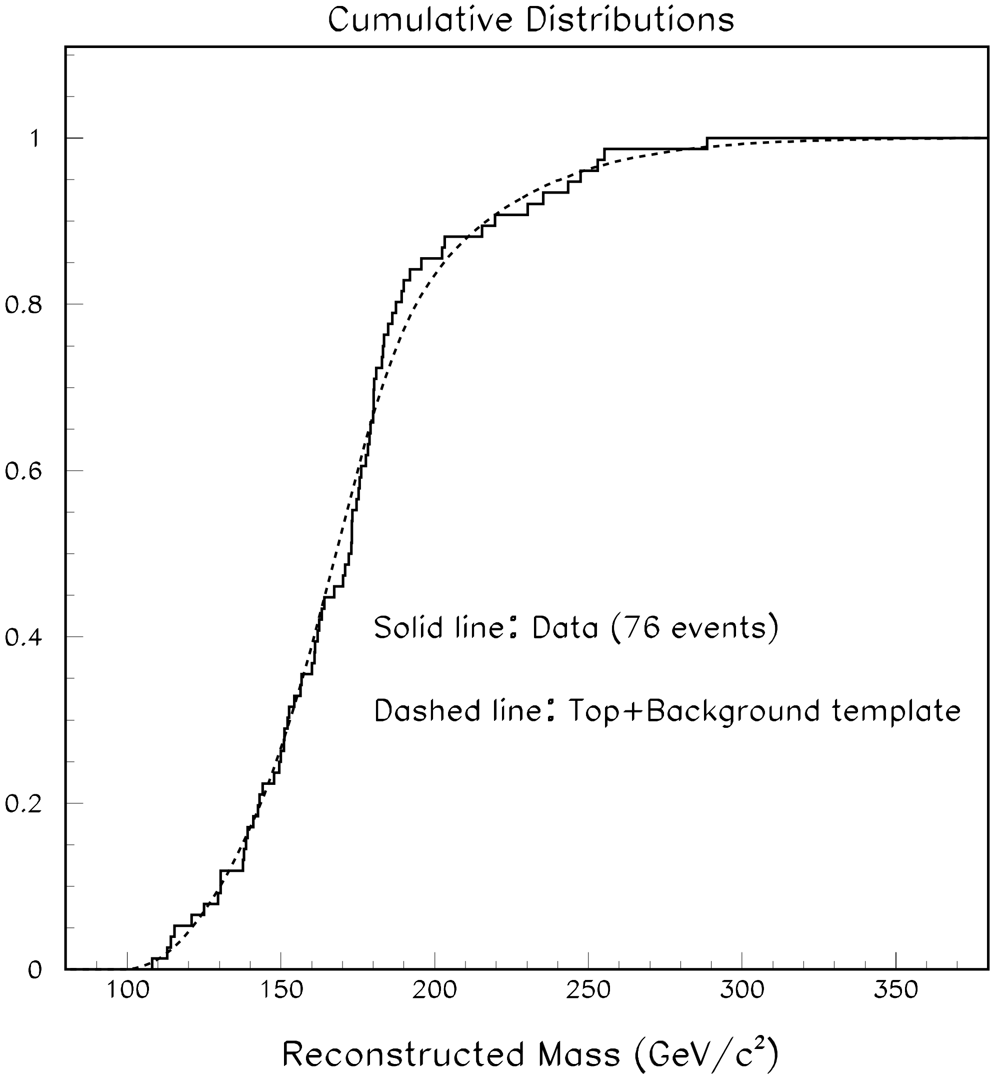

Figure 5.20: The solid line shows the cumulative distribution of the reconstructed masses of the 76 data events used in the optimized analysis. The dashed line is the weighted sum of top and background templates which fits the data best. This plot is used to estimate how well the data fits our model by applying a Kolmogorov-Smirnov test (see text).

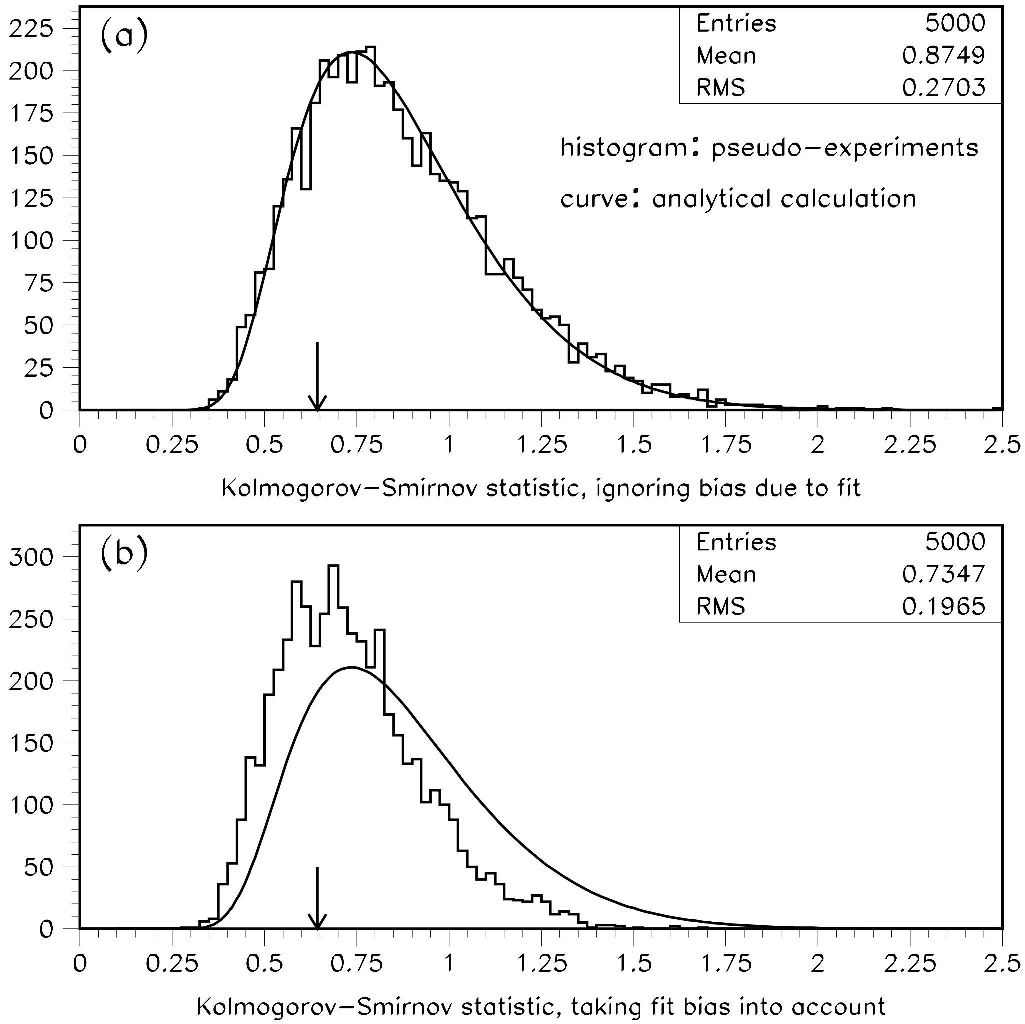

Figure 5.21: Distributions of the Kolmogorov-Smirnov (KS) statistic. The histogram in (a) shows the result of 5000 pseudo-experiments where the KS statistic was calculated between each pseudo-experiment sample and the parent distribution used to generate all samples. The curve is the standard analytical KS distribution function provided by the CERN library. For (b), the KS statistic was calculated between each sample and the distribution that best fit that particular sample. The same curve as in (a) is shown for comparison. The KS statistic observed in the data is indicated by arrows.

Chapter 6

Systematic Uncertainties on the Top Mass

The total systematic uncertainty assigned to the top mass is an attempt to quantify any potential biases that may have occurred in the measurement process. These biases may arise from uncertainties in the detector's performance, choice of theoretical models, and the method chosen for fitting. This chapter explains how the following systematic uncertainties were estimated: (1) the detector's jet energy scale, (2) the mapping of jet energies to parton energies, (3) the amount of initial and final state radiation, (4) the shape of the reconstructed top mass distribution for background events, (5) the *b*-tagging efficiency versus jet E_T, (6) different parton distribution functions, and (7) differences between Monte Carlo generators. Each systematic is calculated using the same general method.

6.1 Method

The systematic uncertainty due to a particular source is taken to be the difference in the measured top mass between the standard or default fitting conditions and when that condition is varied within its uncertainty. To decouple shifts due to systematic effects from shifts due to statistical fluctuations in the observed data sample, the systematic uncertainties are estimated by running large numbers of Monte Carlo "pseudo-experiments". These pseudo-experiments are treated in the same manner as the data with each experiment having the same total number of events as observed in the data. The number of background events for a given pseudo-experiment is chosen randomly from a binomial distribution, whose probability parameter is drawn from the calculated background probability distribution which was described in Section 5.2. The number of top events for a given pseudo-experiment is the total number of observed data events minus the number of background events just chosen. Then the correct number of top and background events are drawn from the parameterized HERWIG top and VECBOS background probability distributions, respectively. The parameterized probability distributions were obtained by using the fitting method described in Section 5.5. Each pseudo-experiment is fit in exactly the same manner as the data to obtain a fitted top mass, i.e. by fitting the chosen pseudo-experiment events to the parameterized HERWIG and VECBOS templates.

To calculate the systematic uncertainty due to a given parameter, the parameter in question is shifted and a set of 5000 pseudo-experiments is generated. A distribution of 5000 "measured top masses" is obtained from the shifted pseudo-experiments. The mass distribution from the shifted pseudo-experiments is then compared to a mass distribution from pseudo-experiments that were generated from the default, unshifted top and background probability distributions. The difference between the medians of the shifted and unshifted distributions is taken to be the systematic uncertainty on the top mass.

With the above procedure, it is estimated that the systematic uncertainties can be determined to within approximately 0.2 GeV/c^2. This uncertainty on the systematic uncertainties is due to the finite statistics of our Monte Carlo samples. It was obtained by recalculating the systematic uncertainties using pseudo-experiments generated from top and background probability distributions whose parameters were shifted by the uncertainties of the parameterized fits to the templates.

6.2 Jet Energy Scale

The largest systematic uncertainty on the top mass comes from the jet energy measurement. Each jet energy correction, described in Section 5.1.1, has an energy-dependent uncertainty with it. To calculate the uncertainties on these jet corrections Equation 5.1 is differentiated. A brief description of the uncertainty associated with each jet energy correction described in Section 5.1.1 is given below.

Absolute Jet Energy Scale Correction

The uncertainty on the absolute jet energy scale has two components: 1) detector response and 2) fragmentation effects. The systematic uncertainty due to the detector response contains two uncertainties, one for the calorimeter calibration and one for the calorimeter stability. The uncertainty on the calorimeter stability correction is 1% of the uncorrected jet P_T and it is applied to the uncorrected jet energy. The calorimeter calibration systematic was obtained by varying each of the pion, electron and photon responses by one standard deviation and adding the effect of each in quadrature. The uncertainty on the fragmentation effects was obtained by varying the charged particle detection efficiency by one standard deviation. The jet energy uncertainties from the calorimeter calibration correction, fragmentation effects correction and the underlying event correction for the primary vertex (described below) are added in quadrature. This overall uncertainty is applied to the jet E_T after the relative and absolute jet corrections. The uncertainty in the jet E_T scale due to the calorimeter calibration, fragmentation and underlying event (described below) is shown in Figure 6.1.

Underlying Event Correction

The underlying event correction has two components; one for the primary vertex and one to take into account multiple interactions in the same beam crossing. The uncertainty in the correction for the primary vertex, UE, was obtained by varying the correction factor by one standard deviation (which is approximately 30% of itself). This uncertainty is applied with the absolute energy correction uncertainty as described above. The uncertainty on the underlying event correction for multiple vertices, UEM, is 100 MeV per each additional vertex besides the primary vertex. This uncertainty is applied after the relative jet energy corrections have been applied to the jet.

Relative Jet Energy Scale Correction

The uncertainty on the relative jet energy scale correction depends on the η of the jet. The uncertainty varies from 0.2% to 4% of the relative correction itself. Table 6.1 gives the percent uncertainty on the relative correction for various ranges of $|\eta|$. This uncertainty is applied after the relative jet energy corrections.

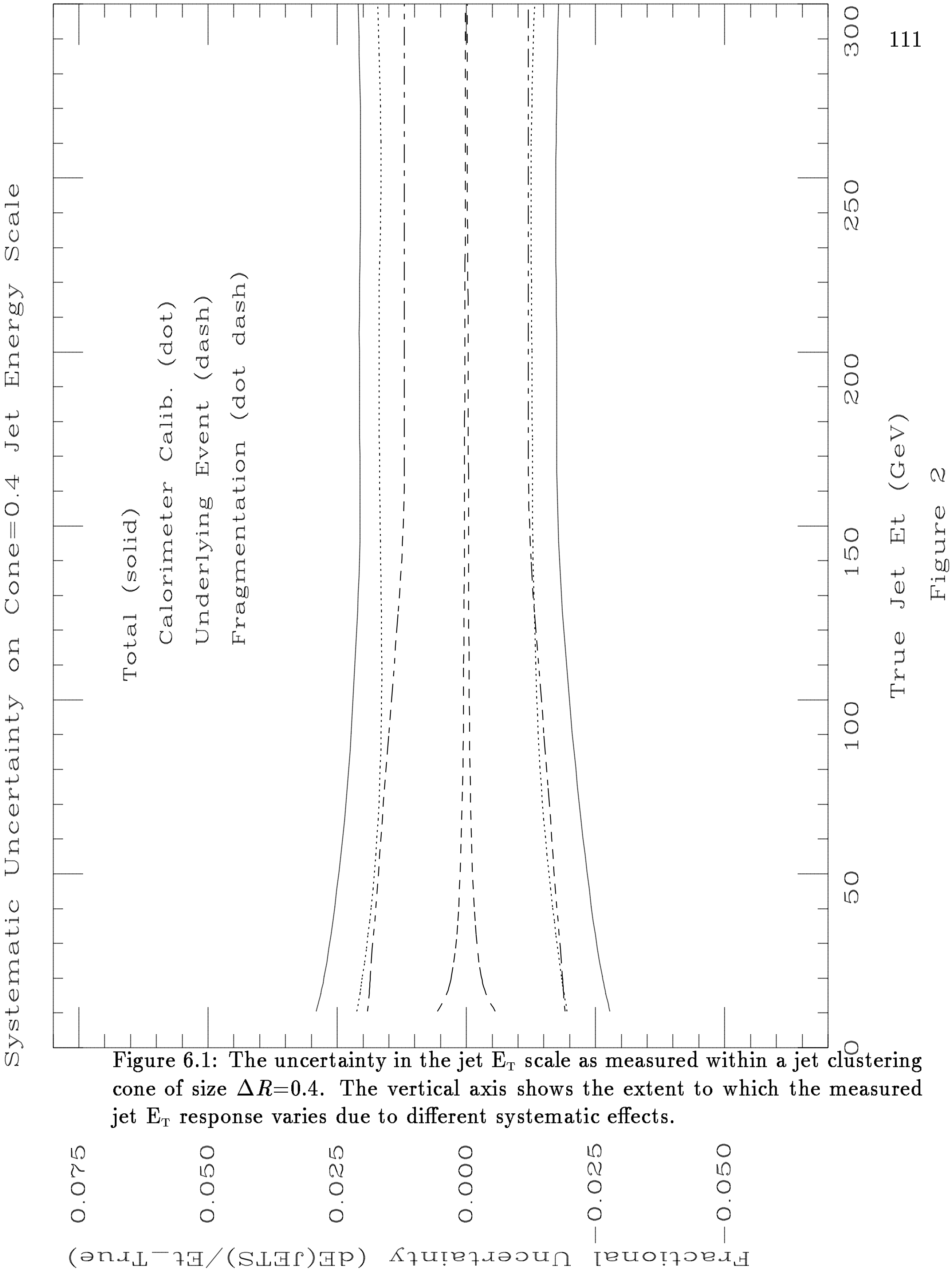

Figure 6.1: The uncertainty in the jet E_T scale as measured within a jet clustering cone of size ΔR=0.4. The vertical axis shows the extent to which the measured jet E_T response varies due to different systematic effects.

$\lvert\eta\rvert$ interval	% Uncertainty on Relative Correction
0.0 - 0.1	2%
0.1 - 1.0	0.2%
1.0 - 1.4	4%
1.4 - 2.2	0.2%
2.2 - 2.6	4%

Table 6.1: The percentage of the relative jet energy correction uncertainty for various $\lvert\eta\rvert$s.

Energy Outside of the Jet Cone Correction

The uncertainty on the fraction of energy in a jet that is outside of a cone of ΔR=0.4 is divided into two components; soft gluon radiation and splash out. The purpose of these jet corrections was given in Section 5.1.1. The uncertainty on the soft gluon radiation correction is taken to be one standard deviation of itself. The uncertainty on the soft gluon correction falls from 6% to 1.4% of the correction as the jet E_T increases from 10 GeV to 120 GeV. This is determined by comparing the energy in an annulus around a jet in data and Monte Carlo Z+jet events. The splash out correction, or energy deposited outside of a cone of ΔR=1.0, has an uncertainty of 1 GeV. Both of these uncertainties are applied after all of the jet corrections have been applied.

Table 6.2 shows the approximate size of the uncertainty for each jet energy correction and in what order the uncertainty is applied. Each uncertainty is applied in the positive and negative direction which causes the jet E_T to become larger or smaller, respectively. Each uncertainty is applied in the positive (negative) direction to the measured jet E_T to obtain a positive (negative) shift in the jet E_T. All of the positive (negative) jet shifts are then added in quadrature and applied

Correction	Systematic Uncertainty	Where Applied
Absolute Jet Energy (includes UE)	$\approx$2.5%	After relative and absolute corrections
Calorimeter Stability	1.0%	Raw E_T
Underlying Event (for multiple vertices)	100 MeV/vertex	After relative and before absolute correction
Relative Jet Energy	0.2-4% of f_{rel}	After relative correction
Soft Gluon Radiation	6-1.4%	After all jet corrections
Energy Outside Cone	1 GeV	After all jet corrections

Table 6.2: The approximate size of the uncertainties on the jet energy corrections and where the uncertainties are applied to the jet E_Ts.

to the jet E_T to obtain a total positive (negative) shift which is then applied as an overall E_T shift to all jets in the HERWIG ($M_{\rm top}$ = 175 GeV/c^2) sample. The total uncertainty on the corrected jet E_T for an observed jet E_T of 40 GeV, varies between 3.4% and 5.6% of its E_T, depending on the pseudo-rapidity of the jet. The mass shift between the medians of the negatively (positively) shifted pseudo-experiments and the default pseudo-experiments gives a systematic uncertainty due to the jet energy scale of $\pm$4.4 GeV/c^2.

6.3 Initial and Final State Radiation

The second largest systematic uncertainty on the top mass is due to the uncertainty in the rate of high transverse momentum gluons which are radiated from either the initial or final state of a $t\bar{t}$ event. In measuring the top mass it is assumed that the 4 highest E_T jets in the event are the jets associated with the partons from the top decay, two bottom quarks and two light quarks from a hadronic W decay. However, Monte Carlo studies indicate that a significant fraction of the time at least one of the four highest E_T jets does not match to the direction of a top decay parton. These jets are typically due to gluons radiating off of one of the initial or final-state partons.

To study the effects of gluon radiation on the top mass, it is necessary to be able to distinguish between jets which come from gluon radiation and jets which come from the partons in the top decay. Using Monte Carlo events, it is possible to match the jets used in the mass fit back to the top decay partons in the event generator. Ideally one would like to explicitly identify which partons originated which jets, allowing one to know if a jet came from a b quark, a light quark, or a gluon. Tracing backwards, from jet to originating parton, along the decay chain in the event generator is quite complicated. An alternative approach is to start from the top decay partons and locate which of the jets used in the mass fit is nearest. If the distance between the parton and the nearest jet is greater than $\Delta R = 0.4$, the jet is defined to be a "gluon jet".

Using this definition of a gluon jet, Monte Carlo samples can be divided into two categories: 1) no gluon events and 2) gluon events. The "no gluon" events are events in which all four of the mass jets match to partons from the top decay within a cone of $\Delta R = 0.4$. The "gluon" events are events for which at least one of the four mass jets does not match to a top decay parton. Applying the definition of a gluon jet to the standard HERWIG sample finds that 50% of HERWIG events are gluon events.

HERWIG was chosen as the standard Monte Carlo but HERWIG's modeling of radiation, particularly in top events, may be incorrect. Each Monte Carlo generator has its own radiation model, which affects the amount and distribution of gluon radiation. Therefore, it was prudent to examine the amount of gluon radiation in other generators, namely ISAJET and PYTHIA. Table 6.3 lists the percentage of b-tagged top events which are gluon events for HERWIG, ISAJET and PYTHIA at a generated top mass of 175 GeV/c^2. Both ISAJET and PYTHIA contain $\sim$20%

Generator	Number of Gluon Events (%)
HERWIG	$50 \pm 1\%$
ISAJET	$72 \pm 7\%$
PYTHIA	$73 \pm 5\%$

Table 6.3: The percentage of gluon events in a sample of b-tagged top events, with $M_{top} = 175$ GeV/c^2, for three different event generators.

Subsample	% of Gluon Events
SVX double tags	$30 \pm 5\%$
SVX single tags	$45 \pm 3\%$
SLT (No SVX) tags	$45 \pm 4\%$
No Tags ($E_T > 15$ all jets)	$50 \pm 3\%$

Table 6.4: The amount of gluon radiation in standard HERWIG for the four optimization subsamples.

more gluon radiation than HERWIG. Table 6.4 shows the percentage of events in HERWIG which are gluon events for the four mass subsamples used in this thesis.

6.3.1 Gluon Radiation in the Data

Instead of relying on the Monte Carlo generators to have the correct radiation modeling it would be best to measure the amount of gluon radiation directly from the data. Several top kinematic variables were studied to try to find one that could distinguish between events with gluon jets and events without gluon jets.

One kinematic variable with some distinguishing power is the number of extra jets in an event, N_{jextra}. The number of extra jets is the number of jets in an event, excluding the 4 highest E_T jets, with $E_T > 5$ GeV/c^2 and $\eta < 2.4$. The MNFIT [38] package was used to fit the distribution of the number of extra jets from the data to a combination of the no gluon event sample and the gluon event sample from HERWIG. By using data events with an SVX tag, the number of background events is significantly reduced and the background distribution in N_{jextra} can be ignored. The fit finds that the data wants $(50 \pm 50)\%$ of the events to be gluon events. The inability of the fitter to limit the allowed percentage of gluon radiation is due to the limited statistics of the data sample. Despite the low statistics it is still interesting to compare the N_{jextra} distribution between the data and various Monte Carlo samples. Figure 6.2 shows that there is poor agreement between the N_{jextra} distribution of the data to HERWIG samples with gluon events and without gluon events. The N_{jextra} distribution for standard HERWIG and PYTHIA compared to the data are shown in Figure 6.3. The data agrees, within statistics, with the amount of radiation in both HERWIG and PYTHIA.

Due to the limited statistics in the data, Monte Carlo must be relied upon to describe radiation modeling. One way to measure the effect due to radiation modeling is to look at the top mass distributions from HERWIG for various mixtures of gluon and no gluon events. Figure 6.4 shows the top mass distribution in b-tagged top events for three different cases of pseudo-experiments: a) standard HERWIG, b) HERWIG events with no gluon jets, and c) HERWIG events with gluon jets. Notice that changing the amount of gluon radiation present in HERWIG only shifts the peak of the top mass slightly. A more noticeable effect is the broadening of the mass distribution with the increase of gluon radiation.

The statistical uncertainty on the top mass measurement is a measurement of the width of the top mass distribution. It is possible that the statistical uncertainty reported by the mass fitter is under or overestimated, depending on the modeling of hard gluon radiation in HERWIG event generation. In Section 5.6 it was demonstrated that for the standard HERWIG Monte Carlo, the statistical uncertainty returned by the mass fitter is accurate. The accuracy of the statistical

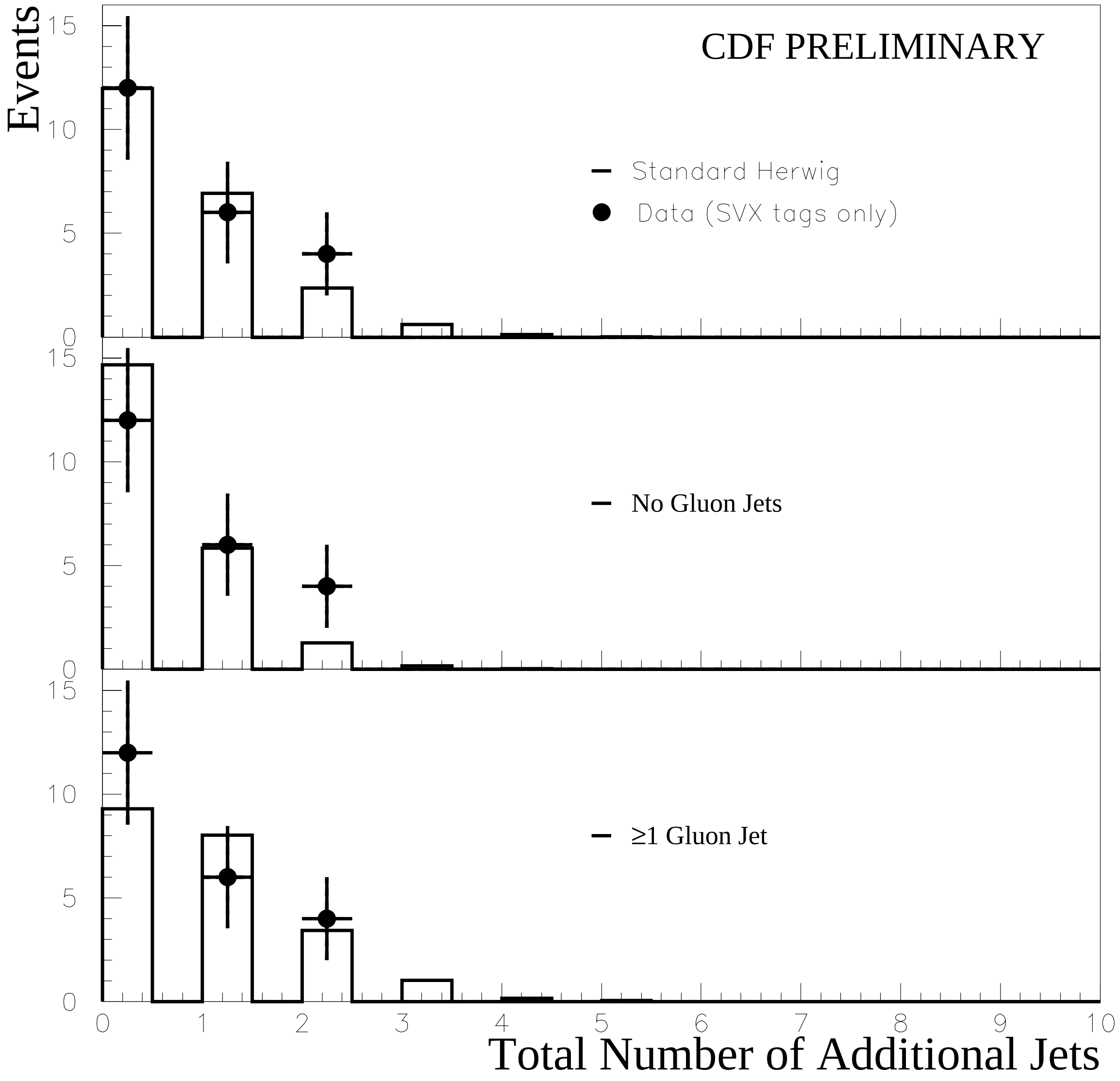

Figure 6.2: The number of jets, excluding the four highest E_T jets, per event for data (points) compared to the three different HERWIG samples (solid lines): default HERWIG, HERWIG events which do not contain a gluon jet in the first four jets, and HERWIG events which have at least one gluon jet among the first four jets. The data sample includes only mass events which have an SVX tag in at least one of the four highest E_T jets. An entry in the zero bin indicates that the event had exactly four jets.

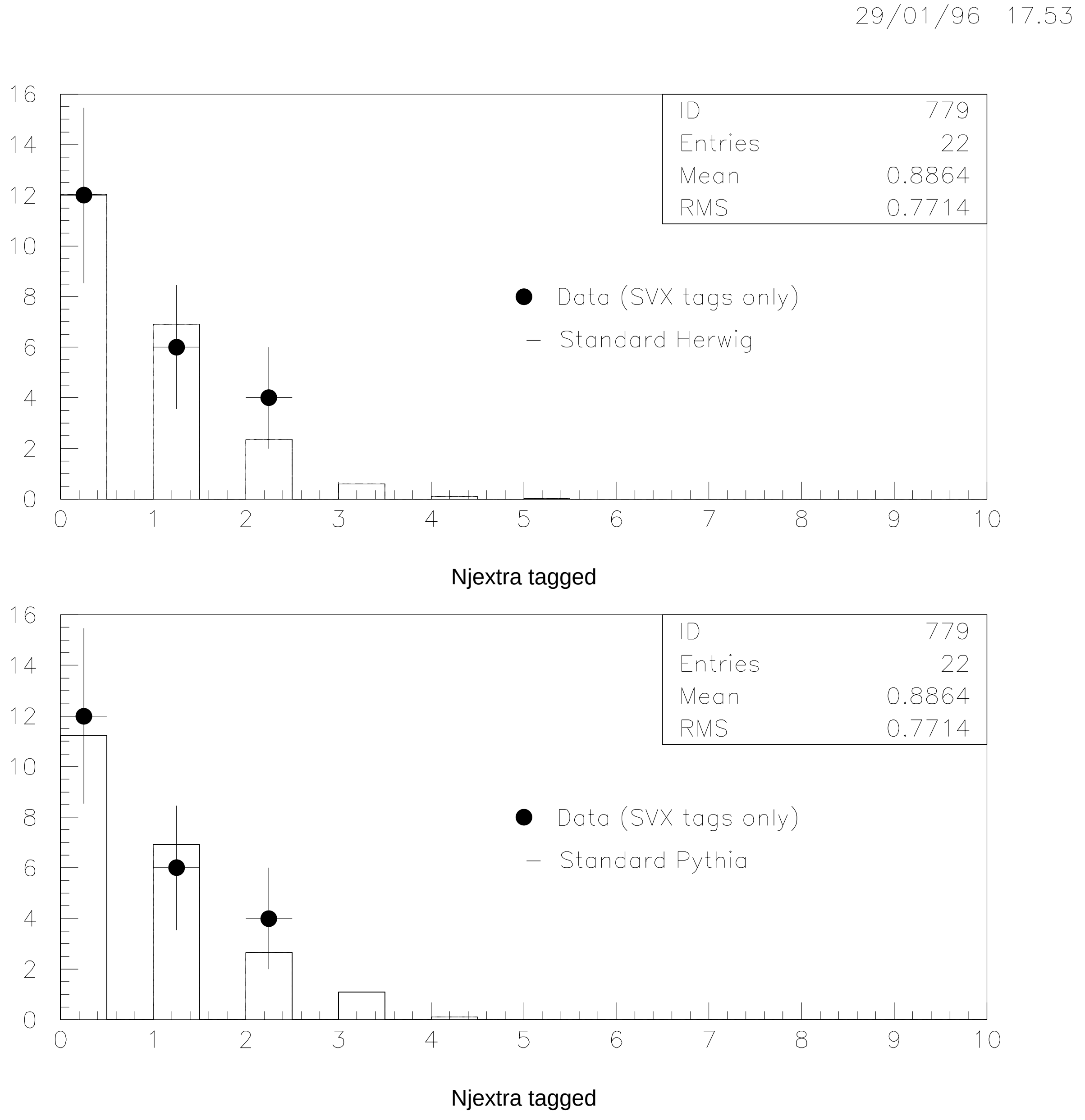

Figure 6.3: The number of jets, excluding the four highest E_T jets, per event for data (points) compared to standard HERWIG (solid line) and standard PYTHIA (solid line). The data sample includes only mass events which have an SVX tag in at least one of the four highest E_T jets. An entry in the zero bin indicates that the event had exactly four jets.

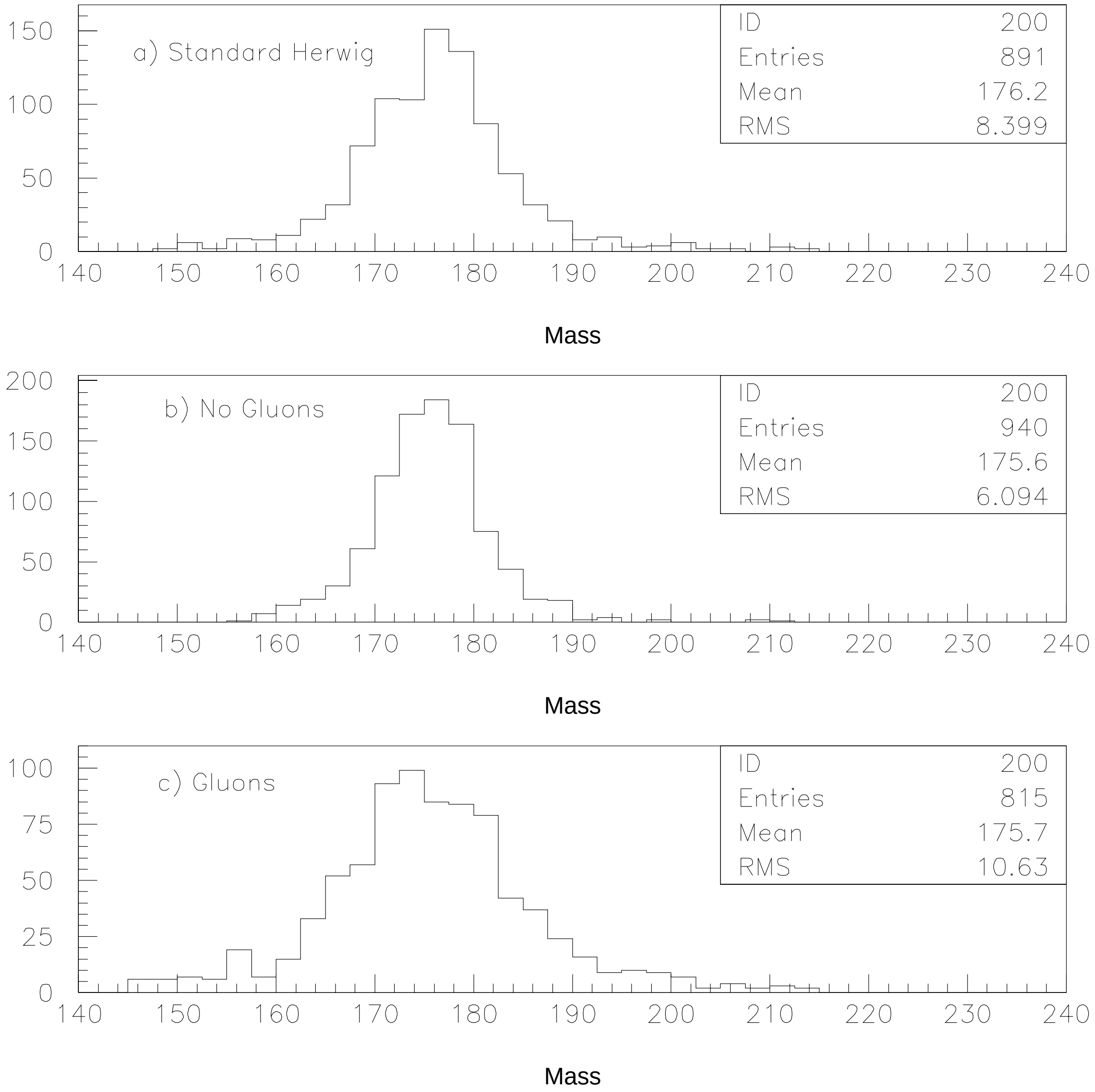

Figure 6.4: The fitted top mass distributions for pseudo-experiments where the events for the pseudo-experiment were chosen from a sample of either a) standard HERWIG, b) HERWIG events with no gluon jets among the first four jets, or c) HERWIG events with at least one gluon jet among the first four jets, and compared to standard HERWIG templates.

uncertainty was also checked for HERWIG event samples with varying percentages of gluon radiation compared to the standard HERWIG templates. Figure 6.5 plots the width of the "pull distribution" as a function of the percentage of gluon events in the HERWIG sample. The pull distribution is defined to be the top mass returned from the fit minus the input top mass (in this case, 175 GeV/c^2) divided by the statistical uncertainty returned from the fitter. If the fitter is returning the correct statistical uncertainty, the width of the pull distribution would be equal to one. The plot shows that for pseudo-experiments with less (more) gluon radiation than standard HERWIG, the statistical uncertainty returned is over-estimated (under-estimated). The statistical uncertainty is only correct when the amount of gluon radiation in the pseudo-experiments is the same as in the parameterized templates. However the slope in Figure 6.5 is linear, indicating that it is just as likely to overestimate as to underestimate the statistical uncertainty, so no systematic is quoted for this effect. In fact the data suggests that there is too much gluon radiation in HERWIG since the mass distribution is narrower than the Monte Carlo distributions. Therefore, it is more likely that the statistical uncertainty is being over-estimated.

6.3.2 Initial State Radiation

In the previous study, the effect which is being measured is the change due to varying the rate of wrong combinations (parton-jet misassociation) and not the change due to variations in the overall ratio of initial to final state radiation. To study the effects of changing the amount of initial and final state radiation in the Monte Carlo model, PYTHIA V5.7 was used. PYTHIA was used rather than HERWIG because initial and final state radiation in HERWIG V5.6 cannot be turned off. To measure the effects of initial state radiation, the mass value obtained

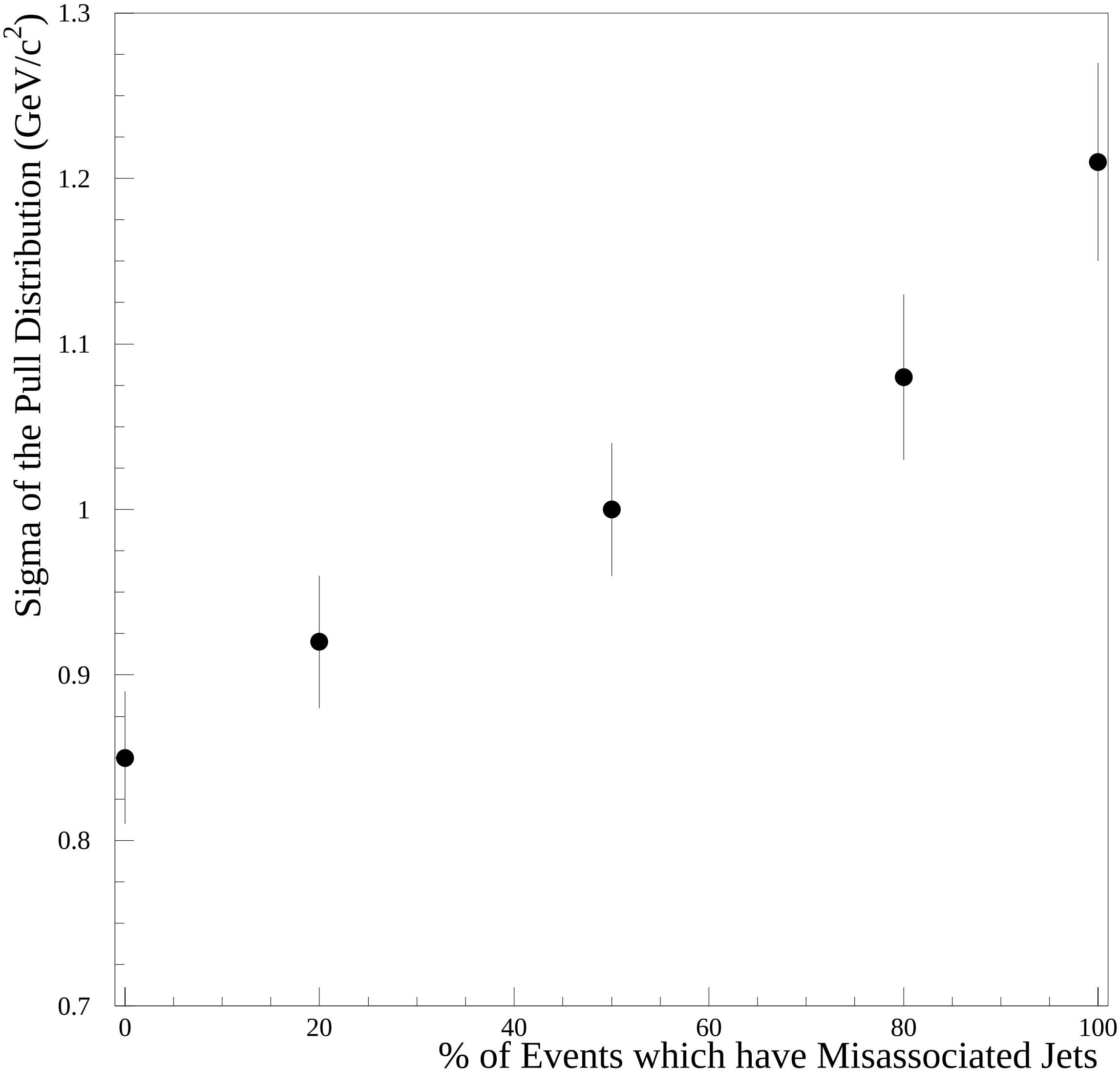

Figure 6.5: The width of the pull distribution as a function of the percentage of gluon events in the HERWIG Monte Carlo.

using standard PYTHIA V5.7 with $M_{\mathrm{top}} = 175$ GeV/c^2 is compared to the mass value for PYTHIA without initial state radiation (NOISR). A difference of 2.4 GeV/c^2 is found. This mass shift corresponds to turning off initial state radiation but it does not take into account increasing the amount of initial state radiation. The amount of initial or final state radiation cannot be increased in PYTHIA. Therefore, it was assumed that the mass shift is symmetric with respect to the amount of initial state radiation, and the mass shift was doubled between default PYTHIA and PYTHIA without initial state radiation to obtain the maximum possible range of variation of M_{top} due to our lack of knowledge about initial state radiation. This maximum range is 4.8 GeV/c^2. The conservative assumption is made that no amount of initial state radiation is more likely than any other, so the quoted systematic uncertainty is equal to the root mean squared width of a flat distribution over the entire range of variation of M_{top}, i.e. we divide 4.8 GeV/c^2 by $\sqrt{12}$. The systematic uncertainty due to initial state radiation is 1.4 GeV/c^2.

6.3.3 Final State Radiation

Final state radiation impacts the top mass in two different ways. The amount of final state radiation present in an event 1) affects the energy distribution within jets and 2) adds additional jets to events. The systematic for the first component of final state radiation is already accounted for in the jet energy scale systematic. The component which adds additional jets to an event has not been accounted for.

The effects of final state radiation on jet multiplicity must be separated from the effects of the jet energy scale. The PYTHIA $t\bar{t}$ Monte Carlo sample which was produced with no *initial* state radiation is used because all the jets in this sample come from the decay of the $t\bar{t}$ system or from final state radiation. In addition, the jet shapes are not distorted by the absence of initial state radiation, as they would be by the absence of final state radiation, so that the jet energy scale is unchanged. To evaluate the final state radiation systematic, the sample is split into two pieces – one with *exactly* four jets and one with *at least* five jets. In both samples the median top mass is determined from Monte Carlo pseudo-experiments run as described in Section 6.1. A mass shift of 3.8 GeV/c^2 is obtained between the two samples. The systematic uncertainty due to final state radiation is the mass difference divided by $\sqrt{12}$, or 1.1 GeV/c^2.

6.4 Background Spectrum

The background spectrum systematic takes into account effects due to different background shapes on the top mass. The background template used in fitting the top mass was generated from VECBOS with the Q^2 scale set equal to P_T^2. Q^2 is a measure of the momentum transferred in a collision between partons. Section 5.2 pointed out that VECBOS was a good model for the background shape. To vary the background spectrum, the Q^2 scale was changed from P_T^2 to M_W^2. Figure 6.6 shows the background spectrum from VECBOS for those two Q^2 scales. The systematic uncertainty due to varying the background spectrum is 1.3 GeV/c^2.

6.5 B-tagging Bias

The b-tagging bias systematic measures the uncertainty in the top mass due to the uncertainty in the efficiency versus $\mathrm{E_T}$ curve for SVX and SLT tagging and the rate of tagging non-B jets in real top events.

The SVX tagging efficiency is determined from Monte Carlo, then corrected by a scale factor. The scale factor was determined from data using CTC tracking studies. This scale factor is a function of jet E_T, as shown in Figure 6.7. The

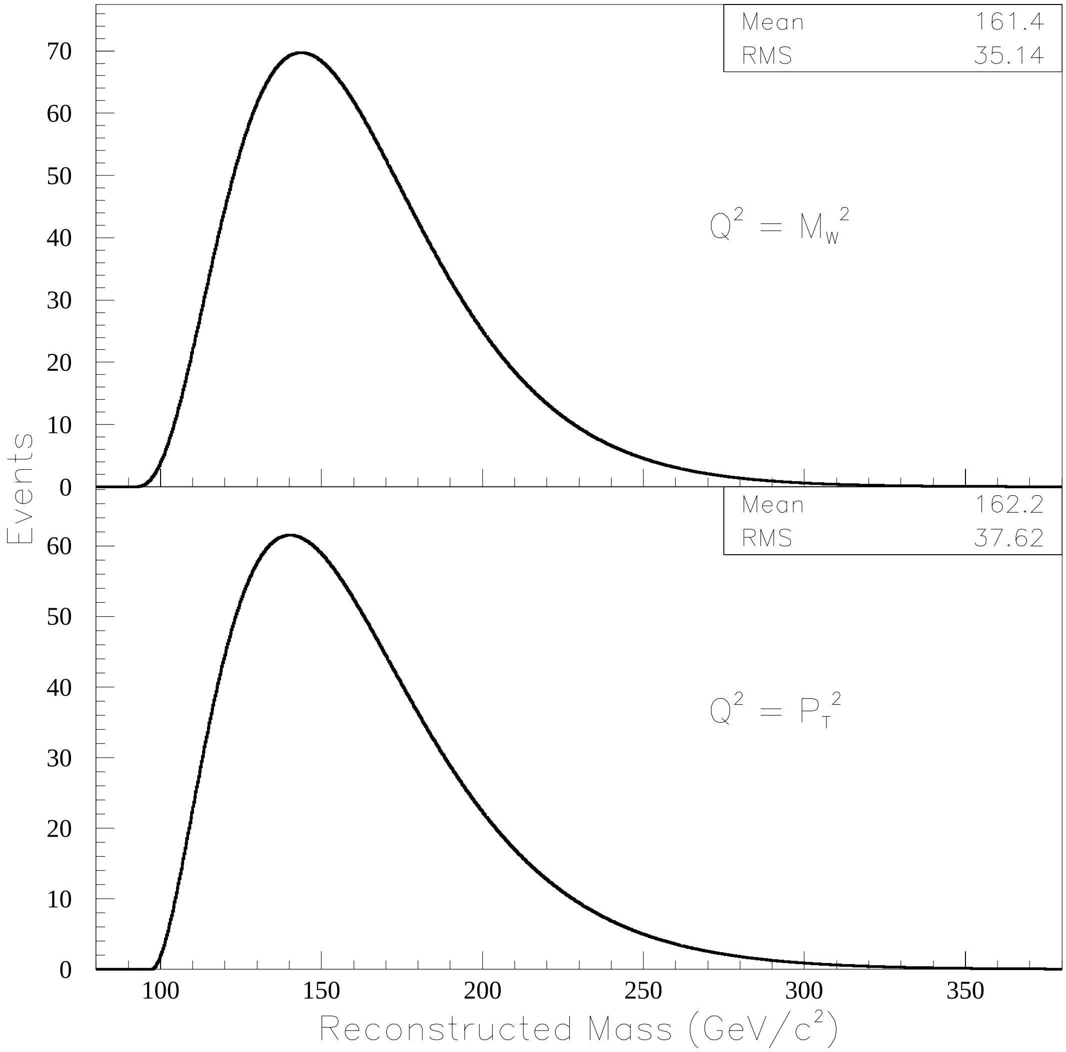

Figure 6.6: The background spectrum from VECBOS for b-tagged events with the Q^2 scale set to M_W^2 (top) or P_T^2 (bottom). The bottom plot ($Q^2 = P_T^2$) is the default background spectrum which is used for measuring the top mass.

Sample	SVX Mass Shift	SLT Mass Shift
SVX Single	-0.5	-
SVX Double	+0.2	-
SLT	-	±2.2
Not Tagged	-	-
Optimized	0.1	0.4

Table 6.5: The shifts (GeV/c^2) in the top mass due to SVX and SLT b-tagging biases are given for the 4 individual subsamples and the optimized analysis. Each number has an uncertainty of $\sim$ 0.4 GeV/c^2.

uncertainties shown in Figure 6.7 are statistical and systematic. The systematic uncertainties are determined from reasonable variations in the tracking dependance on the track quality variable, Q. Q is a measure of the hit density in the immediate area surrounding the track. The first variation assumed no Q dependence and the second variation assumed a one standard deviation stronger Q dependence than the standard for the CTC tracking efficiency. For all top analyses, the scale factor is assumed to be flat with E_T. The systematic uncertainty due to SVX b tagging was estimated by using the maximum deviation from flat allowed by the data shown in Figure 6.7. This deviation was used to sculpt the standard Monte Carlo for SVX tagging. The resultant Monte Carlo pseudo experiments were processed with the standard mass fitting routine. The deviation in the top mass from the nominal is given in Table 6.5.

The SLT efficiency is determined from data. The SLT muon selection was studied in detail with the very large $\psi \rightarrow \mu\mu$ sample. Systematic effects (like how isolated the muon is) have been studied and are flat with tagged jet E_T. SLT electron tags are studied with the high statistics $\gamma \rightarrow ee$ sample. Again, tagging rate vs. track isolation variables have been studied and residual uncertainties are

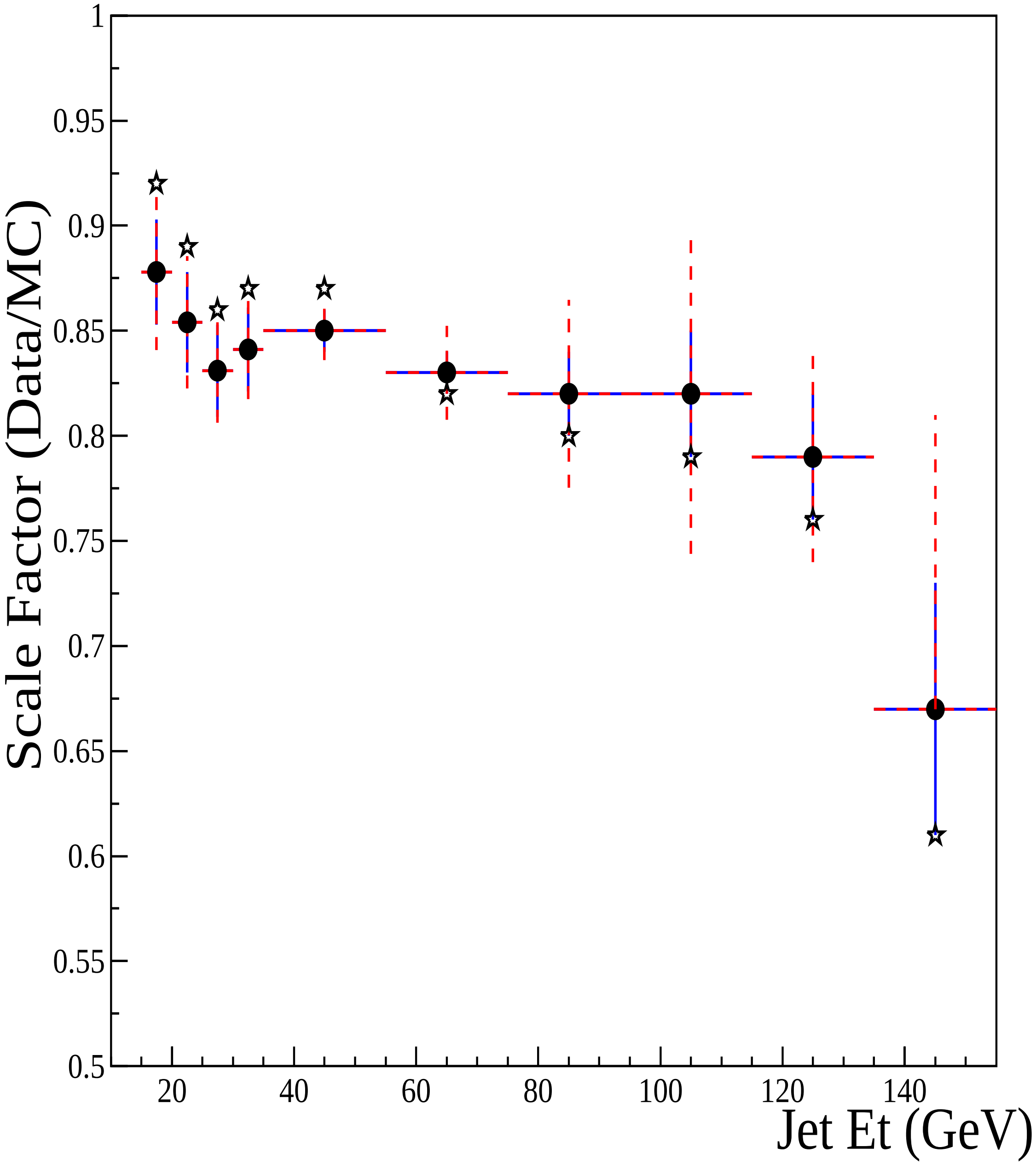

Figure 6.7: The SVX b-tagging scale factor (data-over-Monte Carlo) vs. jet E_T. The systematic uncertainty comes from assuming no Q dependence and a one standard deviation stronger Q dependence in the CTC tracking efficiency. The largest deviation from a flat distribution (stars) was used to sculpt the standard HERWIG Monte Carlo.

negligible.

One uncertainty in the SLT tagging which is relevant is the exact ratio of real-to-fake SLT tags in top events. This ratio is uncertain around the 10-20% level. In order to estimate the effect of this on the top mass, pseudo experiments were generated which had 100% fake SLT tags in top events. Pseudo experiments with 100% real SLT tags in top events were also generated. The top mass distribution is broader for fake SLT tags. Half the difference between these two extremes is clearly a conservative estimate of this systematic error. It is given in Table 6.5.

The mass shift due to SVX tagging bias is added in quadrature with the SLT tagging bias to obtain the total b-tagging bias systematic uncertainty of 0.4 GeV/c^2.

6.6 Different Parton Distribution Functions

All of the Monte Carlo samples used to measure the top mass were generated with the MRSD0$'$ parton distribution function. A parton distribution function describes how the momentum fraction of the partons inside of a hadron is distributed. MRSD0$'$ was the preferred parton distribution function at the time these samples were generated. Newer parton distribution functions now exist, in particular ones which fit CDF's inclusive jet cross section. CTEQ4L was used as an alternative parton distribution function. CTEQ4L is the latest leading order PDF and provides a reasonable variation in gluon distribution compared to MRSD0$'$. The top mass shift between these two parton distribution functions gives a systematic uncertainty of 0.3 GeV/c^2.

6.7 Different Monte Carlo Generators

HERWIG was chosen as the standard Monte Carlo model for generating top samples. It is reasonable to ask what happens to the top mass if a different Monte Carlo model is chosen. Previously this systematic was taken to be the mass shift between pseudo-experiments generated from ISAJET and pseudo-experiments generated from HERWIG [2]. This procedure was repeated and a systematic uncertainty due to different Monte Carlo generators of 1.5 GeV/c^2 was obtained.

Numerous studies have been done comparing CDF top kinematic distributions from data with distributions from HERWIG, PYTHIA and ISAJET. It has been shown that ISAJET does not reproduce the kinematic distributions of top well. In particular, the N_{jet} distribution for ISAJET does not agree well with the data. In addition the bulk of the difference between ISAJET and HERWIG is taken into account in the initial and final state radiation systematic. Including it here would be double counting the same effect, and overestimating the true systematic uncertainty. Instead of using the difference between HERWIG and ISAJET it was decided to look at the difference between HERWIG and PYTHIA. The mass shift between pseudo-experiments using PYTHIA compared to HERWIG gives a systematic uncertainty of 0.1 GeV/c^2.

6.8 Results

Systematic uncertainties on the top mass due to various sources have been evaluated. All of the systematic uncertainties studied for the top mass measurement are listed in Table 6.6. Combining all of these effects in quadrature gives an overall systematic uncertainty on the top mass of 4.9 GeV/c^2.

Source	Value (GeV/c^2)
Soft gluon effects and jet energy scale	4.4
Initial state radiation	1.4
Final state radiation	1.1
Shape of background spectrum	1.3
b-tag bias	0.4
Parton distribution functions	0.3
Monte Carlo generators	0.1
Total	4.9

Table 6.6: List of systematic uncertainties on the top mass measurement.

Chapter 7

Conclusions

The mass of the top quark has been measured in the lepton+jets decay channel to be $175.9 \pm 4.8(stat.) \pm 4.9(syst.)$ GeV/c^2 [39] [40]. Adding the uncertainties in quadrature gives a top mass of 175.9 ± 6.9 GeV/c^2. This result has the smallest fractional uncertainty of any of the quark masses.

A measurement of the top mass, along with a measurement of the mass of the W boson place limits on the Higgs boson mass. Figure 7.1 shows the CDF data point along with the standard model Higgs theory curves. This uses CDF's latest W mass measurement of 80.375 ± 0.120 GeV/c^2 [41] and the top mass measurement from this thesis. The CDF data slightly favors a lighter Higgs mass. This figure shows that the mass of the Higgs boson has a greater dependence on the mass of the W than on the top.

For at least the next 7 years, Fermilab will be the only accelerator in the world that will be able to produce top quarks. A new data taking run will be starting up in 1999 and hopefully 2 fb^{-1} of data will be taken. With this new data it is hoped to measure the top mass to within a total uncertainty of 2 GeV/c^2 [41].

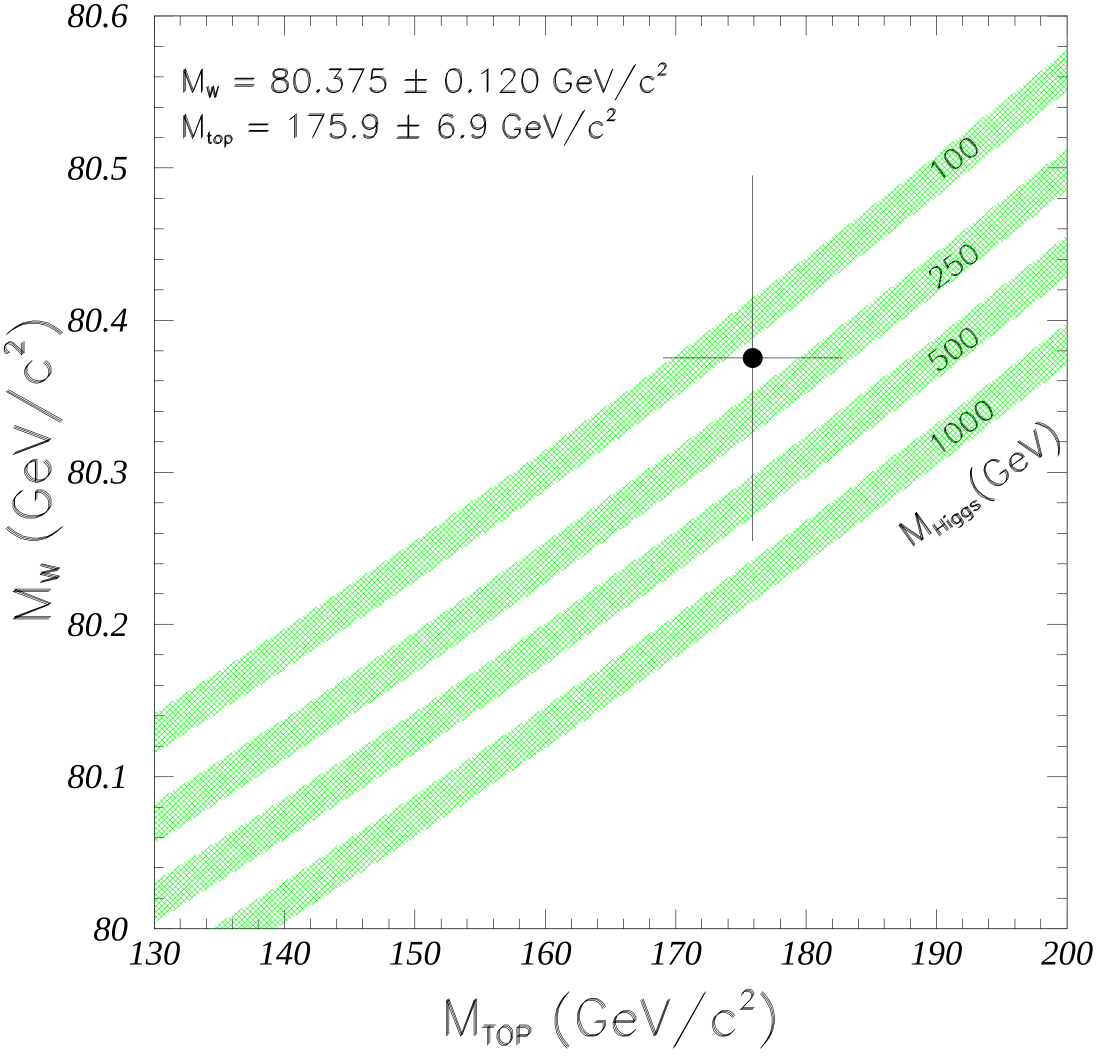

Figure 7.1: CDF's latest top and W mass results with their uncertainties plotted on top of theoretical Higgs mass values.

Bibliography

[1] *Modern Elementary Particle Physics* by Gordon Kane (Addison-Wesley Publishing Co. 1993) describes the theory of the standard model at a level appropriate for undergraduate physics majors who have had classes in basic electromagnetism, mechanics and quantum theory. The book *Introduction to Elementary Particles* by David Griffiths (John Wiley & Sons, Inc. 1987) contains a brief historical review of particle physics.

[2] F. Abe *et al.*, Phys. Rev. D **50**, 2966 (1994);

[3] F. Abe *et al.*, Phys. Rev. Lett. **73**, 225 (1994).

[4] F. Abe *et al.*, Phys. Rev. Lett. **74**, 2626 (1995).

[5] S. Abachi *et al.*, Phys. Rev. Lett. **74**, 2632 (1995).

[6] I. Bigi *et al.*, Physics Letters B, **157**, (1986).

[7] L. Orr, Phys. Rev. D **44**, 44, (1991).

[8] P. Azzi, Thesis, University of Padova, (1996).

[9] W. Bokhari, Thesis, Massachusetts Institute of Technology, (1997).

[10] F. Abe *et al.*, FERMILAB-PUB-97/075-E. To be published in Phys. Rev. Lett.

[11] F. Abe *et al.*, FERMILAB-PUB-97/304-E. To be published in Phys. Rev. Lett.

[12] S.D.Holmes FERMILAB-Conf-87/160(unpublished).

[13] **http://www-fermi3.fnal.gov**.

[14] F.Abe *et al.*, Nucl. Inst. Meth. **A 271**, 378 (1988).

[15] D. Amidei *et al.*, Nucl. Inst. Meth. **A 350**, 73 (1994); D. Amidei *et al.*, Nucl. Inst. Meth. **A 360**, 137 (1995).

[16] M. Kruse, Thesis, Purdue University, (1995).

[17] A.D. Martin, R.G. Roberts, and W.J. Stirling, Phys. Lett. B **306**, 145 (1993).

[18] F. Abe *et al.*, Phys. Rev. Lett. **74**, 850 (1995).

[19] Particle Data Group, R.M. Barnett *et al.*, Phys. Rev. D **54**, 1 (1996).

[20] P. Avery, K. Read, G. Trahern, Cornell Internal Note CSN-212, March 25, 1985 (unpublished).

[21] F. Abe *et al.*, Phys. Rev. Lett., **75**, 608 (1995).

[22] G. Marchesini and B.R. Webber, Nucl. Phys. B **310**, 461 (1988); G. Marchesini *et al.*, Comput. Phys. Commun. **67**, 465 (1992). This analysis uses HERWIG version 5.6.

[23] T. Sjöstrand, Comput. Phys. Commun. **82**, 74 (1994). This analysis uses PYTHIA version 5.7.

[24] F. Paige and S. Protopopescu, BNL Report No. 38034, 1986 (unpublished). This analysis uses ISAJET version 7.06.

[25] T. Sjöstrand, CERN-TH-6488-92, May (1992).

[26] F.A. Berends, W.T. Giele, H.Kuijf, and B. Tausk, Nucl. Phys. B **357**, 32 (1991).

[27] F. Abe *et al.*, Phys. Rev. Lett., **70**, 4042 (1993).

[28] G. Watts, Ph.D. Thesis, University of Rochester, (1994).

[29] D. Glenzinski, Ph.D. Thesis, The Johns Hopkins University, (1995).

[30] D. Kestenbaum, Ph.D. Thesis, Harvard University, (1996).

[31] F. Abe *et al.*, Phys. Rev. Lett. **75**, 11 (1995).

[32] F. Abe *et al.*, Phys. Rev. Lett. **74**, 341 (1995).

[33] M. Jeżabek and J.H. Kühn, Phys. Rev. D **48**, R1910 (1993); erratum: *ibid.* **49**, 4970 (1994).

[34] F. James and M. Roos, Comput. Phys. Commun. **10**, 343-367 (1975).

[35] F. Abe *et al.*, FERMILAB-PUB-97/286-E. To be published in Phys. Rev. Lett.

[36] N. Eddy, Ph.D. Thesis, University of Michigan, (1997).

[37] S. Bettelli, Ph.D. Thesis, University of Pisa, (1997).

[38] I.C. Brock, MNFIT: A Fitting and Plotting Package Using MINUIT Version 4.02 June 2, 1994.

[39] F. Abe *et al.*, FERMILAB-PUB-97/284-E. To be published in Phys. Rev. Lett.

[40] S. Aota, A. Beretvas, S. Bettelli, M. Binkley, S. Blusk, L. Demortier, N. Eddy, L. Galtieri, S. Kim, M. Lanzoni, J. Lys, R. Roser, P. Tipton, K. Tollefson, S. Vejcik, G. Velev, CDF internal document 4199, Measurement of the Top Quark Mass in the Lepton+Jets Channel. A Phys. Rev. D article is currently being written.

[41] F. Abe *et al.*, FERMILAB-PUB-96/390-E.